MANCHESTER 1824
The University of Manchester

Double Exchange Spin Dynamics within Valence Delocalised Molecules

A thesis submitted to the University of Manchester for the degree of
Doctor of Philosophy
in the Faculty of Science and Engineering

2024

Rasmus Tang Christiansen
Department of Chemistry

[Page intentionally left blank]

Contents

Word count: 30243

List of Figures

List of Tables

Abstract

Magnetic molecules can host diverse fundamental quantum phenomena such as magnetic bistability, entanglement, tunnelling, and coherence of quantum superpositions. Consequently, molecules have the potential to be key ingredients for the second quantum revolution provided that we, on a fundamental level, understand them well enough to harness their quantum properties. Therefore, the scientific community has a responsibility to pursue fundamental knowledge about the quantum mechanics at play within molecules.

This thesis investigates a particular quantum phenomenon at play within molecules: delocalisation of valence electrons across several magnetic ions. Such delocalisation can give rise to so-called double exchange interactions, which contribute uniquely to molecular spin dynamics. Still, fundamental understanding of the phenomenon remains scarce, in large due to a lack of adequate experimental methods for probing this intrinsically complex phenomenon. To tackle this issue, this work sets out to establish inelastic neutron scattering (INS) as a key spectroscopic probe of double exchange spin dynamics.

To realise this goal, a combination of INS, high-frequency paramagnetic resonance, and far-infrared magnetospectroscopy was used to investigate the spin dynamics of increasingly complex valence delocalised molecules. These studies show that INS is highly sensitive to the unique spin dynamics that emerge in this class of molecules. To aid the interpretation of the INS data, a spin Hamiltonian modelling tool was developed that, for the first time, incorporates double exchange alongside traditional magnetic interactions. Simulations of momentum-resolved INS spectra furthermore showed that experiments performed on single crystals have the potential to quantify the degree of electron delocalisation based on experimental data. Thus, INS offers the possibility to obtain a complete description of double exchange spin dynamics.

Declaration of originality

I hereby confirm that no portion of the work referred to in the thesis has been submitted in support of an application for another degree or qualification of this or any other university or other institute of learning.

Copyright statement

i The author of this thesis (including any appendices and/or schedules to this thesis) owns certain copyright or related rights in it (the "Copyright") and s/he has given The University of Manchester certain rights to use such Copyright, including for administrative purposes.

ii Copies of this thesis, either in full or in extracts and whether in hard or electronic copy, may be made *only* in accordance with the Copyright, Designs and Patents Act 1988 (as amended) and regulations issued under it or, where appropriate, in accordance with licensing agreements which the University has from time to time. This page must form part of any such copies made.

iii The ownership of certain Copyright, patents, designs, trademarks and other intellectual property (the "Intellectual Property") and any reproductions of copyright works in the thesis, for example graphs and tables ("Reproductions"), which may be described in this thesis, may not be owned by the author and may be owned by third parties. Such Intellectual Property and Reproductions cannot and must not be made available for use without the prior written permission of the owner(s) of the relevant Intellectual Property and/or Reproductions.

iv Further information on the conditions under which disclosure, publication and commercialisation of this thesis, the Copyright and any Intellectual Property and/or Reproductions described in it may take place is available in the University IP Policy (see `http://documents.manchester.ac.uk/DocuInfo.aspx?DocID=24420`), in any relevant Thesis restriction declarations deposited in the University Library, The University Library's regulations (see `http://www.library.manchester.ac.uk/about/regulations/`) and in The University's policy on Presentation of Theses.

Acknowledgements

First and foremost, I owe my supervisors Dr Michael L. Baker and Dr Jacques Ollivier tremendous debts of gratitude. Their insights and guidance have been vital for my success. I want to thank them for believing that I was the right person for the project.

Mike, I want to thank you for the crucial role you have played in shaping the scientist I have become over the past three years. For your understanding when life got difficult during the COVID-19 pandemic in a country far from home. For playing along when my odd brain came up with crazy ideas, and for reeling me be back to reality when the ideas became a bit too crazy. For your willingness to send me around the world to do cool experiments and attend inspiring conferences. And ultimately for showing me what steps to take next in my scientific career. You taught me how to be a scientist. Thank you for that!

Jacques, merci beaucoup pour les heures passées dans la cabine d'IN5. Merci pour avoir pris le temp de m'apprendre les details sur la diffusion des neutrons et pour avoir repondu à mes appels paniqués quand j'ai eu des questions stupide. Tu as toujour eu le temp pour me voir avec un preavis très court, quand même pendant la cycle. J'espere qu'on se rencontre encore a l'ILL dans la future.

The PhD community at Institute Laue-Langevin has played a big part in my life throughout the past three years. It was not easy to arrive in a foreign country with COVID-19 curfew from 6 pm to 6 am, but I would do it all again for the friends I made. Thank you for the laughs, the hikes, the skiing trips, the nights out and everything else we have done together. You know who you are. I hope we do not become strangers.

I also want to thank the (former) members of the Baker group: Myron, Tim, Nathan, and Alan. Thank you for being so welcoming every time I came to visit, and for being so pleasant company. Even though Manchester was far from my daily life, I always felt like I belonged.

Science is a collaborative effort, and I want to thank our talented synthetic collaborators for their amazing samples: Wenwei Zheng, Dr Shu-Qi Wu, and Prof. Osamu Sato from Kyushu University, and Dr Grigore Timco and Prof. Richard Winpenny from the University of Manchester. Without them, a physicist like me would never have managed to do a chemistry PhD. Likewise, thank you to all the scientists at user facilities that have helped me get the data for this thesis. In particular, thank you to Dr Anne-Laure Barra and Dr Florian Le Mardelé for teaching me the ways of EPR and FIRMS.

Lastly, I want to thank my family. Mor, far og Caroline, tak for jer! Selvom min verden har ligget langt fra jeres, både konkret og figurativt, har jeg aldrig tvivlet på jeres støtte. Mit videnskabelige eventyr gør, at vi ikke ses så meget, som nogen af os kunne ønske, men I har stadig altid sagt: Go for it! Tak for det!

Organisation of Thesis

We present this thesis in the Journal Format because we intend to present the contents of Chapters 3-5 for peer-reviewed publication in the near future. For each of these chapters, we give a short prelude which outlines the underlying research goals and explain the individual contributions of all authors.

To compliment the draft manuscripts, Chapters 1 and 2 introduce the most important theoretical background and experimental methods, respectively, while Chapter 6 summarises the work undertaken, highlights the main conclusions drawn therefrom and provides a perspective of its contribution to the broader research landscape.

Chapter 1

Introduction

This chapter introduces the main topics of this thesis; molecular magnetism and valence delocalisation. First, a condensed overview of the current state of molecular magnetism research is given, followed by a presentation of the fundamentals of single ion magnetism. From there, the Heisenberg exchange interaction and the giant spin approximation are introduced, followed by a section on valence delocalisation and double exchange. In that context, vibronic coupling in mixed-valence molecules and how it affects delocalisation and double exchange are also discussed. The reader is assumed to be familiar with quantum mechanics at the level of a physics undergrad, with basic knowledge of wave functions, Dirac notation and the most common properties of Hamiltonian matrices.

1.1 Current State of Molecular Magnetism Research

Molecular magnetism is a broad scientific field encompassing the synthesis, characterisation and physical properties of materials built using molecules containing paramagnetic centres as the fundamental building blocks. While magnetochemistry has long been a mature scientific field, molecular magnetism in a modern context rose to prominence in the early 1990's spearheaded by the discovery of magnetic bistability in Mn_{12}, a large molecule consisting of 12 magnetic centres bridged by acetate ligands [1], [2]. Since then, the near endless possibilities offered by coordination chemistry has taken the field in a couple of different directions. Significant effort is currently put into the realisation of new molecule-based permanent magnets highlighted by the recent discoveries of metal-organic frameworks with a magnetic performance comparable to commercial magnets and of ultra-hard magnetism in a mixed-valence lanthanide dimer [3], [4]. High-temperature hysteresis within single ions, for use in e.g. ultra-compact information storage, is also a highly desired synthetic goal. The current leaders of the field are dysprosocenium derivatives, some of which have hystereses above liquid nitrogen temperatures, and scientists actively explore avenues for enhancing their utility and performance via deposition on surfaces or encapsulation within fullerenes [5]–[8]. Single molecules are also being tailored to act as quantum bits, and a molecule was recently used for a proof-of-concept quantum simulation for the first time [9], [10]. Molecules also hold promise for use in spintronics, and the recent discovery of chirality-induced spin selectively could make read-out of molecular spin states more efficient [11]–[13].

The work of this thesis focuses on molecules containing valence electrons delocalised between more than one centre, a class of molecules with potential impact to a diverse range of scientific fields including materials science, quantum information and biology. From the materials perspective, they are proposed to exhibit magnetic properties that are sensitive to applied electrical fields, a highly desirable quality for spintronics or sensing applications [14], [15]. Also, spins within these molecules are usually strongly coupled, which holds promise for their use in new molecule-based permanent magnets [4]. Biologists are interested in these molecules since active sites of many enzymes contain valence delocalised clusters [16]. The most well-know example is probably nitrogenase, which catalyses the transformation of N_2 into ammonia at ambient conditions [17], [18]. Elucidation and exploitation of this reaction could have enormous socio-economic consequences. It is estimated that up to 40 % of the world's population depend on crops fertilised with ammonia, and the standard industry method for nitrogen fixation, the Harber-Borsch process, consumes towards 1 % of the world's energy annually due to extreme temperature and pressure requirements [19].

From a fundamentals perspective, spin-polarisation of the delocalised electron(s) gives rise to unique spin dynamics that are still poorly understood. This lack of fundamental knowledge hinders the elucidation of more complex phenomena, such as magneto-vibrational and magneto-electric couplings, which are essential to understand before the full potential of mixed valence molecules can be realised.

The main issue holding back investigations of valence delocalised spin dynamics is a severe lack of accurate methods for investigating them. Nowadays, scientists within the field mainly use two experimental methods: magnetometry, which only provides indirect information about the magnetic interactions, and visible light spectroscopy, which rarely contains enough information to accurately parameterise the complicated magnetic interactions within, especially when magnetic and vibrational degrees of freedom are coupled [20], [21]. From a theoretical perspective, *ab initio* quantum chemistry methods are still best suited for mononuclear species despite significant recent developments and therefore difficult to apply to mixed-valence systems [22], [23]. Even when valence delocalisation can be considered, it is usually limited to two-centre cases due to the problem's intrinsic complexity [24]. In contrast, theoretical descriptions relying on parameterised approaches are relatively well developed, however their utility suffer from the lack of experimental probes capable of providing enough information for accurate modelling without overparameterisation [25], [26].

The goal of this thesis is to overcome these challenges by using inelastic neutron scattering (INS) and other advanced spectroscopy methods to probe the spin dynamics within valence delocalised molecules. INS experiments provide direct access to the energy gaps between molecular spin states and the ability to differentiate between particular types of transitions via their neutron momentum transfer dependencies. To take full advantage of the plethora of information these experiments provide, part of the work undertaken during this thesis has been to incorporate valence delocalisation into spectroscopic simulation tools like

Easyspin and *mint* [27], [28]. This way, we can quantify the agreement between Hamiltonian models and INS, electron paramagnetic resonance (EPR) and magnetometry experiments.

By combining INS with other experimental techniques, we have developed a comprehensive approach for probing the spin dynamics of valence delocalised molecules and other strongly interacting magnetic systems, which allows us to extract details no single experimental technique can provide. We apply our methodology to systems with increasing complexity starting with radical-bridged iron dimers (Chapter 3). In that work we were able to directly probe elusive strong metal-radical interactions, and it furthermore acted as test bed before applying our approach to more complicated systems. Next, we investigated a mixed-valence iron carboxylate trimer in which a valence electron is shared amongst two of the three iron centres (Chapter 4) [29], [30]. Our INS data provides the first direct spectroscopic evidence of valence delocalised spin dynamics and allows us to constrain all magnetic interactions and the single-ion anisotropy of the system. Based on the obtained model, we predict that delocalisation excitations have unique momentum transfer dependencies, which can be unravelled by single-crystal INS experiments. Furthermore, we show that preferential occupation within partially delocalised molecules can be resolved. With the experience gained from the first two studies, we turned our attention towards a more complex system; nano-sized iron cluster in which two valence electrons hop between six magnetic centres (Chapter 5) [31]. With our approach, we were finally able to pin down the exchange couplings and electron distribution within this molecule, which showcases that our approach is applicable to complex molecules.

1.2 Magnetism of Single Ions

The fundamental entity in molecular magnetism is the unpaired electrons within a molecule, which reside on metal ions or organic radicals. The electrons have intrinsic spin angular momentum, $\hbar s$, as well as orbital angular momentum, $\hbar l$; the latter depends on the atomic orbital occupied by the electron [32]. The spin is governed by the operators [33]

$$\mathbf{s} = s_x\hat{i} + s_y\hat{j} + s_z\hat{k}$$

$$s_x = \frac{1}{2}\begin{pmatrix} 0 & 1 \\ 1 & 0 \end{pmatrix}, \qquad s_y = \frac{1}{2}\begin{pmatrix} 0 & i \\ -i & 0 \end{pmatrix}, \qquad s_z = \frac{1}{2}\begin{pmatrix} 1 & 0 \\ 0 & -1 \end{pmatrix}, \tag{1.1}$$

here expressed in the eigenbasis of s_z. The projections follow the commutation relations $[s_i, s_j] = i\epsilon_{ijk}s_k$ and are not simultaneously observable. In contrast, $[\mathbf{s}^2, s_z] = 0$ which means that the total spin magnitude and its $z-$projection can be known at the same time [32]. Thus, an electron spin is uniquely defined by its projection since $s = |\mathbf{s}| = 1/2$ always.

In first-row transition metals (TMs), the most studied magnetic ions and the topic of this thesis, the valence electrons occupy the $3d$ shell. It contains five orbitals and thus is five-fold degenerate for a free ion. In a molecule, the crystal electric field (CEF) generated by the ligands breaks the degeneracy and the molecular symmetry determines the energetic ordering

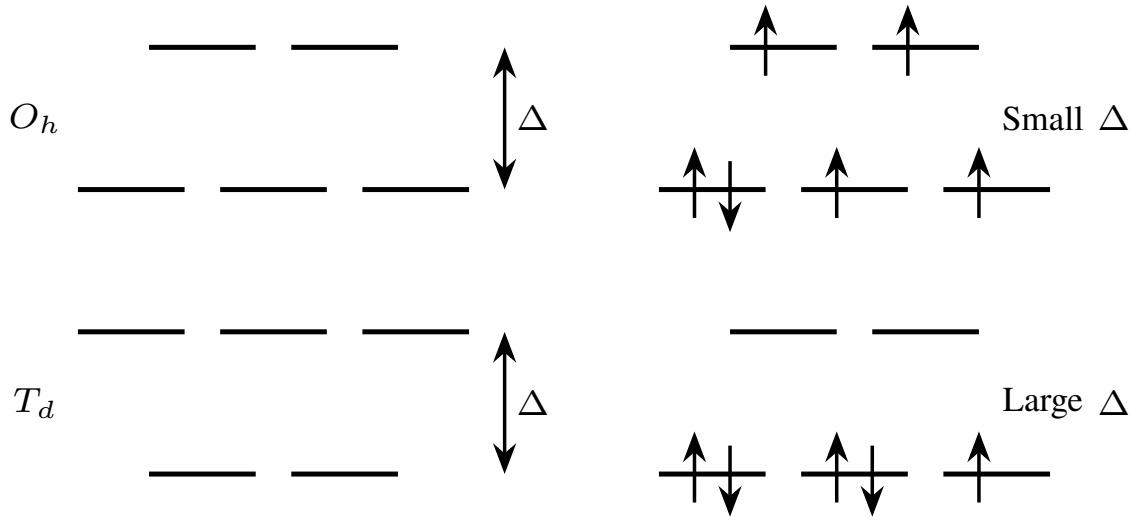

Fig. 1.1. Left: Schematic of $3d$ orbital splitting caused by the crystal electric field (CEF) in octahedral (O_h) and tetrahedral (T_d) point symmetry. Δ is the magnitude of the CEF splitting. **Right:** Electron occupation in a $3d^5$ ion for weak (small Δ) and strong (large Δ) CEF in octahedral symmetry.

of the orbitals as shown in Fig. 1.1 (left). In the octahedral case (O_h symmetry), the d_{xy}, d_{xz}, and d_{yz} orbitals, collectively denoted t_{2g}, lie lowest since they point in-between the axis of an octahedron. The d_{x^2} and $d_{x^2-y^2}$ orbitals, collectively denoted e_g, point along the octahedron axes and consequently lie lowest in the tetrahedral case (T_d symmetry) [33].

When the number of valence electrons is less than or equal to the number of lowest-lying $3d$ orbitals, the electron spins align parallel in order to minimise Coulomb repulsion as summarised by Hund's rules. When more valence electrons are present the orbital occupation depends on the strength of the CEF relative to Coulomb repulsion. When the CEF is weak, the gap Δ between the two orbital manifolds becomes small. Then, Coulomb repulsion still governs orbital occupation and high-spin states emerge. When the CEF is strong, Δ can become larger than the Coulomb energy, which forces the electrons into the lowest-lying manifold and creates a low-spin state; this is exemplified for a $3d^5$ ion in Fig. 1.1 (right) [33].

Assessing the magnetic properties of ions in molecules through the lens of atomic orbitals is not strictly correct. The electrons will occupy molecular orbitals which are superpositions of metal and ligand orbital as can be calculated by e.g. complete active space self-consistent field (CASSCF) calculations. However, physical magnetic orbitals will usually have a major defining component from an atomic orbital of the magnetic ion, which often makes approaching molecular magnetism from the atomic orbital point-of-view a good approximation [34].

The orbital angular momentum of electrons in $3d$ ions is usually suppressed, or even vanishing, due to a phenomenon known as *orbital quenching*. This can be understood by examining the mathematical properties of the angular momentum operator $\mathbf{l} = -i\hat{\mathbf{r}} \times \nabla$ and the CEF. By definition, $\mathbf{l}$ is Hermitian and purely imaginary, while the CEF is given by a real function in the case of strict O_h symmetry. If the ground state, $|0\rangle$, is non-degenerate like in the high-spin $3d^5$ case in Fig. 1.1 (right), the wave function of $|0\rangle$ must be real. As a consequence, $\langle 0|\,\mathbf{l}\,|0\rangle \in i\mathbb{R}$ since $\mathbf{l}$ is purely imaginary. However, it must also be that

$\langle 0|\,\mathbf{l}\,|0\rangle \in \mathbb{R}$ since $\mathbf{l}$ is Hermitian. These two statements can only be combined to $\langle 0|\,\mathbf{l}\,|0\rangle = 0$, i.e. the vanishing of orbital angular momentum in the ground state. While this "proof" is not generally applicable, it sheds light on the mechanisms responsible for orbital quenching [33].

Orbital quenching is rarely complete in real molecules, e.g. due to low CEF symmetry or orbital degeneracy like the low-spin $3d^5$ cases in Fig. 1.1 (right). However, it is not necessary to explicitly deal with the remaining orbital angular momentum for most first-row TMs and the ionic spin, given by the sum of the spins of the electrons, $\mathbf{S} = \sum_i \mathbf{s}_i$, becomes the operator that governs angular momentum. Its magnitude is $S = n_e/2$ (n_e is the number of unpaired electrons) and there are $2S + 1$ possible projections: $-S, -S + 1, \ldots, S - 1, S$. The corresponding spin operators can be built by successive coupling of the entities from eq. (1.1) and they will obey the same commutation relations as the single-electron operators [35].

We account for the left-over angular momentum by treating spin-orbit coupling [33]

$$\mathcal{H} = \lambda \mathbf{S} \cdot \mathbf{L} \tag{1.2}$$

as a second-order (or higher) perturbation, which mixes excited states with finite total angular momentum ($\mathbf{L} = \sum_i \mathbf{l} \neq 0$) into the ground state [36]. Ultimately, it is the CEF that governs the amount of orbital angular momentum since the strength of the perturbation depends on the energy gap between the ground and excited states, which is determined by the CEF [32]. The perturbation breaks the degeneracy of the different projections of the total spin $\mathbf{S}$ and is usually called *zero-field splitting* (ZFS). According to Kramer's theorem, all states of a half-integer spin system that obeys time reversal symmetry must be $2n$-fold degenerate (n is an integer) [37]. Therefore, ions with $S = 1/2$ have no ZFS since the two projections $m_S = \pm 1/2$ must be degenerate. Another consequence of mixing orbital angular momentum into the ground state is that the effective moment of an ion can be different from the spin-only value and that the $\mathbf{g}$-tensor does not have to be single-valued.

The Hamiltonian that governs the spin-CEF interaction can contain arbitrarily high powers of spin operators depending on the order of the perturbation treatment. In practice, one takes advantage of the point symmetry of the ion and the irreducible tensor approach to limit the necessary operators by using the extended Steven's operators [36]. In this formalism, the CEF Hamiltonian is given by [38]

$$\mathcal{H} = \sum_{k,q} B_k^q \hat{O}_k^q \tag{1.3}$$

where $\hat{O}_k^q$ are the Steven's operators, which are polynomials of the spin operators and tabulated in e.g. [39]. The B_k^q constants parameterise the strength of each operator. k and q take integer values; $k \leq 2S$ for integer S and $k \leq 2S - 1$ for half-integer S, while $-k \leq q \leq k$ always. The molecular symmetry determines which B_k^q have non-zero values; in strict O_h symmetry only B_4^0, B_4^4, B_6^0, and B_6^4 are non-zero [39].

1.3 Magnetic Interactions

When a molecule contains more than one magnetic centre (ions with unpaired electrons or radicals) these can interact with one-another, either via direct overlap of the magnetic orbitals or overlap mediated by a bridging ligand. Consider the simplest coupled system consisting of two sites at a and b each containing an electron. By definition the square of the total spin operator $\mathbf{S} = \mathbf{s}_a + \mathbf{s}_b$ is given by [32]

$$\mathbf{S}^2 = \mathbf{s}_a^2 + \mathbf{s}_b^2 + 2\mathbf{s}_a \cdot \mathbf{s}_b \tag{1.4}$$

where $s_{a/b}$ are the single-electron operators and the squared operators are hermitian with eigenvalues $\mathbf{s}_\alpha^2 \left|½, \pm ½\right\rangle = \hbar s(s+1) \left|½, \pm ½\right\rangle = 3\hbar/4 \left|½, \pm ½\right\rangle$. The basis of the coupled system is spanned by product states generated by taking the Kronecker product of the bases of the single-electron states [35].

According to the Pauli principle, the overall wave function of the two-electron system must be antisymmetric since electrons are fermions, and it must also be an eigenfucntion of $\mathbf{S}$. This leaves the following possibilities for the spin part of the wave function [33]

$$|A\rangle = \left|\frac{1}{2}, +\frac{1}{2}\right\rangle \left|\frac{1}{2}, +\frac{1}{2}\right\rangle \tag{1.5a}$$

$$\sqrt{2}\,|B\rangle = \left|\frac{1}{2}, -\frac{1}{2}\right\rangle \left|\frac{1}{2}, +\frac{1}{2}\right\rangle + \left|\frac{1}{2}, +\frac{1}{2}\right\rangle \left|\frac{1}{2}, -\frac{1}{2}\right\rangle \tag{1.5b}$$

$$|C\rangle = \left|\frac{1}{2}, -\frac{1}{2}\right\rangle \left|\frac{1}{2}, -\frac{1}{2}\right\rangle \tag{1.5c}$$

$$\sqrt{2}\,|D\rangle = \left|\frac{1}{2}, +\frac{1}{2}\right\rangle \left|\frac{1}{2}, -\frac{1}{2}\right\rangle - \left|\frac{1}{2}, -\frac{1}{2}\right\rangle \left|\frac{1}{2}, +\frac{1}{2}\right\rangle \tag{1.5d}$$

where the kets on the RHS describe single-electron wave functions. States A-C are symmetric, thus their spatial parts must be antisymmetric, whereas the opposite is true for state D. All states are eigenstates of $\mathbf{S}^2$ with $\mathbf{S}^2 \left|\beta\right\rangle = 2\hbar \left|\beta\right\rangle$ for states $|A\rangle$-$|C\rangle$ (they correspond to $S = 1$), and $\mathbf{S}^2 \left|D\right\rangle = 0$ (it corresponds to $S = 0$). Meanwhile, the eigenvalues of $\mathbf{s}_a^2$ and $\mathbf{s}_b^2$ are $3/4$ for any of the four states. Thus, the eigenvalues of $\mathbf{s}_a \cdot \mathbf{s}_b$ must be $1/4$ for the $S = 1$ states and $-3/4$ for the $S = 0$ state to arrive at the correct eigenvalues of $\mathbf{S}^2$. Therefore, the operator $\mathbf{s}_a \cdot \mathbf{s}_b$ can parameterise the energy difference between states with different values of S as

$$\mathcal{H} = \frac{1}{4}(E_S + E_T) - (E_S - E_T)\mathbf{s}_a \cdot \mathbf{s}_b \tag{1.6}$$

where E_T is the energy of the triply degenerate (triplet) $S = 1$ state and E_S is the energy of the singly degenerate (singlet) $S = 0$ state. If we assume that the electrons, located at $\mathbf{r}_1$ and $\mathbf{r}_2$, occupy atomic orbitals ϕ_a and ϕ_b on sites a and b, the total singlet and triplet wave

functions become

$$\Psi_S = \frac{1}{\sqrt{2}} \left(\phi_a(\mathbf{r}_1)\phi_b(\mathbf{r}_2) + \phi_a(\mathbf{r}_2)\phi_b(\mathbf{r}_1) \right) \chi_S \tag{1.7a}$$

$$\Psi_T = \frac{1}{\sqrt{2}} \left(\phi_a(\mathbf{r}_1)\phi_b(\mathbf{r}_2) - \phi_a(\mathbf{r}_2)\phi_b(\mathbf{r}_1) \right) \chi_T \tag{1.7b}$$

where the spatial parts are given explicitly and $\chi_{S/T}$ describe the spin part from eqs. (1.5). By definition the energies of each state is given by $E_{S/T} = \iint \mathrm{d}\mathbf{r}_1 \mathrm{d}\mathbf{r}_2 \Psi^*_{S/T} \mathcal{H} \Psi_{S/T}$ (* denotes complex conjugate), which means that the energy difference is given by

$$E_S - E_T = \iint \mathrm{d}\mathbf{r}_1 \mathrm{d}\mathbf{r}_2 \psi_a(\mathbf{r}_1)^* \psi_b(\mathbf{r}_2)^* \mathcal{H} \psi_a(\mathbf{r}_2)\psi_b(\mathbf{r}_1) \equiv J/2 \tag{1.8}$$

which is known as the *exchange integral* and J as the *exchange constant*. This explicitly shows that the energy difference between the two-electron states is given by the spatial overlap of the atomic orbitals. If the combined symmetry of the molecule and the atomic orbitals is such that the integral is positive, $E_S > E_T$ and nature prefers the triplet state with aligned spins, while a different symmetry may lead to a negative integral and a singlet ground state. This shows why molecular symmetry is crucially important for the coupling between magnetic centres: control of the symmetry offers control of orbital overlaps, and hence, the coupling.

The derivation of the general case where a molecule contains more than two magnetic centres and each centre contains more than one electron is beyond the scope of this introduction. However, the result is remarkably similar to the case described above. Most often, the constant first term in e.q. (1.8) is ignored and the Hamiltonian becomes

$$\mathcal{H} = -\sum_{i,j} J_{ij} \mathbf{S}_i \cdot \mathbf{S}_j \tag{1.9}$$

where the i and j runs over all magnetic centres in the molecule, the electron spin operators $\mathbf{s}$ have been replaced by the ionic spin operators $\mathbf{S}$ and J_{ij} parameterises the coupling between ions on site i and j. This is known as the *Heisenberg Hamiltonian*. In this particular form J_{ij} is assumed to be isotropic (i.e. a number), which covers nearly all physical cases. In principle, however, J_{ij} can be a 3×3 symmetric matrix with specific coupling constants for each set of components of $\mathbf{S}_i$ and $\mathbf{S}_j$.

1.3.1 CEF Effects in Strongly Coupled Systems

The ionic spins in eq. (1.9) can of course also have orbital angular momentum. Then, it is necessary to add a term like eq. (1.3) to the Hamiltonian for each centre in the molecule and the Hamiltonian becomes

$$\mathcal{H} = -\sum_{i,j,i\neq j} J_{ij} \mathbf{S}_i \cdot \mathbf{S}_j + \sum_i \sum_{k,q} \left(B^q_k \hat{O}^q_k \right)_i \tag{1.10}$$

However, the number of parameters grows rapidly, and for molecules with many centres with large multiplicity their experimental determination becomes practically impossible. Instead, it can sometimes be feasible to treat the whole molecule as a single spin entity with multiplicity equal to that of the ground state produced by the pure Heisenberg Hamiltonian (eq. (1.9)). This way, it is possible to determine some effective Steven's parameters to describe the ZFS within the ground manifold, as has e.g. been done for Mn_{12} [40], [41]. This approach, usually referred to as the *giant-spin approximation* (GSA), is valid only when no excited spin manifolds have significant thermal population, i.e. when the gap between the ground state and the lowest-lying spin manifolds is significantly larger than k_BT [38].

1.4 Valence Delocalisation

Valence delocalisation is a phenomenon that can occur in chemical compounds that contain ions in formally different oxidation states. Therein, electronic degeneracy can cause the extra electron(s) to be shared amongst the formally different centres making them (near-)equivalent. Spin polarisation is a necessary prerequisite for delocalisation between centres containing localised valence electrons, a mechanism that contributes (usually ferromagnetically) to intramolecular magnetic couplings. This phenomenon, usually referred to as double exchange, was first described by Zener as an explanation for ferromagnetic coupling in manganese perovskites [42]. Later, Anderson and Hasegawa further developed the theory [43].

The simplest valence-delocalised system is a mixed-valence dimer, and there exists several examples in the literature [21], [44]–[57]. These usually contain several localised valence electrons in addition to the delocalised, spin-polarised ones. For simplicity, we first describe the case where the delocalised electron is the only valence electron; this simple case already offers valuable insight.

Assume that the electron occupies one of two degenerate atomic orbitals ϕ_a/ϕ_b located on the centres a or b. The introduction of some electronic delocalisation between the sites, parameterised by $\beta = \langle\phi_a|\,\mathcal{H}_{\text{eff}}\,|\phi_b\rangle$, creates the eigenstates $\sqrt{2}\psi_\pm = \phi_a \pm \phi_b$ which are split by $2V_{ab} = 2|\beta|$. The interaction has clearly mixed the atomic orbitals causing the extra electron to simultaneously reside on both a and b in a symmetric or anti-symmetric fashion depending of the sign of β. If the situation is not symmetric the coefficients of $\psi_\pm$ will differ from $\sqrt{2}$ and the eigenstates will retain some atomic orbital character with preferential population of one of the two sites [34].

Based on the above considerations alone, any fully symmetric system with non-zero electronic interaction should be valence delocalised, however that is not the case in real systems. This is because electronic energy levels couple to vibrational degrees of freedom, a phenomenon known as vibronic coupling. Many vibrations can be present at the site of an ion (a or b) and they need not be harmonic. However, the total movement of each atom can be described as harmonic along normal coordinate x as a first-order approximation. Owing to

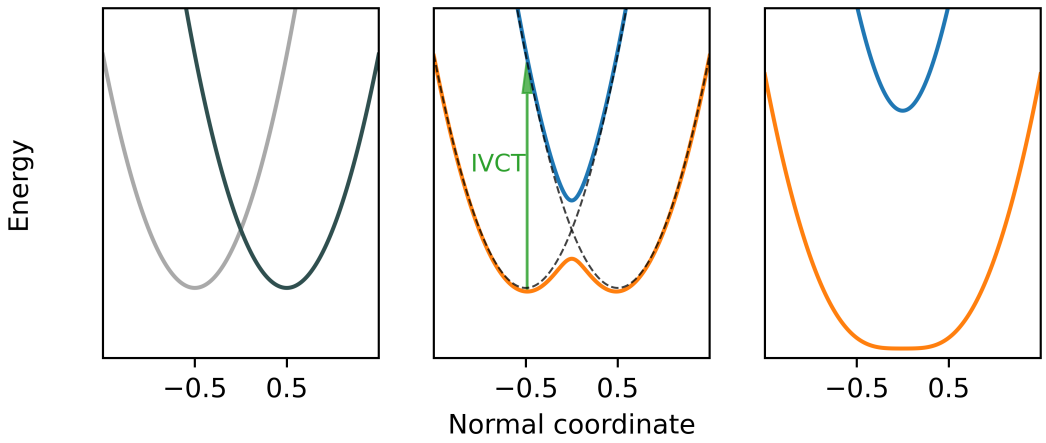

Fig. 1.2. Potential energy surfaces (PESs) for the two-state system described in eq. (1.11) for $\beta = 0$ (left), $\beta = \lambda/8$ (middle) and $2\beta > \lambda$. Orange and blue curves correspond to the ground and excited coupled states, respectively, and the grey curves correspond to the uncoupled single-site harmonic oscillators. The dashed lines in the middle plot show the coupled single-site oscillators, and the green arrow marks the IVCT band.

the symmetry of the problem, the energy associated with these harmonic vibrations will be $E = \lambda(x + 1/2)^2$ and $E = \lambda(x - 1/2)^2$ for a and b, respectively, where λ is a vibronic coupling parameter. The effect of the electronic interaction is to mix the states with these vibrational energies. In the eigenbasis of the atomic orbitals the total effective Hamiltonian becomes [34]

$$\mathcal{H}_{\text{eff}} = \begin{pmatrix} \lambda(x+1/2)^2 & \beta \\ \beta & \lambda(x-1/2)^2 \end{pmatrix} \tag{1.11}$$

which results in two states with the potential energy surfaces (PESs) shown in Fig. 1.2, which are markedly different depending on the relative magnitudes of $|\beta|$ and λ.

For $\beta = 0$, the PESs do not couple. The minima of the PESs are at $x = \pm 1/2$ and the wave functions are still the atomic orbitals. This case corresponds to class I in the Robin-Day classification scheme for mixed-valence compounds [20], [58].

A moderate $|\beta| < \lambda/2$ leads to minima close to but different from $x = \pm 1/2$, values of x where the eigenstates of $\mathcal{H}_{\text{eff}}$ are still mostly ϕ_a/ϕ_b in nature. Thus, a transition from the lower to the upper PES at fixed x still resembles a charge transfer from a to b (or vice-versa depending of the sign of x). Such transitions can be observed as inter-valence charge transfer (IVCT) bands in visible light spectroscopy [20]. Also, it is possible to go from $x \approx \pm 1/2$ to $x \approx \mp 1/2$ along the lower PES by overcoming a barrier at $x = 0$ with height $E_B = \lambda/4 - |\beta| - \beta^2\lambda$. Thermal fluctuations can induce transitions between these minima if $k_B T$ is comparable to E_B, which leads to T-dependent electron transfer since the wave functions at the minima still have localised natures. This case corresponds to class II in the Robin-Day classification scheme, and the compounds of this class usually have properties originating from both the individual atoms as well as their interaction [20], [58]. The molecules studied in Chapters 4 and 5 belong to this class of mixed-valence compounds.

Fig. 1.3. Schematic of the simplest spin-polarised delocalisation (double exchange) mechanism across two sites with $S_0 = 1/2$. The spins in ϕ_1/ϕ_2 prefer to align due to on-site exchange interactions. Thus, there is a energy cost associated with antiferromagnetic coupling between the core spin on sites a/b since the delocalised electron keeps its projection during transfer.

There exists only one minimum for each PES when $\beta > \lambda/2$. It is located at $x = 0$ where the atomic orbitals are completely mixed and the eigenstates of eq. (1.11) bear no resemblance to localised states. In this case the system has unique properties which are fundamentally different from those of the isolated constituent parts. This corresponds to class III in the Robin-Day classification scheme, which is clearly different from the two previous cases [20], [58]. The recent report of record-breaking magnetic coercivity in a class III lanthanide dimer is an excellent showcase of the unique properties that emerges in this class of compounds [4].

When discussing valence delocalisation in magnetic systems, it is necessary to consider at least two orthogonal atomic orbitals at each site, ϕ_{a1}/ϕ_{a2} and ϕ_{b1}/ϕ_{b2}, occupied by three electrons in total (see Fig. 1.3). According to Hund's first rule, the electrons will singly occupy these orbitals and the spins on each site will align. The ionic spins can then couple via Heisenberg exchange as described by eq. (1.9). For simplicity, we assume that ϕ_{a1} and ϕ_{b1} are always occupied such that the electron transfer occurs between ϕ_{a2} and ϕ_{b2}. If the dimer is antiferromagnetically coupled, the transfer of an electron $\phi_{a2} \leftrightarrow \phi_{b2}$ violates the on-site parallel alignment of the spins, which has an energy cost associated to it (Fig. 1.3 (left)). If the dimer is ferromagnetically coupled, the spin of the transferred electron will already be aligned with that of the core electron and there is no cost associated to the electron transfer (Fig. 1.3 (right)). This exemplifies how valence delocalisation leads to double exchange and spin polarisation. In dimers, double exchange always favours ferromagnetic coupling [34].

The underlying idea can be generalised from the above example, which leads to a spin Hamiltonian that combines Heisenberg (eq. (1.9)) and double exchange [59]

$$\mathcal{H} = -J_{ab}\left[\left(\mathbf{S}_a^a \cdot \mathbf{S}_b^a\right)\mathbf{O}^a - \left(\mathbf{S}_a^b \cdot \mathbf{S}_b^b\right)\mathbf{O}^b\right] + B\mathbf{T}_{ab} \tag{1.12}$$

The subscripts refer to specific sites, while the superscripts refer to the location of the extra electron, which is necessary to track since in influences the spin multiplicities of sites a/b. $\mathbf{O}^\alpha$ is an occupation operator which is equal to the identity operator if the extra electron occupies site α and zero otherwise. $\mathbf{T}_{ab}$ transfers the electron (from a to b or vice-versa) while $B = |\beta|/(2S_0 + 1)$ is the double exchange constant (S_0 is the spin of each site without the extra electron). This form of the Hamiltonian assumes that sites a and b are equivalent.

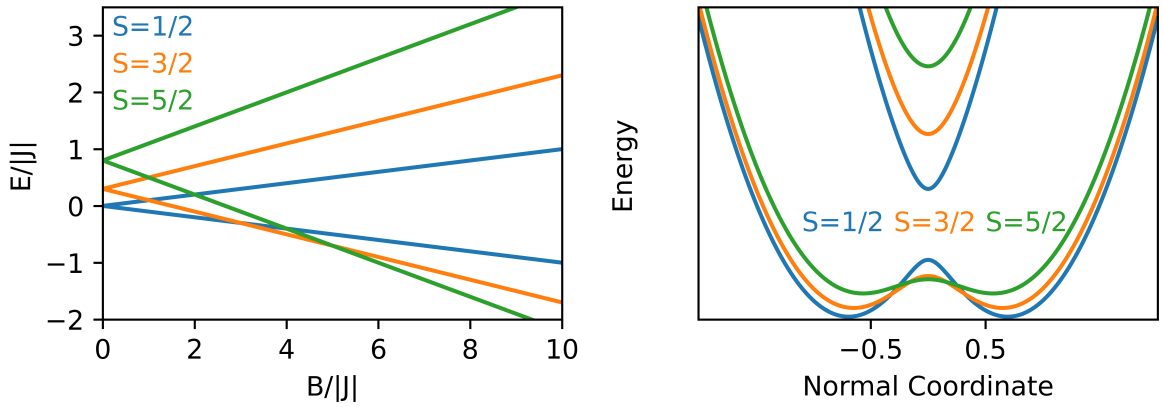

Fig. 1.4. Left: Effect of the relative strength of double and Heisenberg exchange on the eigenenergies of a dimer with $S_0 = 1$ and $J < 0$. **Right:** Effects of vibronic coupling on the PESs a dimer with $S_0 = 1$, $B/|J| = 5.5$ and $J < 0$. With vibronic coupling the ground state has $S = 5/2$, however the vibrations have a localising effect on the lowest-lying PESs which is strongest for low-S states. Consequently, the ground state has $S = 1/2$.

Fig. 1.4 (left) shows the effects of adding double exchange into an antiferromagnetically coupled dimer ($J < 0$); the analytical formula for the eigenenergies is $E = -JS(S+1) \pm B(S+1/2)$ where $S \in [1/2, 3/2, \ldots, 2S_0+1/2]$ is the total spin quantum number. Since the extra electron can be located on either site, each spin state is doubly degenerate in the pure Heisenberg model, and the effect of double exchange is to split these states into symmetric and anti-symmetric linear combinations. It is worth noting that double exchange scales linearly with the total spin in contrast to Heisenberg exchange, which scales as S^2. Consequently, the two mechanisms compete when $J < 0$ and new ground states with intermediate spin can emerge as recently reported (see Fig. 1.4 (left)) [56]. It has been theorised that applying an electric field could bias the potential energy associated with electron transfer, which could perturb the ground state wave function and ultimately change the ground state [14].

Vibronic coupling is also important in magnetic valence delocalised systems: it tends to stabilise states with the smallest S. As described for the non-magnetic case, the effects of vibronic coupling depends on the ratio of the vibronic coupling parameter λ and the splitting Δ between the linear combinations of the localised orbitals. In the present case, these linear combinations are the states with equal S, and their splitting depends on S as $\Delta = 2B(S + 1/2)$. Meanwhile, λ remains unchanged. Therefore, when S is small, Δ may be significantly smaller than λ, which leads to a class II-like situation ($\Delta < \lambda/2$). Yet, for large S, Δ can be larger than $\lambda/2$ and a class III-like situation is retained. Thus, the influence of the vibronic coupling parameter effectively becomes smaller for large S [60]. While this is a qualitative argument, adding a vibronic coupling term to the Hamiltonian in eq. (1.12) has exactly the predicted effect. Fig. 1.4 (right) shows the resulting PESs and its is clear how the lowest-lying $S = 1/2$ state is stabilised more than the $S = 5/2$ state [56].

Despite the focus on dimeric systems in this section, valence delocalisation is not limited to two-site systems. However, explicit treatment of larger systems quickly becomes prohibitively complicated and are outside the scope of this introduction. A general solution to

the Heisenberg-double exchange problem is known and have been implemented in code for isotropic spins [25], [61]. The generalised form of the total Hamiltonian is [25]

$$\mathcal{H} = \begin{bmatrix} \mathcal{H}_{\text{HE}}(D_1) + U(D_1) & \mathcal{T}_{12} & \mathcal{T}_{13} & \cdots \\ \mathcal{T}_{21} = \mathcal{T}_{21}^T & \mathcal{H}_{\text{HE}}(D_2) + U(D_2) & \mathcal{T}_{23} & \cdots \\ \mathcal{T}_{31} = \mathcal{T}_{21}^T & \mathcal{T}_{32} = \mathcal{T}_{21}^T & \mathcal{H}_{\text{HE}}(D_3) + U(D_3) & \cdots \\ \vdots & \vdots & \vdots & \ddots \end{bmatrix} \tag{1.13}$$

where $\mathcal{H}_{\text{HE}}(D_i)$ is the Heisenberg Hamiltonian governing the localised system with a certain distribution D_i of the extra electron(s). The location of only one electron differs between two distinct distributions D_i/D_j. $U(D_i)$ is the orbital energy related to a particular D_i. The Hilbert space of the Hamiltonian is spanned by a combination of the product states $|(S_1, m_{S_1})(S_2, m_{S_2})\cdots\rangle$ of each H_{HE} and the electron distribution space. Thus, for a situation where $\mathcal{T}_{ij} = 0$, the subspace corresponding to each block-diagonal element is spanned by the basis vectors of the corresponding Heisenberg Hamiltonian.

$\mathcal{T}_{ij}$, the transfer matrix, connects two distributions and is given by [61]

$$\mathcal{T}_{ij} = t_{ij} \sum_{\sigma} c^{\dagger}_{j\phi\sigma} c_{i\phi\sigma} \tag{1.14}$$

where t_{ij} is an effective double exchange parameter that, similarly to β, governs electron transfer between sites i and j. $c/c^{\dagger}$ are the creation and annihilation operators for an electron in orbital ϕ with projection σ on site i/j. The sum contains two terms, $\sigma = \pm 1/2$, corresponding to the two possible projections of an electron spin.

Evidently, the effect of double exchange is to mix the subspaces with the extra electron(s) residing on particular sites. In other words, double exchange mixes the Heisenberg-only systems defined by the electron distributions D_i. As a consequence, more parameters need to be defined for each pair of sites. For example, up to three J-parameters are needed: $J_{ij}^{d^n - d^n}$ for when neither site has an extra electron, $J_{ij}^{d^n - d^{n+1}}$ for when either site has an extra electron and $J_{ij}^{d^{n+1} - d^{n+1}}$ for when both sites have extra electrons. Analogously, two sets of e.g. anisotropy parameters and **g**-tensors should be associated to each site. This model assumes that a site never accommodates more than one delocalised electron, which is a valid approximation considering Coulomb repulsion.

The most important new phenomena that emerge when introducing electron delocalisation into systems with more than two sites is that the double exchange can become antiferromagnetic, that the sign of t_{ij} becomes important and that the number of available states increases rapidly when more electron distributions are available [62], [63]. Thus, the characteristics of double exchange being present in a system is the existence of more spin states and the atypical scaling of their eigenenergies as a function of the spin quantum number. The effect of double exchange in specific systems will be discussed in Chapters 4 and 5.

Chapter 2

Experimental Methods and Modelling

This chapter contains an overview of inelastic neutron scattering (INS), the most important experimental method for the work presented in Chapters 3-5. At first, the underlying theory for INS is laid out together with a short overview of instrumentation and the most important experimental considerations. Lastly, an introduction to state-of-the-art spin Hamiltonian modelling tools is given.

2.1 Inelastic Neutron Scattering

INS is an advanced spectroscopic technique capable of probing vibrational and magnetic dynamics within materials. It is sensitive to vibrational dynamics due to neutrons interacting with the nuclei in the sample via the strong force. The sensitivity to magnetic dynamics comes from the neutron magnetic moment interacting with the unpaired electrons within the sample via the electromagnetic force [64], [65]. Magnetic nuclei are only important for magnetic INS if the hyperfine coupling is significant since their magnetic moments are three orders of magnitude smaller than those of unpaired electrons [33].

The observables in an INS experiment are the neutron energy transfer, $\hbar\omega = \hbar^2(\mathbf{k}_i^2 - \mathbf{k}_f^2)/2m_n$, and the scattering angle, 2θ, from which the change of neutron momentum, $\hbar\mathbf{Q} = \hbar(\mathbf{k}_i - \mathbf{k}_f)$ can be deduced. $Q = |\mathbf{Q}|$ is related to the scattering angle as $Q = 4\pi\sin(\theta)/\lambda$, where λ is the de Broglie wavelength of the neutron. Fig. 2.1 shows a schematic of a scattering event [65]. Note that neutron energy loss is defined as positive energy transfer.

Neutrons used for experiments are moderated to have energies of the same order of magnitude as the dynamics under investigation (usually 1-100 meV). Thus, $\hbar\omega$ is easily detectable since it is a significant fraction of the neutron's initial energy. Thereby, one directly probes the excitation energy E since $E = \hbar\omega$ due to energy conservation. Furthermore, the wavelengths of neutrons in the concerned energy range are such that reasonable scattering angles, typically around $10° - 100°$, provide access to portions of reciprocal space large enough for obtaining significant spatial information about the investigated dynamics.

Another convenient property is that neutron-matter interactions are weak due to the nature of the strong force, the small magnetic moment of neutrons, and because neutrons have no electric charge [64]. Therefore, neutrons can penetrate deep into samples and probe their true bulk properties. Another unique advantage is that INS probes magnetic excitations directly

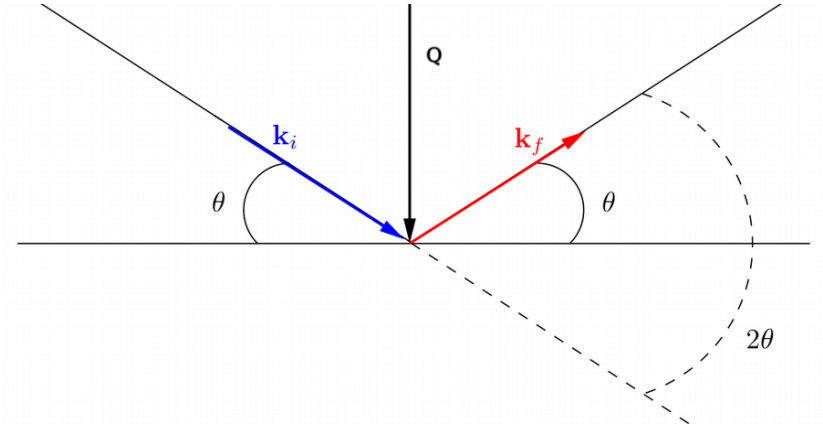

Fig. 2.1. Scheme of the geometry of a scattering event. A neutron with a defined momentum $\hbar\mathbf{k}_i$ is scattered and it's final momentum, $\hbar\mathbf{k}_f$, is measured. The *scattering angle* 2θ, is the in-plane rotation of the neutron wave vector, and $\mathbf{Q} \equiv \mathbf{k}_i - \mathbf{k}_f$ is the *scattering vector*. Figure adapted from [66].

in the absence of magnetic fields in contrast to EPR and FIRMS.

Quantum mechanics governs the neutron scattering process, hence INS should be described in a quantum mechanical framework. Fermi's Golden Rule quantifies the probability density for a system, subject to a potential $\hat{V}$, to transition from one quantum state into another [35]. It can be used to derive an expression for the *partial differential cross section*, a system's ability to scatter neutrons with a final energy in the infinitesimal range $[E_f{:}E_f + dE_F]$ into an infinitesimal solid angle $d\Omega$, commonly known as the master equation for INS [64]:

$$\begin{aligned}\frac{d^2\sigma}{dE_f d\Omega} &= \left(\frac{m_N}{2\pi\hbar^2}\right)^2 \frac{k_f}{k_i} e^{-2W} \sum_{n,m} p_n \left|\langle \mathbf{k}_i, \psi_n | \, \hat{V} \, | \mathbf{k}_f, \psi_m \rangle\right|^2 \delta(E_n - E_m + \hbar\omega) \\ &= \left(\frac{m_N}{2\pi\hbar^2}\right)^2 \frac{k_f}{k_i} S(\mathbf{Q}, \omega)\end{aligned} \tag{2.1}$$

Here m_n is the neutron mass and k_i/k_f are the magnitudes of the initial and final neutron wave vectors, respectively. The bra and ket refer to the initial and final quantum states of the neutron-scatterer system, respectively, and the sum runs over all initial and final states. $\hat{V}$ is the scattering potential and the δ-function ensures energy conservation. The equation describes a system in thermal equilibrium with Boltzmann population p_j of the initial state. Fermi's Golden Rule relies on the *Born approximation*, which implies that all scatterers interact with the unperturbed neutron beam; a good approximation since neutron-matter interactions are weak [64]. $S(\mathbf{Q}, \omega)$ is the measurable quantity [65].

When neutrons scatter from a periodic structure, the average displacement of the scatterers from their equilibrium position influences the neutron intensity. This is accounted for by the so-called *Debye-Waller* factor, e^{-2W}, in eq. (2.1) [64], [67]. It is equal to unity for $Q = 0$ and decreases with increasing Q. Formally, W is a function of $\mathbf{Q}$ and different for each type of scatterer in a system. In practice, it is essentially always assumed that the average

Element	Fe	N	C	O	$^{1}_{1}$H	$^{2}_{1}$H
σ_{inc} (barn, 10^{-24} cm^2)	0.4(11)	0.5(12)	0.001(4)	0.000(8)	80.26(6)	2.05(3)

Table 2.1. Table of the nuclear incoherent neutron scattering cross sections, σ_{inc}, of most common constituents of molecular magnets, taken from the ILL neutron data booklet [68].

displacement is isotropic and consequently that W depends on Q only. Phenomenologically, this mechanism can be understood by recalling that large Q corresponds to short distances in real space. Thus, at large Q, one probes dynamics at short length scales. As Q increases, the characteristic length scale of the dynamics approaches the average displacement of the scatterers, which causes the scattered neutrons to be out of phase and the overall intensity decreases. The decay at large Q due to the Debye-Waller factor will be more significant at higher temperatures since thermal motion, and thus the mean displacement, increases with temperature. The effect is also present at very low temperatures due to zero-point motion.

2.1.1 Nuclear INS

The Fermi pseudo-potential governs the interaction between neutrons and the nuclei in the system [65]

$$\hat{V}_{nuc}(\mathbf{r}) = \frac{2\pi\hbar^2}{m_n} b_j \delta(\mathbf{r} - \mathbf{r}_j) \tag{2.2}$$

where b_j is the scattering length of nucleus j. The δ-function emphasises that the nuclei are treated as points, a valid approximation since the nuclei are orders of magnitude smaller than the typical neutron wavelength (1-10 Å). Inserting $\hat{V}_{nuc}$ into eq. (2.1) reveals that the nuclear partial differential cross section is a sum of two distinct contributions: 1) The coherent part, which depends on the correlation between all scatterers within the neutron's coherence volume, e.g. the collective motion of particles in a lattice, and 2) the incoherent part, which depends on the self-correlation of individual particles, i.e. rattling of single atoms. In other words, inelastic nuclear scattering comes from the vibrational dynamics within the sample. For molecular crystals, the incoherent vibrations usually contribute more to the measured INS spectrum. A common trait for both types of vibrational scattering is that for small Q, where the Debye-Waller factor is near constant, the measurable $S(\mathbf{Q}, \omega)$ scales as Q^2 [64].

The coherent and incoherent cross sections of an isotope can be vastly different and can vary significantly from one isotope to the next. Tab. 2.1 shows the nuclear incoherent cross sections, σ_{inc}, of the most common constituents of molecular magnets [68]. Note that σ_{inc} changes drastically from hydrogen to deuterium. Thus, one can minimise incoherent nuclear scattering by deuterating a sample, for example to minimise the background when studying magnetic excitations. If the energy scale of the magnetic interactions significantly overlaps with that of incoherent vibrations, deuteration is vital for the success of the experiment.

2.1.2 Magnetic INS

The electromagnetic interaction between the neutron magnetic moment and the unpaired electrons within the sample is mathematically similar to the Fermi pseudo-potential. For an atom with unpaired electrons located at $\mathbf{r}_j$ the potential is given by [65]

$$\hat{V}_{mag}(\mathbf{r}) = \frac{2\pi\hbar^2}{m_N} p_j F_j(Q)\delta(\mathbf{r} - \mathbf{r}_j) \tag{2.3}$$

where p_j is the linear momentum of atom j and the δ-function again specifies that the magnetic atoms are treated as points. F_j is the *magnetic form factor* of site j, which is defined as the spatial Fourier transform of the normalised unpaired electron density. While F_j's are generally element- and oxidation state specific, they are always equal to unity at $Q = 0$ and decay smoothly with increasing Q. Significant effort was put into calculating and measuring magnetic form factors in the 1960's [69]–[71], however nowadays they are parameterised using spherical Bessel functions and tabulated in e.g. Ref. [72].

Inserting eq. (2.3) into eq. (2.1) and treating only finite magnetic systems with defined magnetic centres yields the partial differential cross section for molecular magnets [65],

$$\frac{d^2\sigma}{dE_f d\Omega} = \frac{A}{N}\frac{k_f}{k_i}\sum_{n,m} p_n I_{nm}(\mathbf{Q})\delta(E_i - E_f + \hbar\omega) \tag{2.4}$$

where the constant $A = 0.29$ barn collects all prefactors and N is the number of magnetic centres. I_{nm}, which contains all $\mathbf{Q}$-dependent information, is given by [65]

$$I_{nm}(\mathbf{Q}) = \sum_{j,j'} F_j^*(Q)F_{j'}(Q)e^{-i\mathbf{Q}\cdot\mathbf{R}_{j,j'}} \sum_{\alpha,\beta}\left(\delta_{\alpha,\beta} - \frac{Q^\alpha Q^\beta}{Q^2}\right)\langle n|\,\hat{s}_j^\alpha\,|m\rangle\langle m|\,\hat{s}_{j'}^\beta\,|n\rangle \tag{2.5}$$

where the j, j'-sum runs over all sites and the α, β-sum runs over the Cartesian coordinates. $\mathbf{R}_{j,j'}$ is the vector separating magnetic centres at $\mathbf{r}_j$ and $\mathbf{r}_{j'}$ while $\delta_{i,j}$ is Kronecker's delta. The n and m brakets denote the initial and final state of the sample, respectively, and $\hat{s}_k^\kappa$ is the spin operator of site k along the direction κ (see eq. (1.1)). The factor $(\delta_{\alpha,\beta} - Q^\alpha Q^\beta/Q^2)$ describes how neutrons only couple to the parts of the magnetic moments perpendicular to the neutron wave vector; a key result in magnetic INS.

Eq. (2.5) contains the time and space Fourier transform of the dynamical spin pair correlation function for all permutations of site pairs and Cartesian coordinates. This explicitly shows how the partial differential cross section depends on the relative positions of the magnetic centres and the wave functions involved in a particular magnetic excitation, which highlights the plethora of information available in an INS experiment. Eqs. (2.4) and (2.5) are exactly computable if three things are known: 1) The relative positions of the magnetic atoms in the investigated molecule, 2) the eigenvalues of the governing spin Hamiltonian, and 3) the eigenvectors corresponding to each eigenvalue. Thus, modelling of molecular magnet

INS data with Hamiltonian models is well developed as will be elaborated in Section 2.2.

The explicit dependence on the spin operators $\hat{s}_k^\kappa$ implies that excitations must obey the selection rules $\Delta S = 0, \pm 1$ and $\Delta m_S = 0, \pm 1$, which emphasises another unique trait of magnetic INS: inter-spin multiplet excitations can be directly probed. These rules, together with the dependence of the Boltzmann population, make precise temperature control imperative during an INS experiment. Cooling to temperatures close to absolute zero (typically a few Kelvin) ensures that only the ground state is populated. Thus, the nature of the observed excitations are more clear thanks to the selection rules. However, the amount of available states are also limited. Heating the sample will thermally populate excited states and new excitations may be allowed.

Note also that I_{nm} is proportional to the magnetic form factors. Thus, magnetic excitations are most intense at low Q and decay as Q increases. This behaviour is opposite to that of vibrational excitations at low Q and is used distinguish magnetic and vibrational excitations.

In order to obtain the full 3D **Q**-dependence of the investigated excitations, experiments need to be performed on oriented single crystals. This is often a big challenge since large crystals (masses on the gram scale) are needed due to the weak nature of neutron-matter interactions. Therefore, researchers often compromise and instead study polycrystalline samples for which obtaining gram-scale amounts is more feasible. In such cases, all directions in momentum space are probed simultaneously, and the measured spectrum depends only on Q. The that case, $I_{nm}(\mathbf{Q})$ in eq. (2.4) is replaced by its averaged form [73]:

$$\begin{aligned} I_{nm}(Q) = \sum_{jj'} F_j^*(Q) F_{j'}(Q) \Bigg\{ & \frac{2}{3}\left[j_0 + c_0^2 j_2\right] \tilde{s}_j^z \tilde{s}_{j'}^z + \frac{2}{3}\left[j_0 - \frac{1}{2} c_0^2 j_2\right] \left(\tilde{s}_j^x \tilde{s}_{j'}^x + \tilde{s}_j^y \tilde{s}_{j'}^y\right) \\ & + \frac{j_2}{2}\left[c_2^2 (\tilde{s}_j^x \tilde{s}_{j'}^x - \tilde{s}_j^y \tilde{s}_{j'}^y) + c_{-2}^2 (\tilde{s}_j^x \tilde{s}_{j'}^y + \tilde{s}_j^y \tilde{s}_{j'}^x)\right] \\ & + j_2\left[c_1^2 (\tilde{s}_j^z \tilde{s}_{j'}^x + \tilde{s}_j^x \tilde{s}_{j'}^z) + c_{-1}^2 (\tilde{s}_j^z \tilde{s}_{j'}^y + \tilde{s}_j^y \tilde{s}_{j'}^z)\right] \Bigg\} \end{aligned} \tag{2.6}$$

where j_0/j_2 are the spherical Bessel functions, which are functions of $Q|\mathbf{R}_{j,j'}| = QR_{j,j'}$, and the dynamical spin pair correlations are short-handed as $\tilde{s}_j^\alpha \tilde{s}_{j'}^\beta = \langle n| \hat{s}_j^\alpha |m\rangle\langle m| \hat{s}_{j'}^\beta |n\rangle$. The constants c_a^b are given by

$$\begin{gathered} c_0^2 = \frac{1}{2}\left[3\left(\frac{R_{j,j'}^z}{R_{j,j'}}\right)^2 - 1\right], \quad c_1^2 = \frac{R_{j,j'}^x R_{j,j'}^z}{(R_{j,j'})^2}, \quad c_{-1}^2 = \frac{R_{j,j'}^y R_{j,j'}^z}{(R_{j,j'})^2} \\ c_2^2 = \frac{(R_{j,j'}^x)^2 - (R_{j,j'}^y)^2}{(R_{j,j'})^2}, \quad c_{-2}^2 = 2\frac{R_{j,j'}^x R_{j,j'}^y}{(R_{j,j'})^2} \end{gathered} \tag{2.7}$$

where $R_{j,j'}^\alpha$ is the length of component α of $\mathbf{R}_{j,j'}$.

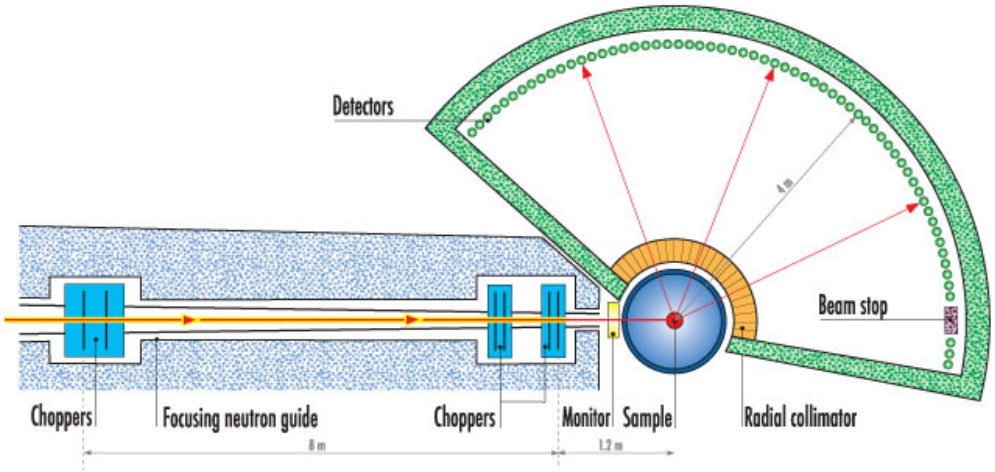

Fig. 2.2. Schematic of the direct geometry cold neutron time-of-flight disk chopper spectrometer IN5 at Institut Laue-Langevn in Grenoble, France [74].

2.1.3 Time-of-Flight INS

Neutron spectrometers can be built in a few different ways, but one particular kind is most commonly used for studies of magnetic excitations within molecules: direct geometry time-of-flight (df-TOF) spectrometers. These spectrometers can measure large portions of $\mathbf{Q}, \omega$-space simultaneously which makes them ideal for measuring excitations that are not dispersive in Q. An example of such a spectrometer is IN5 at Institute Laue-Langevin (ILL) in Grenoble, France, of which Fig. 2.2 shows a schematic [75]. In general terms, dg-TOF spectrometers function by having short, well-timed pulses of neutrons with well-defined energies arrive at the sample position at a precisely defined time. This allows for the flight time after scattering, t_F, to be measured alongside the scattering angle 2θ. The distance from the sample position to the detector, L, is also known, from which the final neutron energy E_f and momentum transfer Q are found as [76]

$$\begin{gathered} k_f = \frac{m_N L}{\hbar t_F}, \qquad E_f = \frac{\hbar^2 k_f^2}{2m_N} = \frac{m_N L^2}{2t_F^2}, \\ \frac{\hbar^2 Q^2}{2m_N} = E_i + E_f - 2\cos(2\theta)\sqrt{E_i E_f} = Ei + \frac{m_N L^2}{2t_F^2} - \cos(2\theta)\frac{L}{t_F}\sqrt{2E_I m_N} \end{gathered} \tag{2.8}$$

If the sample is an oriented single crystal and the spectrometer is equipped with position-sensitive detectors, one obtains the four-dimensional $S(\mathbf{Q}, \omega)$ from an experiment (eq. (2.5)). When polycrystalline samples are used, the powder-averaged $S(Q, \omega)$ is obtained (eq. (2.6)).

The spectrometer layout has important implications for its performance. ILL is a reactor-based neutron source, which provides a steady neutron beam. IN5 therefore uses disk choppers to monochromate the beam and cut it into the initial neutron pulses. The biggest source of background in this type of spectrometers are dark counts and counts from rogue neutrons that do not follow the intended flight path. Since the amount of dark counts do not change

over time, the background signal will be approximately flat in the time domain, however in the energy domain the background scales as $(\hbar\omega)^4$ due to the transformation in eq. (2.8).

Another general feature of dg-TOF spectrometers is that the energy resolution depends on $\hbar\omega$; it is widest at large negative $\hbar\omega$ and narrows smoothly towards the minimum at largest attainable $+\hbar\omega$. The exact shape depends on the instrument, and for IN5 the resolution is approximately constant for $\hbar\omega \geq 0$ when low-energy neutrons are used.

To optimise the energy resolution and remove background, IN5 uses a pair of counter-rotating choppers to pulse and monochromate the beam. Their rotation speed can be used to balance resolution and neutron flux, and the phasing of the choppers controls the energy of the monochromated neutrons. For the typical speed of 12000 RPM, the resolution full-width-at-half-maximum at $\hbar\omega = 0$ is ≈ 2 % of E_i. Two additional chopper pairs clean the neutron beam: one removes contamination from harmonics and one deals with the frame overlap, i.e. makes sure that no fast neutrons catches up to the slowest neutrons from the previous pulse. A radial collimator hinders neutrons scattered by the sample environment from reaching the detectors.

2.1.4 INS studies of Magnetic Molecules

INS has a long history of providing unprecedented experimental insight into the spin dynamics of magnetic molecules. Experiments on polycrystalline samples provided the first direct, zero-field evidence for the anisotropy parameters responsible for quantum tunneling of the magnetisation in Mn_{12}, time-resolved INS elucidated Mn_{12}'s magnetic relaxation and in 2017 single-crystal INS finally pinned down the magnetic interactions within Mn_{12} 18 years after the initial INS studies [40], [41], [77], [78].

Following a significant leap forward in instrumentation in the late 2000's, INS continued to provide unique information on magnetic molecules. Experiments performed on single crystals revealed Néel vector tunneling in a Cr_8 ring molecule, entanglement between two Cr_7Ni molecular qubits, and oscillations of the total spin of Cr_7Ni entities upon application of a magnetic field [79]–[81]. Kofu et al directly probed hyperfine coupling within a Tb-Cu dimer and elucidated its magnetic relaxation via so-called quasi-elastic neutron scattering [82], [83]. Very recently, it was shown that INS spectra also contain information about the coupling of magnetic and vibrational degrees of freedom within molecules, which makes the technique well suited for studying valence delocalised molecules [84].

2.2 Spin Hamiltonian Modelling

Spin Hamiltonian modelling is the premier tool employed to interpret INS and other spectroscopic data of magnetic polynuclear metal complexes. At its core, the methodology can be boiled down to three essential steps: 1) Construct a suitable Hamiltonian model capable of explaining all observables, 2) Fit the parameters of the model to obtain the best agree-

ment between model and observables, and 3) Interpret the physical properties that emerge from the best set of parameters. This approach is particularly well suited for INS since the observable $S(\mathbf{Q}, \omega)$ for any model can be computed directly from the Hamiltonian eigenvalues and -vectors and the related spin operators as outlined in eq. (2.4). In addition, only a few experimental prefactors need to be taken into account. Still, it can be necessary to make approximations or combine several experimental methods to constrain all parameters of a suitable Hamiltonian model as will be elaborated in Chapter 3.

The dimensionality of a Hamiltonian matrix increases rapidly when the model becomes more complex, hence its construction and diagonalisation is usually handled by tailor-made computer programs like *mint* or MAGPACK for INS and Easyspin or PHI for e.g. EPR [27], [28], [85], [86]. Systems governed by most types of magnetic interactions can be constructed within these programs, however none of them incorporates double exchange (eq. (1.13)). One program, MVPACK, can tackle systems governed by double exchange, however it is limited to calculations of bulk magnetometry measurements of isotropic spin systems [25].

For this thesis, we have implemented the general solution to the double exchange problem within the framework of Easyspin and *mint* [61]. With this tool, it is possible to construct arbitrary spin Hamiltonian models governed by double exchange and all other interactions built into Easyspin using a coding formalism familiar to Easyspin users. One can furthermore define oxidation-state dependent parameters to e.g. account for the difference in $3d^5 - 3d^5$ and $3d^5 - 3d^6$ Heisenberg exchange interactions. Models incorporating double exchange are fully compatible with all *mint* functions, and the tool also outputs the magnetic dipole operators for use in all Easyspin functions. This provides two major benefits compared to MVPACK: 1) Single-ion anisotropy can be included in the spin Hamiltonian alongside double exchange and 2) INS (and soon EPR) spectra can easily be calculated using the built-in functions of *mint* (and Easyspin). These features were essential for the work presented in Chapter 4. In that work, our new tool revealed that INS could be able to provide a quantitative handle on the distribution of electrons with valence delocalised molecules, a hypothesis we investigate further in Chapter 5.

The trade-off for using our tool instead of MVPACK is that the matrices can become prohibitively large because Easyspin and *mint* uses the product state formalism. In contrast, MVPACK uses the coupled basis and takes full advantage of the irreducible tensor operator formalism, whereby the Hamiltonian is broken down into block-diagonal elements. For example, the full matrix for a system with six coupled $3d^5$ sites and two delocalised electrons has dimensionality 468000x468000 in the product state basis, whereas the largest spin block is 7050x7050 in the coupled basis. If the community is interested in calculating INS and EPR spectra of larger delocalised molecules it could be worth to further develop our tool.

Chapter 3

Manuscript 1: Combining Spectroscopies to Unravel Strong Exchange Interactions within Radical-Bridged Iron(III) Dimers

3.1 Prelude to Chapter

The research presented in this chapter sought to figure out how to probe molecular spin dynamics within molecules with strong intramolecular exchange interactions caused by e.g. double exchange or direct exchange between metal centres and radical ligands. For sufficiently large couplings, the gap to excited spin manifolds can approach or even surpass $\Delta/k_B = 300$ K, which makes modelling of the temperature-dependence of the magnetic susceptibility unreliable. INS can also fall short in these cases because instrumental limitations prevents probing the low-Q region of $S(\mathbf{Q}, \omega)$ for short neutron wavelengths, which causes magnetic transitions to be weak due to the magnetic form factor.

We found that it is possible to combine several spectroscopic techniques that are sensitive to different terms in the magnetic Hamiltonian and thereby obtain insight no single method could provide. In particular, we used INS, high-frequency (HF) EPR, FIRMS and magnetometry to probe magneto-structural correlations in a series of radical-bridged Fe^{3+} dimer molecules. INS and HF EPR gave access to the magnetic anisotropies (e.q. (1.3)), and modelling of the latter yielded the **g**-tensors of the investigated molecules. With this knowledge, we could extract the Heisenberg exchange couplings from FIRMS and magnetometry data, which would not have been reliable without the prior information obtained from INS and HF EPR.

This work does not directly involve valence delocalised molecules, however it addresses an issue relevant for future studies of such molecules. Valence delocalised molecules, especially dimers, are usually strongly coupled, and the experimental campaign presented here is directly portable to such systems [21], [50], [56].

We intend to submit this draft to a chemistry journal. Information about individual contributions can be found in within the ”Contributions” section within manuscript.

Combining Spectroscopies to Unravel Strong Exchange Interactions within Radical-Bridged Iron(III) Dimers

R. T. Christiansen,[†,‡,¶] W. Zheng,[§] A.-L. Barra,[‖] F. Le Mardelé,[‖] M. Orlita,[‖,⊥] A. I. Kolesnikov,[#] M. Appel,[†] R. Clérac,[@] J. Ollivier,[†] S.-Q. Wu,[§] O. Sato,[§] and M. L. Baker*[,‡,¶]

†*Spectroscopy Group, Institut Laue-Langevin, 38042 Grenoble Cedex 9, France*

‡*Department of Chemistry, The University of Manchester, Manchester M13 9PL, UK*

¶*The University of Manchester at Harwell, Diamond Light Source, Didcot, Oxfordshire, OX11 0DE, UK*

§*Institute for Materials Chemistry and Engineering, Department of Fundamental Organic Chemistry, Kyushu University, Fukuoka 819-0395, Japan*

‖*LNCMI-EMFL, CNRS UPR3228, Université Grenoble Alpes, Université Toulouse, Université Toulouse 3, INSA-T, 38042 Grenoble and Toulouse Cedex 9, France*

⊥*Faculty of Mathematics and Physics, Charles University, 121 16 Prague, Czech Republic*

#*Neutron Scattering Division, Oak Ridge National Laboratory, Oak Ridge, TN 37831, USA*

@*Centre de Recherche Paul Pascal, CNRS UMR 5031, 33600 Pessac, France*

E-mail: michael.baker@manchester.ac.uk

Abstract

When the gap between the lowest-lying spin manifolds of a molecule approaches $\Delta/k_B \approx 300$ K one can no longer rely on the temperature-dependence of the molar magnetic susceptibility to get a good estimate of intra-molecular exchange couplings. This works explores using several spectroscopic techniques to probe different terms in the magnetic Hamiltonian and thereby arrive at a unified description of molecular spin dynamics. Specifically, we combine inelastic neutron scattering, high-frequency electron paramagnetic resonance, far infrared magneto-spectroscopy and SQUID magnetometry to elucidate structure-property relationships in a series of newly synthesised iron dimers derived from $[[Fe(cth)]_2(dhbq)]^{3+}$ (H_2dhbq = 2,5-dihydroxy-1,4-benzoquinone; cth = 5,5,7,12,12,14-hexamethyl-1,4,8,11-tetraazacyclotetradecane). These dimers have well-isolated $S = 9/2$ ground states due to strong direct antiferromagnetic exchange between the Fe^{3+} centres ($S = 5/2$) and the radical bridging π ligand ($S = 1/2$). Our combinational approach allows us to determine the parameters of their microscopic Hamiltonians including fourth order Steven's operators and exchange couplings. We find that ligand-to-metal charge transfer, controlled by bridge functionalisation, significantly impacts the magnetic anisotropy, rhombicity, and exchange coupling. Furthermore, we show that imposing centrosymmetry via control of capping ligand chiralities makes the **g**-tensor isotropic, while other parameters remain largely unchanged. The level of detail we obtain exemplifies the capabilities of our experimental approach, which can be directly ported to other studies of molecule-based magnetic compounds.

Introduction

Owing to the remarkable versatility of coordination chemistry, molecule-based magnetic materials continue to find new applications in various quantum technologies and as new permanent magnets.[1–8] In recent years, a particularly successful strategy for creating exciting new compounds has been to incorporate strongly coupled spin centres via direct metal-radical exchange or metal-metal bonding.[8–13] An essential next step towards reaching the full po-

tential of strongly coupled magnetic compounds is to establish quantitative relationships between their structures and the couplings within. However, commonly employed experimental methods such as magnetometry can fall short when the couplings become comparable to or greater than $k_B \cdot 300$ K. Consequently, the elucidation of important structure-property trends remains a formidable challenge to be tackled by experimentalists. Here, we present a methodology capable of this task by combining several spectroscopy methods.

Specifically, we study the effects of chemical tailoring on a family of new radical-bridged Fe^{3+} dimers based on $[[Fe(cth)]_2(dhbq)]^{3+}$ (**A**, cth = 5,5,7,12,12,14-hexamethyl-1,4,8,11-tetraaza-cyclotetradecane; H_2dhbq = 2,5-dihydroxy-1,4-benzoquinone). This molecule, originally investigated by Dei et al,[14] consists of two Fe^{3+} ions (high-spin $3d^5$) which are strongly coupled to a radical $dhbq^{3-}$ π bridge and capped by chiral cth ligands. Our synthesis of new derivatives provides the possibility for investigating the potential avenues for chemical tunability through a comparative study. Also, the methods we employ provide more detailed insight into the properties of derivatives of **A** compared to previous studies.

Molecules closely related to **A** have exciting properties, which further motivates our study. $[Fe(RR{-}cth)Co(SS{-}cth)(dhbq)]^{3+}$, for example, shows electronic pyroelectricity, and the pure Co analogue undergoes a photo-induced valence tautomeric transition from $^{ls}Co^{3+}{-}dhbq^{3-}{-}^{ls}Co^{3+}$ to $^{hs}Co^{2+}{-}dhbq^{2-}{-}^{ls}Co^{3+}$.[15,16] In addition, functionalisation of the dhbq bridge in iron and cobalt dimers capped by TPA(=tris(2-pyridylmethyl)amine) has proven to be a successful strategy for tailoring their magnetic properties,[17–21] and dhbq derivatives are frequently used as linkers in 0D, 1D, 2D, and 3D Fe-based molecular systems.[22–28] These examples highlight the tunability of transition metal (TM) dimers bridged by dhbq derivatives and underline the need for quantifying structure-property relationships to tune the properties of systems incorporating dhbq derivatives as bridging ligands.

Our dimer series consists of three molecules: An enantiopure version of **A** (**1-H**), its analogue with a dcbq bridge (**1-Cl**, H_2dcbq = 3,6-dichloro-2,5-dihydroxy-1,4-benzoquinone), and a racemic version of **A** (**2-H**). The first two have crystallographically different iron

centres, while the iron centres are related by inversion symmetry in the latter. Thus, we investigate two avenues for tailoring the magnetism of our dimers: 1) Increasing the electron withdrawing potential of the radical bridge by Cl substitution and 2) imposing inversion symmetry on the Fe centres via control of the relative capping ligand chirality. Radical ligands have been widely used as building blocks within molecular magnetism and were recently indispensable for building a metal-organic magnet with a record-breaking critical temperature, which shows that tailoring the character of the radical bridge provides a promising avenue for tunability.[8,29] Control of chirality has also proved useful for engineering the properties of both small molecules and extended molecular systems, but quantitative information about its effect on magnetic coupling and anisotropy within molecules is lacking, which motivates exploring this engineering route.[30,31]

We investigate our dimers by combining inelastic neutron scattering (INS), high-frequency electron paramagnetic resonance spectroscopy (HF-EPR), far infrared magneto-spectroscopy (FIRMS), and SQUID magnetometry into a comprehensive experimental approach. These spectroscopic techniques have previously unravelled highly detailed information about magnetic anisotropy and spin dynamics within magnetic molecules.[32–35] Here, they provide access to Fe^{3+}-radical exchange couplings and magnetic anisotropy parameters of the Fe^{3+} sites, including fourth order Steven's operators. From there, we establish structure-property trends that can guide exploration of other coordination compounds utilising metal-radical exchange interactions and chiral ligands. This exemplifies the capabilities of our experimental approach to unravel the microscopic Hamiltonians of molecular systems without overparametrisation, an approach which is directly transferable to studies of other coordination compounds.

Experimental Methods

Samples

We synthesise the dimers using a three-step process: 1) Synthesis of the mononuclear species [Fe(AcO)L](PF_6) with L = *Rac*-cth, *RR*-cth or *SS*-cth (cth = 5,5,7,12,12,14-hexamethyl-1,4,8,11-tetraazacyclotetradecane), 2) synthesis of the dicationic precursor [[FeL]$_2$A](PF_6)$_2$ from the mononuclear analogue with H_2A = 2,5-dihydroxy-1,4-benzoquinone (H_2dhbq) or 3,6-dichloro-2,5-dihydroxy-1,4-benzoquinone (H_2dcbq), 3) oxidation of the dicationic precursor with $AgPF_6$ in solution. The ligands (L) were synthesised using previously reported methods, and other chemicals and solvents were used as purchased from commercial sources.[36]

The crystal structures were determined based on single-crystal X-ray diffraction data collected at T = 100 K on a Rigaku XtaLab Synergy-R/DW diffractometer equipped with a HyPix-6000 area detector using multi-layer mirror monochromated Mo-Kα radiation (λ = 0.71073 Å). The structures were solved by a direct method and refined using full-matrix least-squares on F^2 using the SHELX implemented in the OLEX2. All non-hydrogen atom were refined using anisotropic thermal parameters and the hydrogen atoms were geometrically added and refined by the riding model.[37–39] Complete structural information for the tricationic dimers can be found in Tab. S1.

[Fe(AcO)L](PF_6)

Freshly purchased $Fe(AcO)_2$ (3.3 mmol, 521 mg) and the appropriate ligand (L = *Rac*-cth, *RR*-cth or *SS*-cth, 3.3 mmol, 850 mg) were added to 10 ml EtOH from which dissolved oxygen had been removed by bubbling for several minutes with N_2. The solution was then heated to 70 °C and left until it became brown and transparent. Then, we added NH_4PF_6 (3.3 mmol, 540 mg), and a white solid ([Fe(AcO)L]PF_6) to gradually precipitated accelerated by cooling in an ice bath for 15 minutes. Afterwards, we filtered the white solid and washed it with cold EtOH and ether (yield 980 mg, 54 %, independent of L).

$[[Fe(\boldsymbol{RR}-cth)]_2(dhbq)](PF_6)_3 \cdot H_2O \cdot MeOH$, 1-H

We first mixed H_2dhbq (1 mmol, 140 mg) and triethylamine (2 mmol, 280 μl) in MeOH (50 ml) under the protection of a N_2 flow. Next, [Fe(AcO)(RR−cth)](PF_6) (2 mmol, 1089 mg) was added to the mixture, which was then stirred at 60 °C for 30 min. Afterwards, we added 30 ml of aqueous solution of KPF_6 (1.5 mmol, 276 mg) was to the dark mixture, slowly cooled it to room temperature and left it to precipitate overnight. The dark-grey product, [(Fe(RR−cth))(μ−dhbq)(Fe(RR−cth))]$(PF_6)_2$, was filtered and washed with H_2O (yield 820 mg, 74 %).

The intermediate product, [(Fe(RR−cth))(μ−dhbq)(Fe(RR−cth))]$(PF_6)_2$ (1 mmol, 1109 mg), was then dissolved in 50 ml MeOH, to which an aqueous solution of $AgPF_6$ (1 mmol, 252 mg) was added. The solution was stirred at room temperature for 30 minutes and thereafter filtered multiple times to remove any residual silver. The solution was then gradually evaporated until the crude product, [(Fe(RR−cth))(μ−dhbq)(Fe(RR−cth))]$(PF_6)_3$, fully precipitated. The obtained dark green solid was subsequently filtered and washed with ether (yield 800 mg, 61 %). We then performed a recrystallisation to obtain the pure product. The crude product (120 mg) was dissolved in a mixture of methanol and water (2:1 ratio) and left under a N_2 flow for several days, which afforded dark-green stick crystals (yield 70 mg, 58 %).

$[[Fe(\boldsymbol{Rac}-cth)]_2(dhbq)](PF_6)_3$, 2-H

The crude product, [(Fe(Rac−cth))(μ−dhbq)(Fe(Rac−cth))]$(PF_6)_3$, was obtained in the same manner as for **1-H** using L = *Rac*-cth for the synthesis of the mononuclear precursor (yield 780 mg, 62 %). The yield of the dicationic precursor was 98 % (1095 mg). For the recrystallisation, the crude product (120 mg) was dissolved in a mixture of methanol and water (1:1 ratio) with a few drops of acetonitrile added. The solution was left to evaporate slowly under a nitrogen atmosphere over several days, resulting in the formation of dark-green plate crystals (yield 50 mg, 41 %).

$[[\mathbf{Fe}(\boldsymbol{SS}\mathbf{-cth})]_2\mathbf{(dcbq)}](\mathbf{PF_6})_3 \cdot \mathbf{H_2O} \cdot \mathbf{MeOH}$, 1-Cl

The crude product, $[(\mathrm{Fe}(SS\text{−cth}))(\mu\text{−dcbq})(\mathrm{Fe}(SS\text{−cth}))](\mathrm{PF}_6)_3$, was obtained in the same manner as for **1-H** using L = *SS*-cth for the synthesis of the mononuclear precursor and replacing H_2dhbq with H_2dcbq (yield 557 mg, 40 %). The yield of the dicationic precursor was 55 % (650 mg). The recrystallisation was carried out the same way as for **1-H** using 80 mg crude product, again yielding dark-green stick crystals (yield 30 mg, 37.5 %).

SQUID Magnetometry

We performed our magnetisation measurements with a Quantum Design MPMS3 SQUID magnetometer. Samples ($\approx$ 15 mg) were ground to a fine powder, mixed with liquid eicosane (T_{max} = 45 °C) and contained in gelatin capsules. Variable-field measurements, $M(H)$, were conducted at T = 2, 3, 5, and 10 K (ΔH = 70 mT/s), and variable-temperature measurements, $M(T)$, were conducted while applying a moderate field of H = 100 mT (ΔT = 2 K/min). We calculated the magnetic susceptibility, χ, of our samples using the linear approximation $\chi_{\mathrm{sample}}(T) = M(T)/H - \chi_{\mathrm{in}} - \chi_{\mathrm{env}}$, where χ_{env} is the contribution from the eicosane and gelatin, corrected for by subtracting a measurement of an empty sample holder, and χ_{in} is the sample's intrinsic diamagnetism estimated using Pascal's constants.[40]

Inelastic Neutron Scattering

We performed our INS experiments at two facilities: At Institut Laue-Langevin (ILL) in Grenoble, France, where we used the direct geometry time-of-flight (dg-TOF) spectrometer IN5 and the backscattering-and-time-of-flight spectrometer IN16b, and at the Spallation Neutron Source at Oak Ridge National Laboratory (ORNL) in Tennessee, USA, where we used the dg-TOF spectrometer SEQUOIA.[41–44] For all experiments, we used approximately 1 g of polycrystalline sample, which was contained in annular aluminium cylinders, and the relative efficiencies of the neutron detectors were always normalised using a standard

vanadium sample. Mantid was used to reduce, integrate and cut the INS data.[45,46]

At IN5, we used incident neutron energies, E_i's, of 1.94 and 3.47 meV, with chopper settings such that the energy resolution (FWHM) at zero energy transfer was 39 µeV and 90 µeV for $E_i = 1.94$ and 3.47 meV, respectively. An ILL orange cryostat cooled the sample to temperatures between $T = 1.5$ K and $T = 50$ K. We collected data for 1 hour for $E_i = 1.94$ and for 1.5 hours for $E_i = 3.47$ meV independently of the temperature. The ILL reactor ran at reduced power (27 MW), thus the neutron flux was reduced by approximately 50 % compared to normal.

For the SEQUOIA experiment, we used E_i's of 35 and 100 meV and a closed-cycle refrigerator cooled the samples to 5 K.

At IN16b, we used the instrument in BATS mode with Si_{111} backscattering analysers corresponding to E_f=2.08 meV and a Q-range of 0.2-1.8 Å^{-1}. We used the 14° slit in the pulse chopper at 315 Hz for increased flux at relaxed resolution of 5.6 μeV. To increase the dynamic range, we combined several acquisitions with the energy transfer range centred at −380, −150 and +150 ueV with a counting time of 3 hours per acquisition with the reactor running at 44 MW.[42,43]

Electron Paramagnetic Resonance

Our HF EPR experiments took place at the French Laboratory for High Magnetic Fields at Institut Néel in Grenoble, France. The samples were ground to a fine powder, pressed to pellets (to avoid torquing effects, thickness ≈ 3 mm), wrapped in Teflon tape and placed in helium exchange gas inside a superconducting solenoid (T = 8-18 K, B = 0-15.8 T).

For our measurements, we used a multi-frequency spectrometer, which was setup in a double-pass configuration and operated in transmission mode. Two frequency sources equipped with multipliers provided the radiation. These sources can operate either with a fixed value (110.4 GHz for one and 127.68 GHz for the other) or with a step-tunable value in a range of the fixed value ±10 GHz.

Our X-band EPR spectra were collected with a Bruker EMX+ spectrometer at the EPSRC National Service for Electron Paramagnetic Resonance Spectroscopy at the Photon Science Institute, University of Manchester, UK. We ground the polycrystalline samples (mg scale) into eicosane to fix them to avoid field-induced orientation. The spectrometer ran with the following settings: $\nu = 9.375$ GHz microwave radiation, power of 2.2 mW, attenuation of 20 dB, 0.2 mT modulation amplitude and 100 KHz modulation frequency. A closed-cycle refrigerator cooled the sample to temperatures down to 5 K.

Far-Infrared Magneto-spectroscopy

Our FIRMS experiment also took place at the French Laboratory for High Magnetic Fields at Institut Néel in Grenoble, France. A mercury lamp generated the non-polarised radiation for the experiment and a Bruker Vertex 80v Fourier-transform spectrometer analysed the radiation. Light-pipe optics delivered the light to the sample, which was placed inside a superconducting solenoid (0-16 T) submerged in liquid helium ($T = 4.2$ K). To ensure IR transmission through the samples, we ground them to fine powders, diluted them in eicosane and pressed them to pellets. After trying several configurations, we obtained the most intense signal by using a 1:20 sample-to-eicosane ratio and ≈ 2 mm thick pellets. The setup ran in a Faraday configuration ($k \parallel B$). A composite bolometer, placed below the sample, detected the transmitted light. Spectra were collected between 0 and 16 T in steps of 0.25 T.

We used Field-Optic to treat our data.[47] Field-dependent spectra of a pure eicosane pellet (tickness ≈ 0.5 mm) were used to correct for the eicosane contribution to the sample spectrum and for the field-dependence of the sensitivity of the bolometer. The magneto-transmission colourmap was obtained by normalising the derivative of raw spectra, measured at field strength B, to the average of derivatives of spectra measured at $B \pm 3.75$ T. To correct for a sloping baseline along the field direction of the spectrum, we fit a linear function to the average of the central part of the spectrum (14-24.5 meV) and subsequently subtracted that from all spectra.

Results and discussion

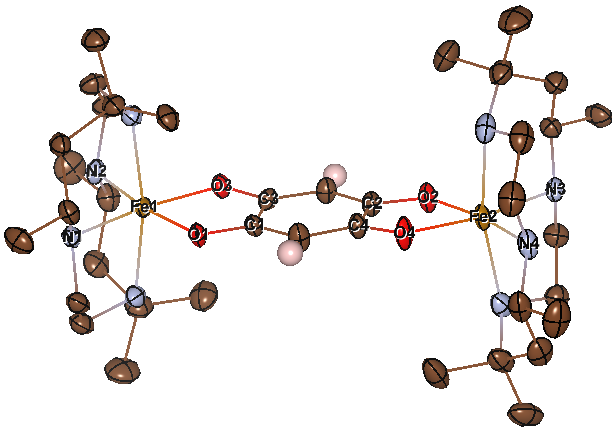

Fig. 1: ORTEP drawing of **1-H** with 75 % probability ellipsoids with H, C, O, N and Fe in beige, brown, red, blue and gold, respectively. Hydrogens not bound to the dhbq bridge are left out for clarity, and only the atoms discussed in the text are labelled. The structure is derived from single-crystal X-ray diffraction patterns measured at $T = 100$ K.

Figs. 1 and S1 show the structures of **1-H**, **2-H** and **1-Cl**, and Tab. 1 summarises the most important structural information (see Tab. S1 for complete crystallographic information). In all dimers, the irons are coordinated to two oxygens from the bridge and four nitrogens from the capping ligand, which leads to distorted octahedral environments. In the enantiopure versions, the coordination environment of the two irons are formally distinguishable, albeit similar, while the irons in the racemic analogue are related by inversion symmetry. The average N-Fe-N and O-Fe-O bond angles are always close to 100° and 80°, respectively, which suggests that the distorted symmetry is closer to C_{2v} rather than O_h.[48] The enantiopure versions crystallise in the $P2_1$ space group while **2-H** crystallises in $P2_1/c$; all compounds have two structurally identical molecules oriented differently within the unit cell.

The structures contain significant information about the oxidation state of the irons and the redox-active bridges with the most important indicators being the Fe-O, C-O and C-C (within the chelating ring) bond lengths. At $T = 100$ K, the average Fe-O bond lengths are 1.984(5) Å (**1-H**), 1.986(7) (**2-H**) and 1.979(5) Å (**1-Cl**), which are all short and consistent with an Fe^{3+} assignment in line with Ref. 14.[26,28] This implies that the dhbq/dcbq bridges

Tab. 1: Selected bond lengths and angles for $[Fe(RR{-}cth)]_2(dhbq)]^{3+}$ (**1-H**) and derivatives at $T = 100$ K. The numbering of atoms for **2-H** and **1-Cl** follow that of **1-H** in Fig. 1.

		1-H	**2-H**	**1-Cl**
Fe1-O1	[Å]	1.987(2)	1.978(4)	1.962(4)
Fe2-O2	[Å]	1.982(2)		1.989(4)
Fe1-O3	[Å]	1.979(2)	1.979(3)	2.005(3)
Fe2-O4	[Å]	1.987(3)		1.989(3)
C1-C3	[Å]	1.481(4)	1.479(7)	1.463(7)
C2-C4	[Å]	1.493(4)		1.473(7)
C1-O1	[Å]	1.293(4)	1.291(5)	1.294(6)
C2-O2	[Å]	1.293(4)		1.284(6)
C3-O3	[Å]	1.296(4)	1.292(6)	1.268(6)
C4-O4	[Å]	1.292(4)		1.298(6)
O1-Fe1-O3	[°]	79.99(8)	80.27(14)	79.50(13)
O2-Fe2-O4	[°]	79.53(8)		79.36(15)
N1-Fe1-N2	[°]	101.31(10)	97.92(14)	101.65(14)
N4-Fe2-N3	[°]	101.72(10)		100.83(14)

must be in the trianionic state since the dimer as a whole is tricationic. A trianionic bridge would be immediately visible in the structure. C-O bond lengths in trianionic dcbq are around 1.30 ± 0.01 Å, while typical values lie around 1.25 Å in the dianionic case. The trend is reversed for C-C bond lengths, which are around 1.45 ± 0.02 Å in $dcbq^{3-}$ but usually exceed 1.49 Å in $dcbq^{2-}$.[26,28] The average C-O and C-C bond lengths within the chelating ring in our dimers are 1.294(8) and 1.487(6) Å (**1-H**), 1.292(8) and 1.479(7) Å (**2-H**) and 1.286(12) and 1.468(10) Å (**1-Cl**), which unambiguously confirms the trianionic assignments.

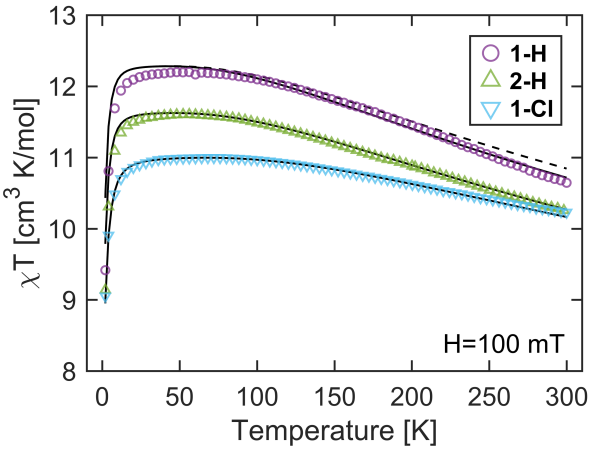

Fig. 2: Temperature dependence of molar magnetic susceptibility-temperature products for **1-H** (purple circles), **2-H** (green triangles) and **1-Cl** (blue triangles) alongside simulations based on eq. (1) with parameters from Tab. 2 (full lines). The simulations are scaled to correct for errors in the molecular weights as described in the text. The dashed line shows the model for **1-H** with $J = -225$ cm^{-1} which fits the susceptibility data equally well but is ruled out by X-band EPR data (see Fig. S8).

In TM compounds bridged by radical dhbq derivatives, spatial overlap of the frontier orbitals usually leads to direct exchange, which causes strong antiferromagnetic coupling and creates well-isolated spin ground states with $S = 2S_{TM} - 1/2$; for a $^{hs}Fe^{3+}$ dimer the ground state would be $S = 9/2$.[14,17,28,29] Our dimers follow the same trend according to their magnetic susceptibilities as shown in Fig. 2, in excellent agreement with the expectations from our structural analysis. Upon lowering the temperature, each χT curve slowly increases from its room-temperature value towards a plateau around $T = 50$ K. For **1-H**, $\chi T = 12.2$ cm^3 K/mol at $T = 50$ K, which is nearly equal to 12.375 cm^3 K/mol, the expected value for

an isolated $S = 9/2$ ground state with $g = 2$. In contrast, for **2-H** and **1-Cl**, χT=11.6 and 11.0 cm^3 K/mol at $T = 50$ K which would infer that $g_{\mathbf{2\text{-}H}} = 1.94$ and $g_{\mathbf{1\text{-}Cl}} = 1.89$ assuming $S = 9/2$. However, our HF EPR experiments (*vide infra*) clearly show that $g \geq 1.99$ for these compounds meaning that reduced g-values cannot be the origin of this discrepancy. Instead, we ascribe the reduction of χT at 50 K to imprecisions in the molecular weights used for data normalisation. Other spin ground states with large S can also be excluded since their χT values would be either significantly smaller ($\chi T = 7.785$ cm^3 K/mol for $S = 7/2$, $g = 2$) or larger ($\chi T = 15$ cm^3 K/mol for $S = 5$, $g = 2$) and low-temperature field-dependent magnetisation measurements are also consistent with $S = 9/2$ ground states (see Fig. S2). Thus, the χT data confirms that our dimers have well-isolated $S = 9/2$ ground states and that population of excited states with $S < 9/2$ drives the decrease in χT upon heating.

We attribute the steep decline at the lowest temperatures to significant zero-field splitting (ZFS) within the ground state manifolds caused by intrinsic magnetic anisotropies of the Fe^{3+} centres; an idea which is further supported by the absence of magnetic saturation in any of the dimers at $T = 2$ K and $H = 5$ T (see Fig. S2). This is somewhat unexpected, since Fe^{3+} and radicals are usually isotropic. It was recently suggested that partial ligand-to-metal charge transfer (LMCT) is the mechanism behind strong anisotropy in a Fe^{3+}−$dcbq^{3-}$ metal-organic framework, and the same mechanism is probably responsible for the anisotropy of our dimers.[25] From a naive point-of-view, this can be viewed as giving rise to some Fe^{2+} character at the metal centre, which is orbitally degenerate and therefore anisotropic. Several dhbq/dcbq-bridged compounds with Fe and Co centres show valence tautomeric transitions, which shows that such LMCT is possible.[21,23,24,26]

Based on the above discussion, it is necessary to use a Hamiltonian of the following form to model the magnetism of the dimers:

$$\mathcal{H} = -2J(\mathbf{S}_1 \cdot \mathbf{S}_2 + \mathbf{S}_2 \cdot \mathbf{S}_3) + \sum_{k,q} B_k^q \left(\mathcal{O}_k^q(\mathbf{S}_1) + \mathcal{O}_k^q(\mathbf{S}_3)\right) + \mu_B \left[\mathbf{B}^T \mathbf{g}(\mathbf{S}_1 + \mathbf{S}_3) + g\mathbf{B} \cdot \mathbf{S}_2\right] \quad (1)$$

where $S_1 = S_3 = 5/2$ refer to the Fe^{3+} centres, $S_2 = 1/2$ refers to the radical bridge and J parameterises the exchange coupling between them. We leave out a term describing Fe-Fe superexchange since we expect it to be insignificant compared to direct metal-radical exchange. Stevens operators, $\mathcal{O}_k^q$, describe the anisotropies of the Fe centres, which are parameterised by the B_k^q constants. These are assumed to be equal for both Fe sites to avoid overparameterisation. The last term describes the Zeeman interaction where $\mathbf{B}$ is the applied magnetic field (T denotes transpose), $\mathbf{g}$ is the Fe^{3+} g-tensor (assumed to be diagonal) and $g = 2$ is the radical g-value, which for simplicity is assumed to be isotropic. The magnetic susceptibility curves alone do not contain enough information to uniquely determine the parameters of this Hamiltonian, not even in the rather conservative case where only two Steven's operators, an exchange coupling and an isotropic $\mathbf{g}$-tensor sufficiently describes the magnetism. Thus, it is necessary to combine several experimental approaches to pin down each term of the Hamiltonian.

INS can probe the ZFS within the ground spin manifold directly in zero field since the energy change of the scattered neutrons is equal to the ZFS gaps. Fig. 3 contains the INS spectra of all dimers and we assign each peak to a transition between doublets within the $S = 9/2$ ground manifold based on their momentum transfer dependencies and the $\Delta m_S = \pm 1$ INS selection rule. We model the spectra with a combination of Gaussians accounting for each peak and a polynomial background which we fit to the data using a χ^2-method. Afterwards, we subtract the background and extract the excitation energies as the best-fit values of the means of the Gaussians. At $T = 50$ K we find excitations at 0.4076(6), 0.532(2), 0.6267(4) and 0.8752(3) meV for **1-H**, 0.4221(5), 0.5099(15), 0.6627(7) and 0.9197(8) meV for **2-H** and 0.364(6), 0.5890(15) and 0.8081(11) meV for **1-Cl**. For the dhbq-bridged analogues, the T-dependence of the spectra (see also Fig. S3) revealed that each peak corresponds to the transition from one doublet within the ground manifold to the next, which raises the question of whether a fourth peak is missing in the spectrum of **1-Cl** closer to $E = 0$. High-resolution INS experiments rules out this possibility (see Fig.

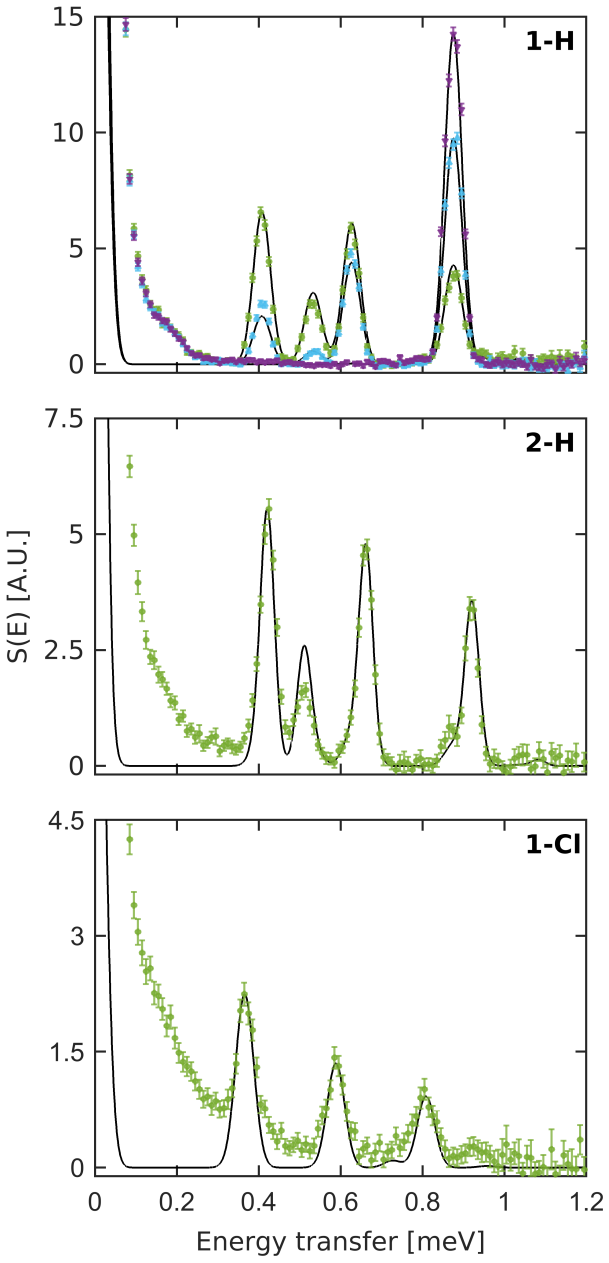

Fig. 3: INS spectra of **1-H** (top), **2-H** (middle) and **1-Cl** (bottom) measured with IN5@ILL at 50 K (green circles), 7.5 (blue triangles) and 1.5 K (purple triangles) using $E_i = 1.94$ meV and integrated over the momentum transfer range $Q = (1 \pm 0.5)$ Å^{-1} . The black lines show spectra calculated using *mint* with the Hamiltonian in eq. (1) and the parameters in Tab. 2.[49] Fig. S3 show the T-dependent spectra of **2-H** and **1-Cl**.

S4) and a closer inspection of the relative intensities of the peaks in Fig. 3 reveal that the peak at $E = 0.364(6)$ meV must contain spectral weight from more than one excitation. Consequently, the gaps from the second to the third and fourth excited doublets must be nearly equal. Based on this analysis we construct the level schemes in Fig. 4 and use them to fit the parameters of the Hamiltonian.

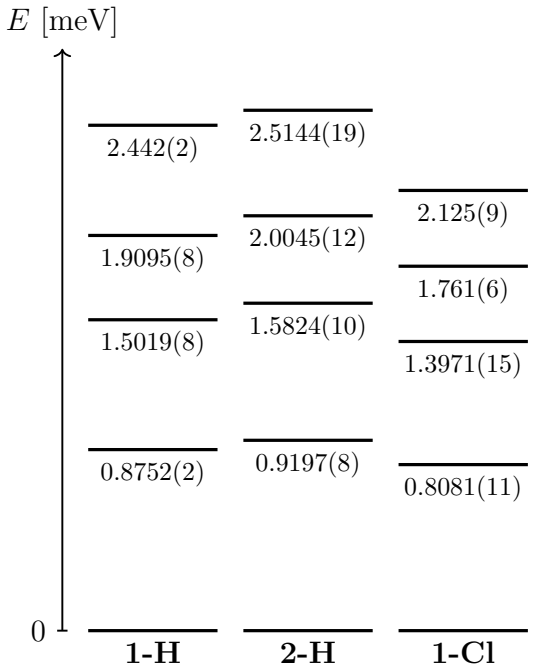

Fig. 4: Level splitting diagrams for the doublets within the $S = 9/2$ ground manifolds of all dimers based on the T-dependence of INS spectra in Figs. 3 and S3.

To avoid overparameterisation when modelling the INS data, the number of fitted parameters cannot exceed the number of experimentally determined eigenvalues. Based on the χT data, the $S = 9/2$ ground states are well isolated at $T \leq 50$ K due to strong antiferromagnetic exchange, which makes the ZFS parameters independent of the value of J. Therefore, we fix the exchange at $J = -225$ cm^{-1} for the dhbq analogues and at $J = -300$ cm^{-1} for **1-Cl** during our INS modelling. Models with two or three anisotropy parameters proved insufficient for accurately reproducing INS spectra, which further justifies keeping J fixed to allow for using more ZFS parameters for the fitting.

Normally, the coordination symmetry of the metal centres determines what Steven's

operators are allowed, but the Fe centres have no formal symmetry and therefore put no constraints on the choice of operators. However, since the effective symmetry is close to C_{2v} as previously mentioned, we use the simplest operators that are allowed for this symmetry, which leaves the following parameters to be fit: B_2^0 and B_2^2, which respectively describe easy-axis and rhombic anisotropies, as well as B_4^0 and B_4^4 which parameterise fourth-order corrections.[50] We leave out B_4^4 for **1-Cl** since only three gaps were determined experimentally and three parameters were sufficient to accurately model the data.

We use Easyspin to construct the Hamiltonians, a χ^2-method to fit the parameters and *mint* to simulate the INS spectra of models that best fit the eigenvalues.[49,51] Tab. 2 shows the parameters we obtain and the black lines in Fig. 3 show the simulated INS spectra, which are near-perfect matches to data. The parameters for **1-H** and **2-H** are rather similar, which shows that the symmetry differences between **1-H** and **2-H** have little influence on their anisotropies. This was counter-intuitive at first since symmetry is often the predominant factor that governs magnetic anisotropy. Ultimately, this agrees well with the idea that LMCT is the origin of the anisotropy, since centrosymmetry should not greatly influence LMCT. Conversely, this lead us to expect that altering metal-radical covalency by substituting an electron-withdrawing Cl group onto the bridging radical would have a larger influence on the anisotropy. Previously, such a substitution stabilised the radical in a $Co^{3+}-dcbq^{3-}-Co^{3+}$ dimer compared to its dhbq analogue and made its valence tautomeric transition inaccessible, which shows that Cl substitution can significantly perturb the nature of the radical.[17,21] The numbers in Tab. 2 clearly show that the substitution perturbs the magnetic anisotropy of our dimer, potentially caused by hindering of LMCT by the electron-withdrawing Cl group.

The simulations of the spectra of **1-H** and **1-Cl** use Gaussian line broadenings of 50 µeV (FWHM), i.e. slightly larger than the instrumental resolution, which suggests that our samples contain molecules with a distribution of anisotropies. This distribution is probably a consequence of the co-crystallised solvent in these samples which creates slightly different

Tab. 2: Parameters from the best fits of the Hamiltonian in eq. (1) to INS, HF-EPR, FIRMS, and SQUID data for **1-H**, **1-Cl** and **2-H**.

		1-H	**2-H**	**1-Cl**
g_x	N/A	1.980(10)	2	~ 2.15
g_y	N/A	2	2	2
g_z	N/A	2	2	2
B_2^0	cm^{-1}	-0.56906(12)	-0.5940(2)	-0.5158(4)
B_2^2	cm^{-1}	-0.3075(9)	-0.2867(14)	-0.186(5)
B_4^0	10^{-4} cm^{-1}	-2.56(10)	-3.3(2)	-3.4(4)
B_4^4	10^{-4} cm^{-1}	47(5)	37(9)	0
J	cm^{-1}	-210(10)	-225(2)	-300(10)

surroundings for individual molecules. In contrast, Gaussians with FWHM equal to the instrumental resolution (40 µeV) accurately reproduce the experimental line widths of **2-H**, which contains no solvent. However, to capture the asymmetry of the peaks at 0.6627(7) and 0.9197(8) meV in the spectrum of **2-H**, it is necessary to add a minor **1-H** species (15 %) to the simulated spectrum.

Fig. 5 shows the momentum transfer (Q) dependence of the intensity of the highest-energy excitation in **2-H** ($E = 0.9197(8)$ meV). Modulations of the INS intensity as a function of Q depends on the relative positions of the magnetic centres and their magnetic form factors (MFFs).[52] MFFs decay as a function of Q and are defined as the spatial Fourier transform of the normalised unpaired electron density of a spin centre, which is delocalised over a large area for an aromatic, organic radical like $dhbq^{3-}$ and derivatives. Therefore, the MFFs of such radicals are expected to decay more quickly with increasing Q compared to those of metal centres. Nonetheless, little attention is usually paid to the MFF of radicals and they are not tabulated unlike their metal counterparts.[53,54] In our case, a simulation which neglects the MFF of the bridging radical does not reproduce the experimentally observed intensity modulation (Fig. 5, dashed line). The MFF of $dhbq^{3-}$ is not known in the literature

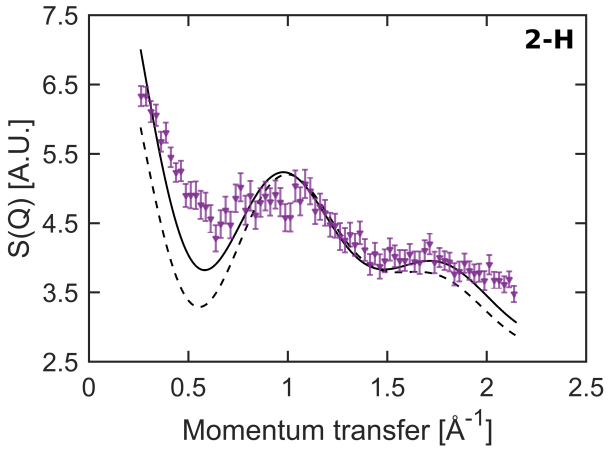

Fig. 5: Momentum transfer of the excitation at $E = 0.9197(8)$ meV $= 7.418(6)$ cm^{-1} in **2-H** measured at $T = 1.5$ K using $E_i = 3.47$ meV and integrated over the energy transfer range $E = (0.925 \pm 1)$ meV. The full and dashed lines show *mint* calculations with and without the magnetic form factor of a bridging radical, respectively.[49]

and measuring it is outside the scope of this work. Instead, we included the known MFF of radical pyrazine, a similar aromatic organic radical, in our simulation.[55] This significantly improved the quality of our simulation and further confirmed the radical character of the dhbq bridge.

HF EPR is an accurate technique for probing Zeeman terms in the Hamiltonian of molecules, which made it a natural next step in our investigation. EPR furthermore probes the ZFS within the ground manifold of molecules and can thereby compliment our INS data. The black lines in Fig. 6 show EPR spectra of **1-H**, **2-H** and **1-Cl** recorded up to $B = 15.8$ T at $T = 18$, 18 and 8 K using $\nu = 331.2$, 319.5 and 220.8 GHz, respectively, and Figs. S5-S7 show spectra measured with additional frequencies at more temperatures. The spectra are normalised such that the leftmost major transitions have equal peak intensities.

Based on the modelling of the INS data, we expected the spectra of the dhbq analogues to be similar and that is indeed the case. They both show three nearly equidistant resonances at $B \leq 8$ T, which correspond to consecutive axial ($\mathbf{B} \parallel g_{zz}$) transitions between the lowest-lying four doublets within the ground manifold according to their T-dependencies. The rich behaviour around $B = 11.83$ T and $B = 11.42$ T, which correspond to $g = 2$ for $\nu = 331.2$

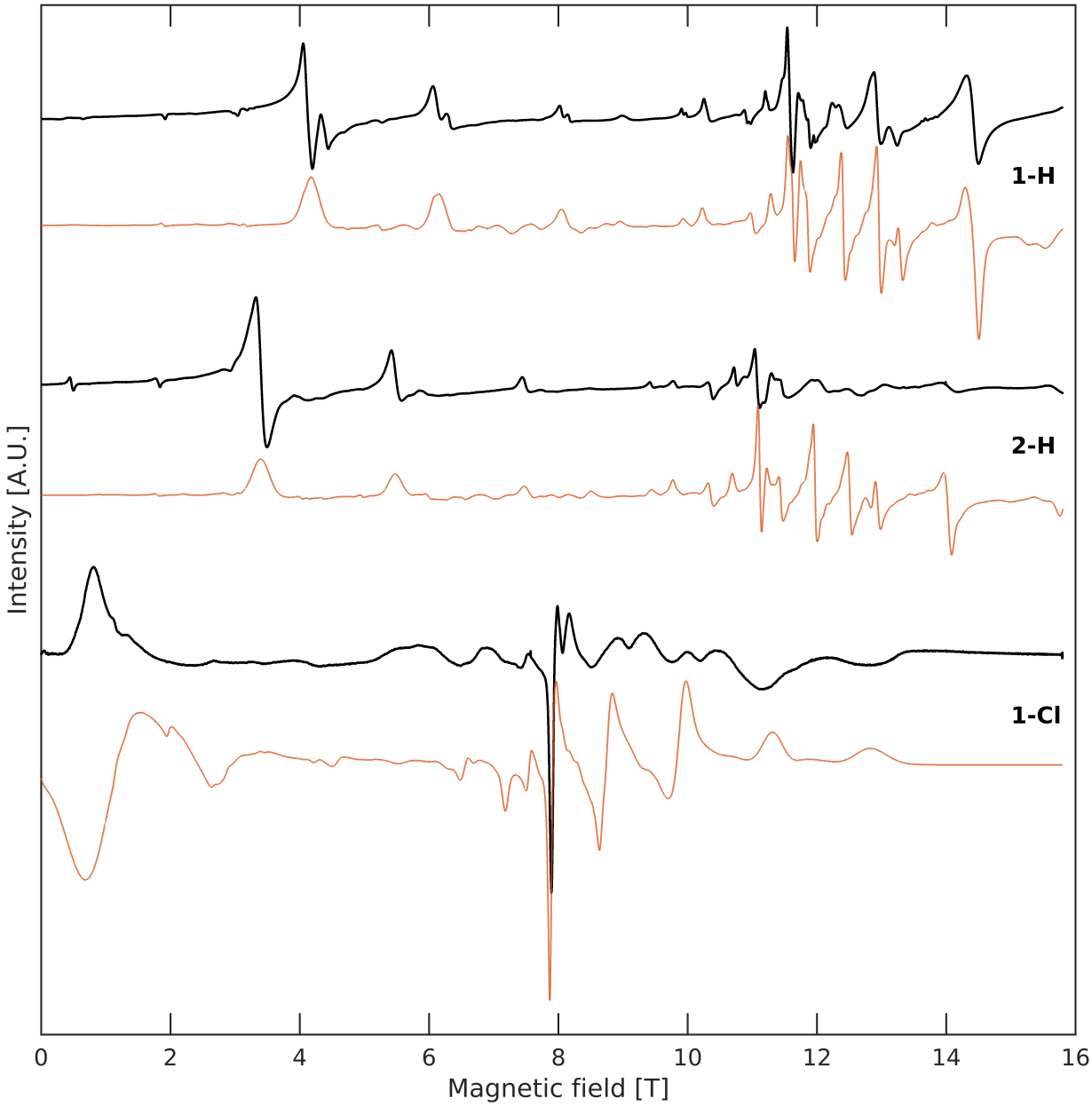

Fig. 6: HF EPR spectra (black) with Easyspin simulations (red) calculated using the Hamiltonian in eq. (1) and the parameters in Tab. 2 with a Lorentzian lineshape (FWHM = 36 mT).[51] **1-H**: $T = 18$ K, $\nu = 331.2$ GHz and 5 % B_2^0-strain; **2-H**: $T = 18$ K, $\nu = 319.5$ GHz and 5 % B_2^0-strain; **1Cl**: $T = 8$ K, $\nu = 220.8$ GHz and 15 % B_2^0-strain. Figs. S5, S6 and S7 show additional temperatures and frequencies.

and 319.5 GHz, respectively, originates from the in-plane ($B \perp g_{zz}$) transitions. The less intense peaks at $B < 4$ T are forbidden transitions ($\Delta m_S > 1$) which gain intensity due to state mixing caused by the non-zero fourth order Steven's operators. The axial transitions are slightly wider than the in-plane ones, which is usually caused by a distribution of axial B_k^q parameters. The spectrum of **1-Cl** is resolved worse compared to the two others. As a consequence, the axial transition close to $B \approx 1$ T is only clearly distinguishable from the background in the spectra measured at $T = 8$ K where the spectral weight is distributed across fewer peaks due to limited thermal population of excited states. In contrast, the in-plane transitions around $B \approx 7.89$ T, which is equivalent to $g = 2$ for $\nu = 220.8$ GHz, are resolved better, and for this reason we ascribe the worse resolution to a larger strain on the axial B_k^q parameters. Partial solvent loss or absorption of moisture from the atmosphere are possible origins of the increased strain.

We model the EPR spectra based on the Hamiltonian in eq. 1 with the **g**-tensor as the only free parameter since the INS experiments already provided the anisotropy parameters and we still operate well within the strongly coupled regime ($T \ll 50$ K) where the spectra are independent of J. We accounted for the observed anisotropy strains by including strains on the B_2^0-parameters (5 % for **1-H** and **2-H**, 15 % for **1-Cl**). Due to the nature of the our HF EPR setup, which works without an optical cavity in contrast to commercial EPR spectrometers, it is not possible to asses any quantitative agreement between simulated and experimental spectra. It is, for example, commonly known that transitions at low magnetic fields can be less intense in simulated spectra compared to experiments. Also, the phase of the microwave radiation is not controlled explicitly and can therefore change because of the applied magnetic field, which can flip the sign of the measured spectrum during a sweep.

The red lines in Fig. 6 show the best simulations with **g** as the only free parameter. They are an excellent match to the measured spectra and thereby cements the Steven's parameters obtained from the INS data (Tab. 2 contains the optimal **g**-values). For **2-H**, the centrosymmetric dimer, we find no evidence for **g**-tensor anisotropy while $g_{xx} \neq 2$

for both enantiopure dimers. The g-anisotropy is small for **1-H**, however it was strictly necessary for aligning the principal in-plane transition to the experimentally observed value at all frequencies. For **1-Cl**, the g-anisotropy appears to be rather large, however the quality of the spectrum makes it difficult to quantitatively asses. Still, given the major displacement of the main in-plane peak from the isotropic case it is likely that $g_{xx} > 2$. The complete nature of the underlying mechanism is not clear, however it well known that lower structural symmetry causes lower electronic symmetry.

With the Zeeman and anisotropy terms of the Hamiltonian pinned down by HF EPR and INS, respectively, we turn our focus to the exchange term. Based on the slopes of χT data we expect the excited spin multiplets to lie 20-40 meV above the ground state and that the coupling within **1-Cl** is stronger than in the dhbq analogues. This agrees with temperature-dependent X-band EPR spectra (see Fig. S8) in which a narrow line emerges around $B = 335$ mT (equivalent to $g = 2$) between 100 and 200 K for both dhbq analogues. We assign this line as originating from the radical bridge when the thermal energy is large enough to compete with the exchange coupling. The feature emerges at lower temperatures for **1-H** than for **2-H**, which suggests that $|J_{\mathbf{1\text{-}H}}| < |J_{\mathbf{2\text{-}H}}|$.

INS is one of the only spectroscopic techniques that can directly probe inter-multiplet transitions, and therefore exchange constants, due to its unique selection rule $\Delta S = \pm 1$. Unfortunately, the ability of INS to probe magnetic transitions in the expected energy range is inherently limited. Low-Q regions become inaccessible when the energies of the incident neutrons increase, thus signals become weak due to the intrinsic decay associated with the MFFs. The phonon partial density-of-states (pDOS) of molecules containing organic ligands furthermore often overlap with the expected magnetic transitions, which can cause vibrational scattering to dominate magnetic signals in INS spectra due to the large incoherent neutron cross section of hydrogen.[54] The spectra in Fig. S9 shows that this is indeed the case for our dimers. They only contain intense vibrational transitions recognised by the characteristic momentum transfer dependence ($I \propto Q^2$).

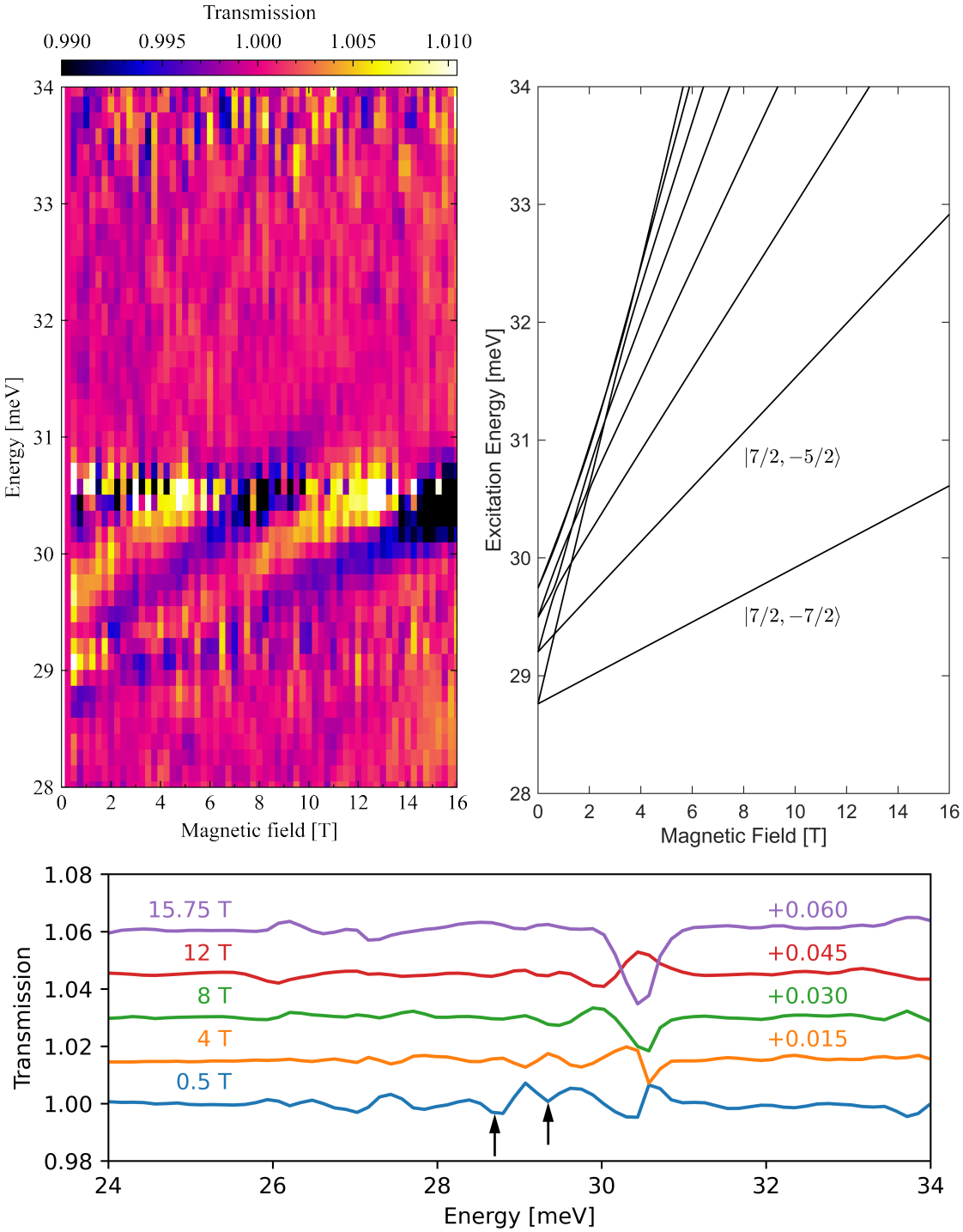

Fig. 7: **Left:** FIRMS spectrum of **2-H** at $T = 4.2$ K. **Right:** Field-dependence of excitation energies from the ground state ($|9/2, -9/2\rangle$) to states within the first excited $S = 7/2$ manifold calculated with eq. (1) using the parameters in Tab. 2. **Bottom:** Magneto-transmission of **2-H** for selected magnetic fields. Each line is the average of three scans separated by 0.25 T. The arrows mark the magnetic absorption features.

Instead, we used FIRMS to probe the exchange coupling within our dimers. Inter-multiplet transitions are formally forbidden (only $\Delta m_S = \pm 1, 0$ is allowed), but magnetic features can emerge if vibronic coupling is significant, or if the wave functions of the involved states contain components with different S. Fig. 7 (Left and Bottom) shows the FIRMS spectrum of **2-H** collected at $T = 4.2$ K, which contains a feature emerging from $E = 28.7(2)$ meV with $g = 2$. A second feature with $g \approx 4$ is present at slightly higher energy, however its weak intensity and the overlap with the strong artefact at 30.5 meV makes it difficult to extract a precise excitation energy by extrapolating to $B = 0$. Both features cease to exist upon crossing the artefact at $E = 30.5$ meV, which is caused by poor normalisation of a particularly strong vibrational absorption. While quantitative simulation of spin-phonon coupling is outside the scope of this work, one can speculate whether the envelope effect for vibronic FIRMS transitions, described by Kragskow et al, plays a role.[35]

Based on the slopes of the field-dependent features, we assign them as the transitions from $|9/2, -9/2\rangle$ to $|7/2, -7/2\rangle$ and $|7/2, -5/2\rangle$ within the first excited spin manifold, where $|S, m_S\rangle$ refers to states with total spin S and projection m_S. Insertion of $J = -225(2)$ cm^{-1} into eq. (1) with all other parameters fixed at the previously determined values yields $E_{|7/2,-7/2\rangle} - E_{|9/2,-9/2\rangle} = 28.75$ meV in perfect agreement with the FIRMS observation. Fig. 7 (Right) shows the calculated excitations energies from $|9/2, -9/2\rangle$ to all states within the $S = 7/2$ manifold, which supports assigning the second feature as $|9/2, -9/2\rangle \rightarrow |7/2, -5/2\rangle$.

A calculation of χT using $J = -225$ cm^{-1} and the rest of the values in Tab. 2 excellently matches data (black line on green triangles in Fig. 2), which confirms that we are indeed probing excitations to the excited spin manifold. To our knowledge, this is the first direct observation of a molecular spin excitation with FIRMS and the first quantification of an Fe^{3+}-$dhbq^{3-}$ exchange coupling. This J-value is two orders of magnitude larger than previously reported antiferromagnetic couplings of Fe centres via innocent $dhbq^{2-}$ bridges; instead it resembles those reported oxo-bridged Fe^{3+} dimers.[56] This underlines the difference between bride-mediated Fe-Fe superexchange and direct Fe-radical exchange.[57,58]

Despite trying several pellet thicknesses and sample-to-eicosane ratios, we were not able to detect a FIRMS signal for any of the enantiopure dimers. This is probably due a change in vibronic coupling that occurs alongside the loss of molecular centrosymmetry as suggested by INS data. Fig. S9 clearly shows that the pDOS of **1-H** is different from that of **2-H**. Therefore, we have to rely on χT to estimate the exchange couplings within **1-H** and **1-Cl** while keeping the rest of the parameters fixed. The former has a slope similar to **2-H** in the range 50 K - 300 K, thus we expect their couplings to be similar. Both $J = -225$ cm^{-1} and $J = -210$ cm^{-1} provide good agreements with data (dashed and full lines on purple circles in Fig. 2, respectively), and based on the expectations from X-band EPR data we take $J = -210(10)$ cm^{-1} as the best estimate.

For **1-Cl**, $J = -300(10)$ cm^{-1} provided the best match of the data (black line on blue triangles in Fig. 2). This is $33 - 43\,\%$ larger than the dhbq analogues, which shows that functionalisation of the dhbq^{3-} bridge can affect the magnetic properties of Fe dimers in contrast to reports from Ref. 59. To our knowledge, this is the first report of a Fe^{3+}-dcbq^{3-} coupling. In comparison, Fe^{3+}-dcbq^{2-} couplings are ferromagnetic and two order of magnitude weaker.[17,22] Like for the dhbq analogues, this dramatic increase in coupling strength probably happens because the exchange mechanism becomes direct upon reduction.

The change of sign of J upon dcbq reduction stands out compared to the TPA-capped Fe^{2+} analogues in which $J > 0$ regardless of the oxidation state of dcbq. Another difference is that reduction of dcbq^{2-} only enhances the coupling by one order of magnitude instead of two in that series.[17,18] At first glance, it is tempting to conclude that these differences are related to the change in Fe oxidation state since the coordination environments provided by TPA and cth are quite similar. However, adding three methyl groups to TPA changes the Fe^{2+}-dcbq^{3-} couplings from $J_{\mathrm{TPA}} = 19$ cm^{-1} to $J_{\mathrm{Me_3TPA}} = -60$ cm^{-1} without dramatic changes to the first coordination sphere of the Fe ions.[59] This shows that ligand modifications far way from the metal centres can have significant impact and that couplings in Fe^{2+}-based dcbq-bridged molecules can follow the same trend upon bridge reduction as their Fe^{3+} counterparts. Thus,

the reason for the striking difference between $J = -300$ cm^{-1} and $J = 19$ cm^{-1} mediated by dcbq^{3-} in **1-Cl** and [Fe^{2+}(TPA)]$_2$(dcbq), respectively, remains unresolved, and the lack of a crystal structure for [Fe^{2+}(TPA)]$_2$(dcbq) prevents further preclusion. Oxygen K-edge spectroscopy could in theory shed light on differences in Fe-O orbital overlaps responsible for the different Fe-dcbq couplings. Unfortunately, **1-H** and **2-H** decompose instantly when exposed to a soft X-ray beam, which makes this avenue impossible.

Conclusion and Outlook

We have shown how a comprehensive experimental approach encompassing INS, HF EPR, FIRMS, and SQUID magnetometry can unravel the governing magnetic Hamiltonian of strongly coupled radical-bridged transition metal dimers, including exchange interactions and fourth order Steven's parameters. We used the approach to elucidate structure-property relationships in a series of newly synthesised Fe^{3+} dimers bridged by dhbq^{3-} and dcbq^{3-} radicals, however our methodology is generally applicable and future studies of strongly coupled molecular materials could benefit from adopting similar strategies. In particular, our direct observation of a molecular spin excitation with FIRMS hold promise for future investigations.

Our modelling showed that substitution of electron-withdrawing Cl groups onto the bridging ligand in **1-H** enhances antiferromagnetic Fe-radical coupling. Thus, functionalisation of radical dhbq derivatives can provide an avenue for tuning magnetic properties in contrast to previous findings.[59] INS data revealed significant ZFSs for the typically isotropic Fe^{3+} ions in all three dimers, presumably caused by LMCT as previously suggested.[25] Compared to **2-H**, the ZFS of **1-H** was left largely unaffected when the molecular centrosymmetry was broken by the capping ligand chirality. In contrast, our HF EPR data showed that the g-tensor becomes anisotropic when centrosymmetry is broken, however the underlying mechanism remains unknown.

The differences between the vibrational pDOS of **1-H** and **2-H** alongside the absence of any FIRMS intensity for **1-H** suggests that vibronic coupling is different in the two molecules, and consequently, that vibronic coupling can be controlled via the relative chirality of the capping ligands. Since control of vibronic coupling is essential for engineering single-molecule magnets (SMMs), our work shows that control of relative ligand chiralities could provide an avenue for tuning SMM properties.

Acknowledgement

The authors thank ILL and ORNL for INS beam time, the European Magnetic Field Laboratory for HF EPR and FIRMS magnet time, the EPSRC National Service for Electron Paramagnetic Resonance Spectroscopy for X-band EPR time and Adam Brookfield for assistance with X-band EPR measurements. The research at ORNL's Spallation Neutron Source was sponsored by the U.S. Department of Energy, Office of Basic Energy Sciences. RTC thanks ILL for funding a PhD student fellowship.

Contributions

RTC and MLB conceived and led the project. WZ synthesised the samples, performed single-crystal XRD measurements and solved the structure supervised by SQW and OS. RTC, AIK, MA and JO conducted the INS experiments and RTC analysed the data supervised by JO. RTC and ALB conducted the HF EPR experiments and analysed the data. RTC conducted the X-band EPR experiments and analysed the data. RTC and FLM conducted the FIRMS experiments and analysed the data supervised by MO. WZ and SQW performed the SQUID magnetometry measurements and RTC analysed the data supervised by RC and MLB. RTC wrote the manuscript with input from MLB and JO.

Supporting Information Available

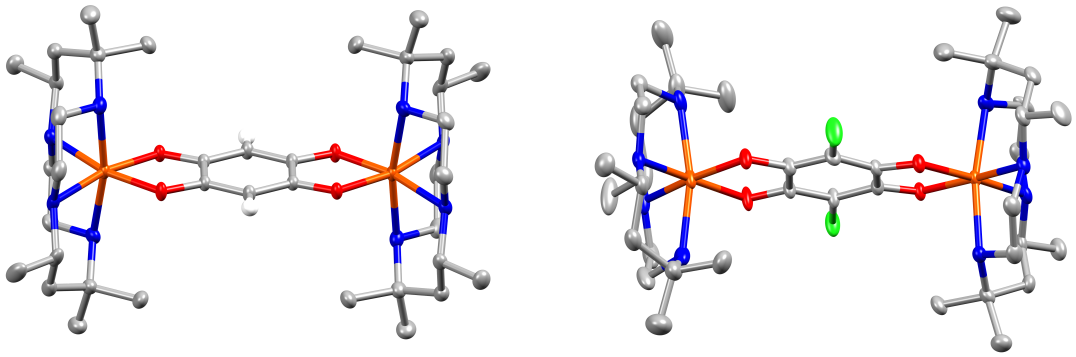

Fig. S1: ORTEP drawings of **2-H** (left) and **1-Cl** (right) with 50 % probability ellipsoids and Fe, O, N, C, H and Cl in orange, red, blue, grey, white and green, respectively. H's not bound to bridge are left out for clarity.

Tab. S1: Complete structural information for **1-H**, **2-H** and **1-Cl** obtained from single-crystal X-ray diffraction data obtained at $T = 100$ K. The structures are submitted to the Cambridge Crystallographic Data Base under number XX, YY, ZZ.

		1-H	**2-H**	**1-Cl**
Formula	N/A	$C_{39}H_{80}F_{18}Fe_2N_8O_6P_3$	$C_{38}H_{74}F_{18}Fe_2N_8O_4P_3$	$C_{39}Cl_2H_{78}F_{18}Fe_2N_8O_6P_3$
Weight	g/mol	1303.7	1253.6	1372.6
Z	N/A	2	2	2
Space Group	N/A	$P2_1$	$P2_1/c$	$P2_1$
a	[Å]	9.33011(15)	8.9086(4)	9.4816(3)
b	[Å]	18.8759(3)	30.8224(9)	18.7282(6)
c	[Å]	16.1790(3)	10.2987(5)	16.5658(5)
β	[°]	89.9946(14)	110.692(5)	93.989(3)
V	[Å^3]	2849.36(8)	2645.4(2)	2934.52(16)
μ	N/A	0.701	0.749	0.774
F_{000}	N/A	1348	1300.992	1420
Rad.	N/A	Mo Kα ($\lambda = 0.71073$ Å)		
Index ranges	N/A	$-12 \leq h \leq 12$ $-26 \leq k \leq 24$ $-23 \leq l \leq 23$	$-12 \leq h \leq 12$ $-42 \leq k \leq 43$ $-14 \leq l \leq 13$	$-13 \leq h \leq 11$ $-17 \leq k \leq 25$ $-22 \leq l \leq 22$
GoF	N/A	1.029	1.0299	1.048

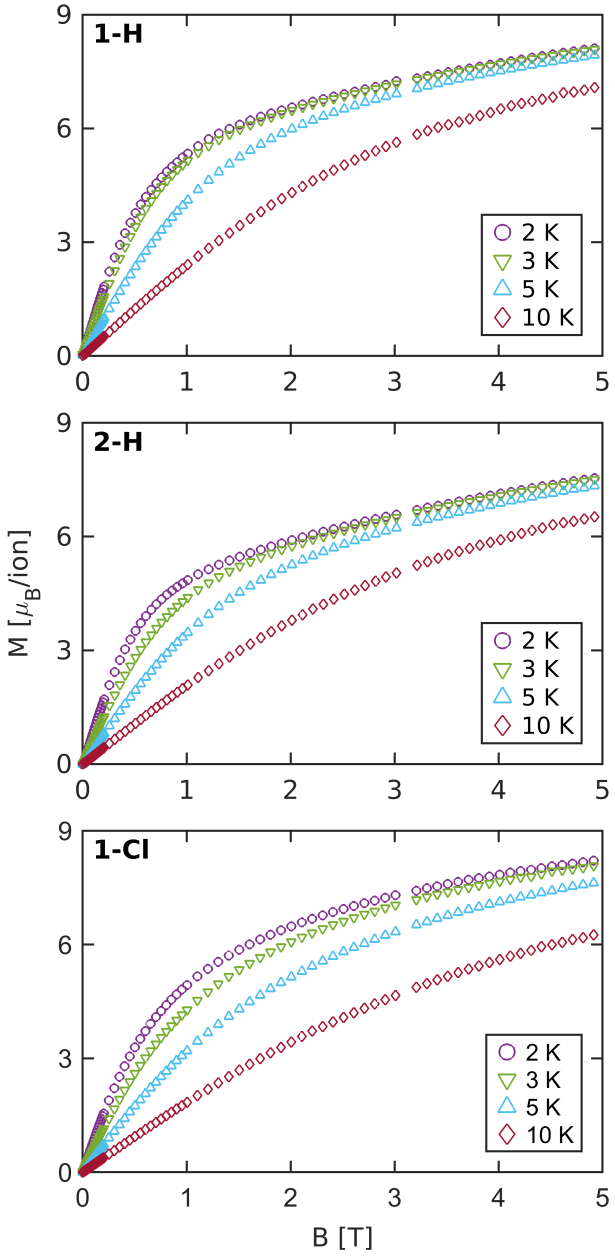

Fig. S2: Field-dependent magnetisation of **1-H** (top), **2-H** (mid) and **1-Cl** (bottom) measured at $T = 2$, 3, 5 and 10 K.

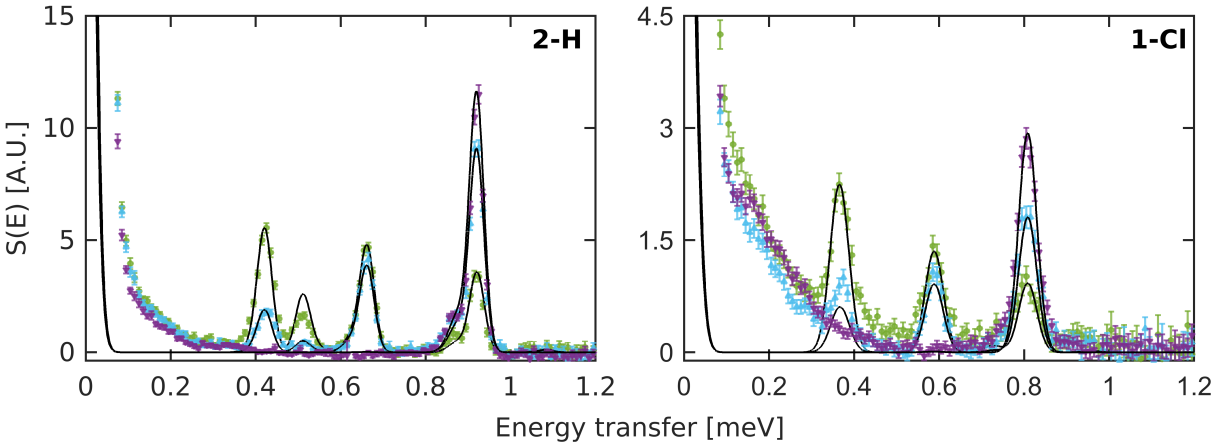

Fig. S3: Temperature dependence of INS spectra of **2-H** (left) and **1-Cl** (right) measured at 50 K (green circles), 7.5 (blue triangles) and 1.5 K (purple triangles) using $E_i = 1.94$ meV and integrated over the momentum transfer range $Q = (1 \pm 0.5)$ Å^{-1} . The black line shows *mint* simulations with the parameters from Tab. 2.[49]

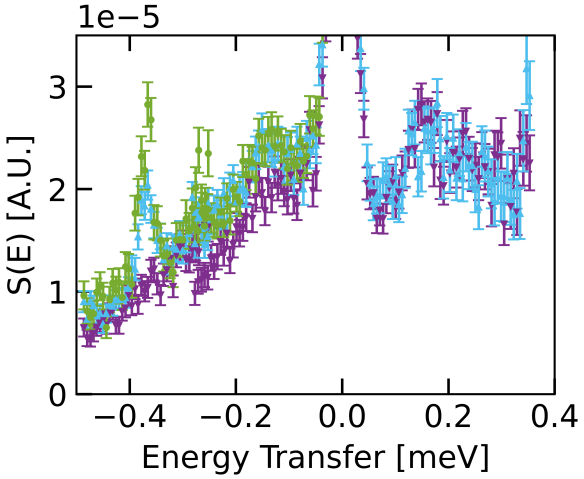

Fig. S4: High-resolution INS spectrum of **1-Cl** measured with IN16b@ILL at T = 1.6, 10 and 15 K in purple, blue and green, respectively. The magnetic excitation at $\hbar\omega = -0.364$ meV changes with temperature, which confirms its magnetic origin, while the non-magnetic feature at $\approx \pm 0.15$ meV is temperature independent.

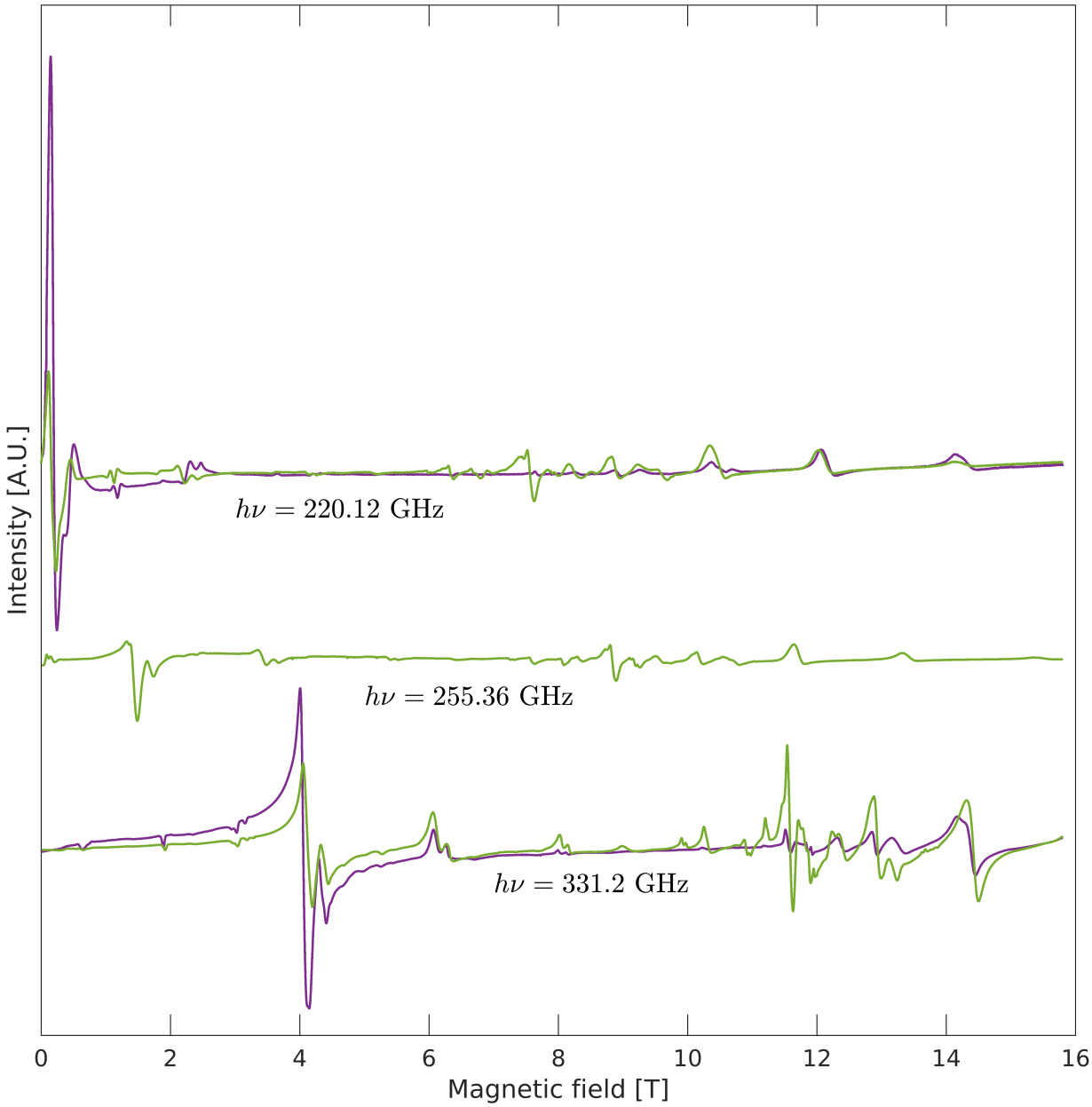

Fig. S5: Temperature dependence of HF EPR spectra of **1-H** measured at $T = 8$ K (purple) and 18 K (green) using $\nu = 220.8$, 255.36 and 331.2 GHz. The spectra are not normalised.

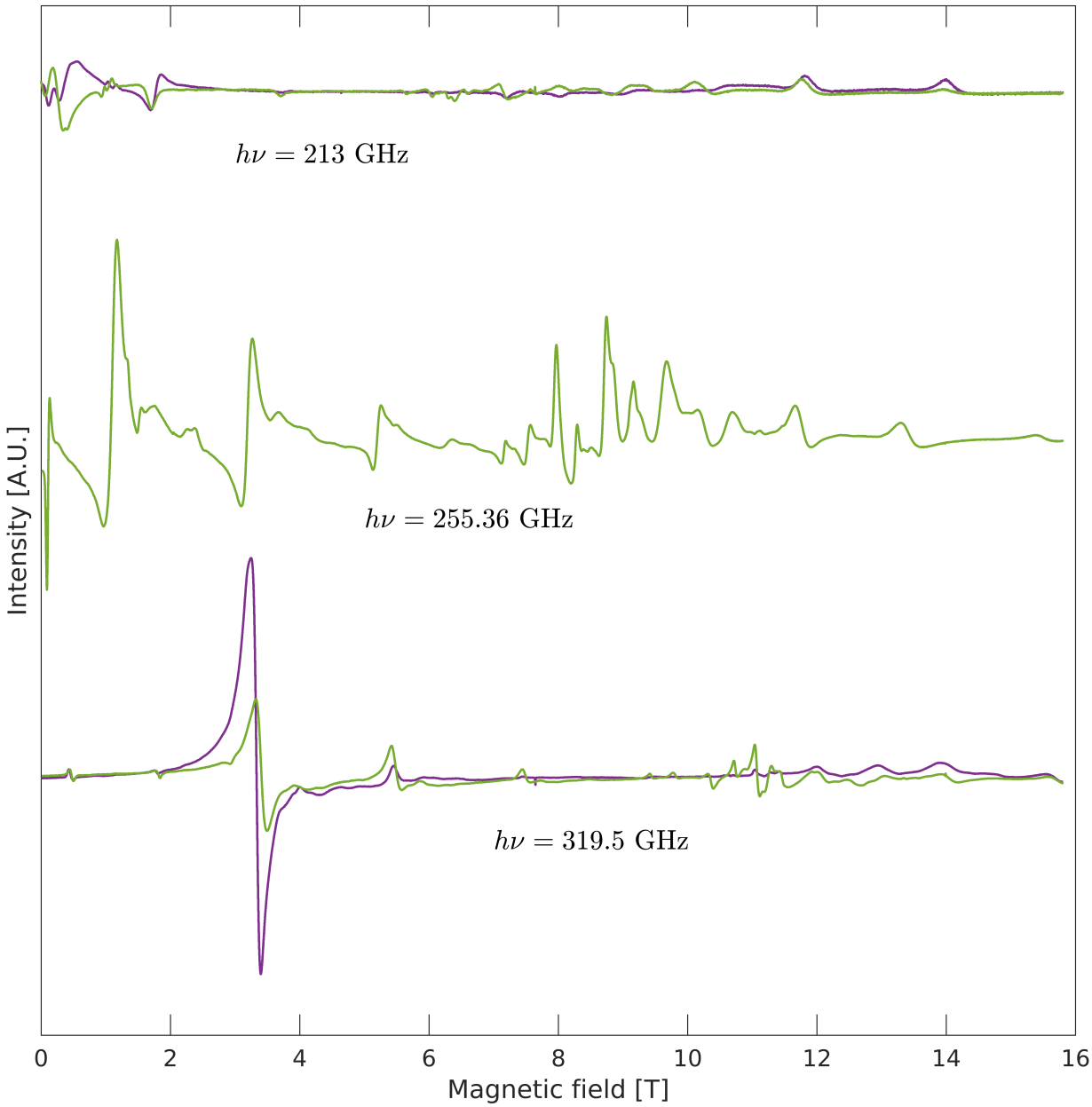

Fig. S6: Temperature dependence of HF EPR spectra of **2-H** measured at $T = 8$ K (purple) and 18 K (green) using $\nu = 213$, 255.36 and 319.5 GHz. The spectra are not normalised.

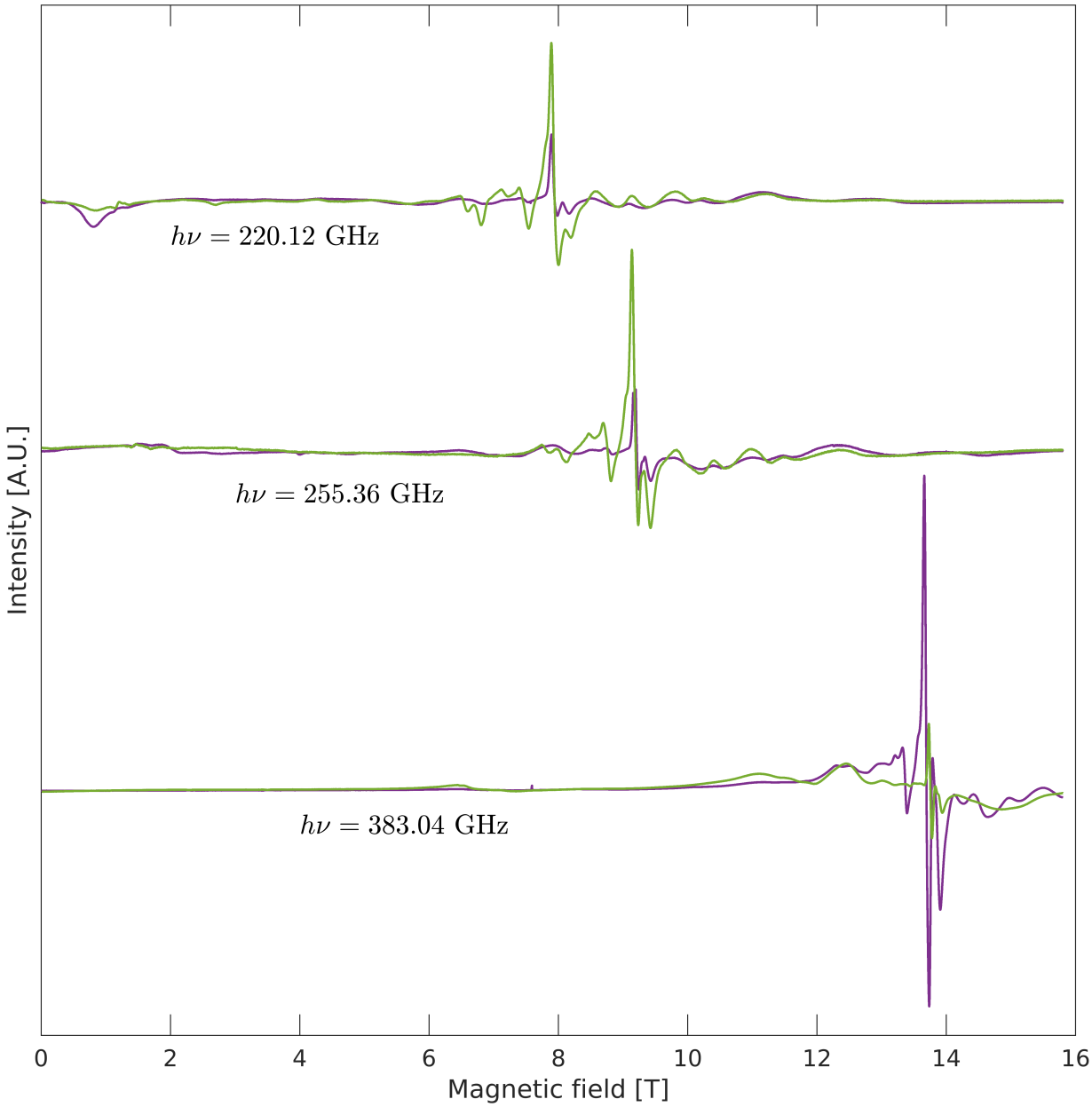

Fig. S7: Temperature dependence of HF EPR spectra of **1-Cl** measured at $T = 8$ K (purple) and 18 K (green) using $\nu = 220.8$, 255.36 and 383.04 GHz. The spectra are not normalised.

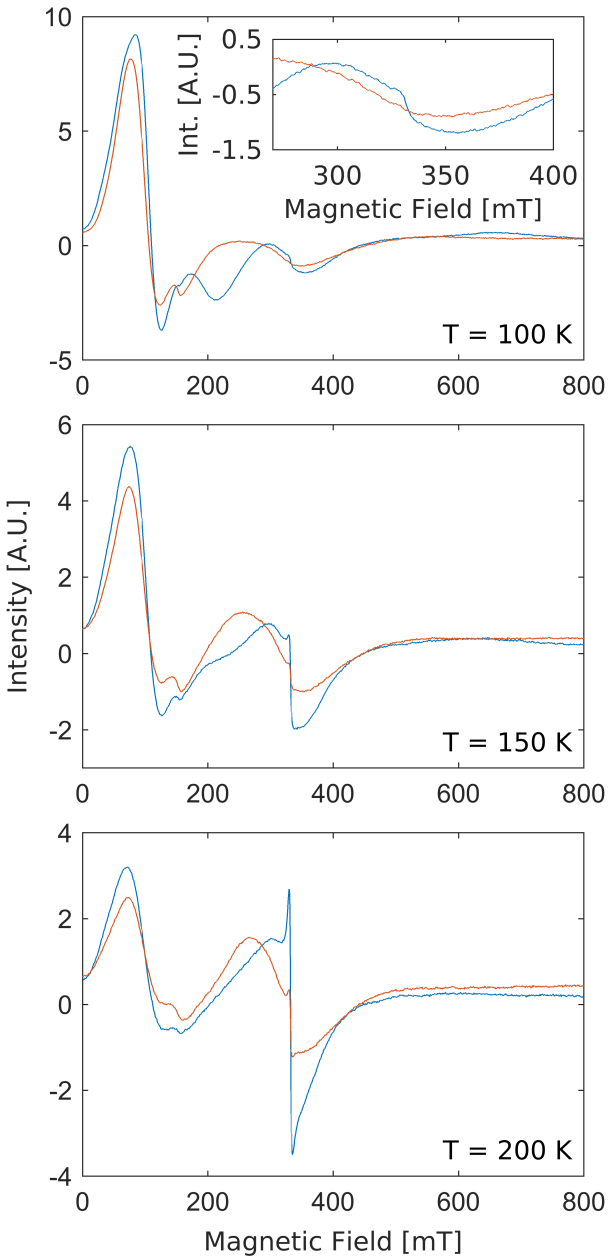

Fig. S8: Temperature-dependent X-band EPR spectra of **1-H** (top), **2-H** (mid) and **1-Cl** (bottom) measured at $T = 100$, 150 and 200 K.

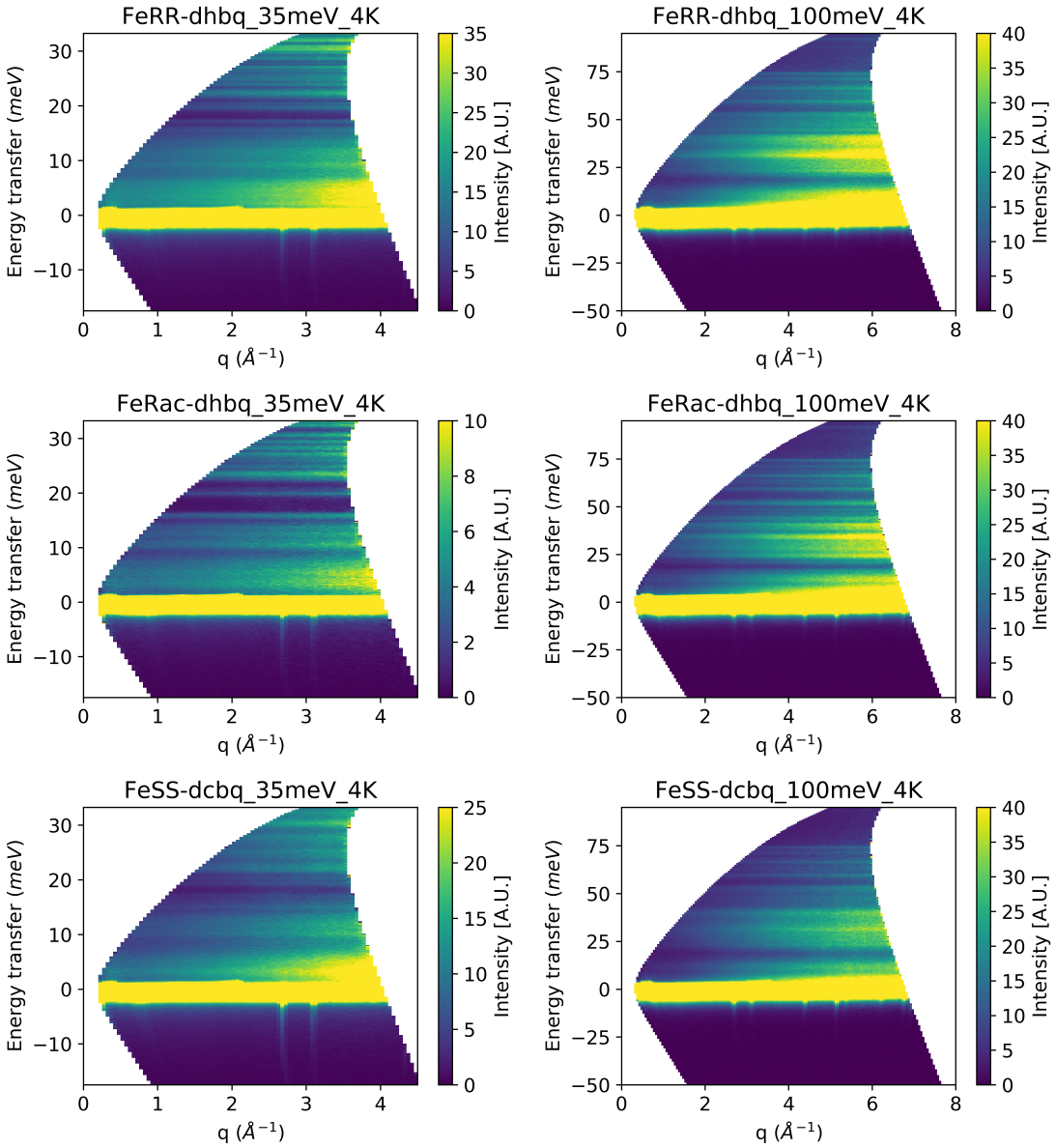

Fig. S9: INS intensity as a function of energy and momentum transfer for **1-H** (top row), **2-H** (mid row) and **1-Cl** (bottom row) measured using $E_i = 35$ meV (left column) and 100 meV (right column) at $T = 4$ K. No magnetic excitations, recognised by their decrease in intensity as Q increases, is seen for any dimer.

References

(1) Shiddiq, M.; Komijani, D.; Duan, Y.; Gaita-Arino, A.; Coronado, E.; Hill, S. Enhancing coherence in molecular spin qubits via atomic clock transitions. *Nature* **2016**, *531*, 348–351.

(2) Wedge, C. J.; Timco, G. A.; Spielberg, E. T.; George, R. E.; Tuna, F.; Rigby, S.; McInnes, E. J. L.; Winpenny, R. E. P.; Blundell, S. J.; Ardavan, A. Chemical Engineering of Molecular Qubits. *Phys. Rev. Lett.* **2012**, *108*, 107204.

(3) Ferrando-Soria, J.; Pineda, E. M.; Chiesa, A.; Fernandez, A.; Magee, S. A.; Carretta, S.; Santini, P.; Vitorica-Yrezabal, I. J.; Tuna, F.; Timco, G. A.; McInnes, E. J.; Winpenny, R. A modular design of molecular qubits to implement universal quantum gates. *Nat. Commun.* **2016**, *7*, 11377.

(4) Sanvito, S. Molecular Spintronics. *Chem. Soc. Rev.* **2011**, *40*, 3336–3355.

(5) Chicco, S.; Allodi, G.; Chiesa, A.; Garlatti, E.; Buch, C. D.; Santini, P.; De Renzi, R.; Piligkos, S.; Carretta, S. Proof-of-Concept Quantum Simulator Based on Molecular Spin Qudits. *JACS* **2024**, *146*, 1053–1061.

(6) Goodwin, C. A. P.; Ortu, F.; Reta, D.; Chilton, N. F.; Mills, D. P. Molecular Magnetic Hysteresis at 60 Kelvin in Dysprosocenium. *Nature* **2017**, *548*, 439–442.

(7) Guo, F.-S.; Day, B. M.; Chen, Y.-C.; Tong, M.-L.; Mansikkamäki, A.; Layfield, R. A. Magnetic Hysteresis up to 80 Kelvin in a Dysprosium Metallocene Single-Molecule Magnet. *Science* **2018**, *362*, 1400–1403.

(8) Perlepe, P. et al. Metal-Organic Magnets with Large Coercivity and Ordering Temperatures up to 242 °C. *Science* **2020**, *370*, 587–592.

(9) Pedersen, K. S. et al. Formation of the Layered Conductive Magnet $CrCl_2(pyrazine)_2$ through Redox-Active Coordination Chemistry. *Nat. Chem.* **2018**, *10*, 1056–1061.

(10) Perlepe, P. et al. From an Antiferromagnetic Insulator to a Strongly Correlated Metal in Square-Lattice $MCl_2(pyrazine)_2$ Coordination Solids. *Nat. Commun.* **2022**, *13*, 5766.

(11) Gould, C. A.; McClain, K. R.; Reta, D.; Kragskow, J. G. C.; Marchiori, D. A.; Lachman, E.; Choi, E.-S.; Analytis, J. G.; Britt, R. D.; Chilton, N. F.; Harvey, B. G.; Long, J. R. Ultrahard Magnetism from Mixed-Valence Dilanthanide Complexes with Metal-Metal Bonding. *Science* **2022**, *375*, 198–202.

(12) Henthorn, J.; Cutsail, G.; Weyhermüller, T.; DeBeer, S. Stabilization of intermediate spin states in mixed-valent diiron dichalcogenide complexes. *Nat. Chem.* **2022**, *14*, 328–333.

(13) McClain, K. R.; Kwon, H.; Chakarawet, K.; Nabi, R.; Kragskow, J. G. C.; Chilton, N. F.; Britt, R. D.; Long, J. R.; Harvey, B. G. A Trinuclear Gadolinium Cluster with a Three-Center One-Electron Bond and an S = 11 Ground State. *JACS* **2023**, *145*, 8996–9002.

(14) Dei, A.; Gatteschi, D.; Pardi, L.; Russo, U. Tetraoxolene Radical Stabilization by the Interaction with Transition-Metal Ions. *Inorg. Chem.* **1991**, *30*, 2589–2594.

(15) Sadhukhan, P. et al. Manipulating Electron Redistribution to Achieve Electronic Pyroelectricity in Molecular [FeCo] Crystals. *Nat. Commun.* **2021**, *12*, 4836.

(16) Carbonera, C.; Dei, A.; Létard, J.-F.; Sangregorio, C.; Sorace, L. Thermally and Light-Induced Valence Tautomeric Transition in a Dinuclear Cobalt–Tetraoxolene Complex. *Angewandte Chemie International Edition* **2004**, *43*, 3136–3138.

(17) Min, K. S.; DiPasquale, A. G.; Golen, J. A.; Rheingold, A. L.; Miller, J. S. Synthesis, Structure, and Magnetic Properties of Valence Ambiguous Dinuclear Antiferromagnetically Coupled Cobalt and Ferromagnetically Coupled Iron Complexes Containing the Chloranilate(2−) and the Significantly Stronger Coupling Chloranilate(•3−) Radical Trianion. *JACS* **2007**, *129*, 2360–2368.

(18) Min, K. S.; Rheingold, A. L.; DiPasquale, A.; Miller, J. S. Characterization of the Chloranilate(•3−) π Radical as a Strong Spin-Coupling Bridging Ligand. *Inorg. Chem.* **2006**, *45*, 6135–6137.

(19) Min, K. S.; Swierczek, K.; DiPasquale, A. G.; Rheingold, A. L.; Reiff, W. M.; Arif, A. M.; Miller, J. S. A Dinuclear Iron(II) Complex, $[(TPyA)Fe^{II}(THBQ^{2-})Fe^{II}(TPyA)](BF_4)_2$ [TPyA = tris(2-pyridylmethyl)amine; $THBQ^{2-}$ = 2,3,5,6-tetrahydroxy-1,4-benzoquinonate] Exhibiting both Spin Crossover with Hysteresis and Ferromagnetic Exchange. *Chem. Commun.* **2008**, 317–319.

(20) Min, K. S.; DiPasquale, A. G.; Rheingold, A. L.; White, H. S.; Miller, J. S. Observation of Redox-Induced Electron Transfer and Spin Crossover for Dinuclear Cobalt and Iron Complexes with the 2,5-Di-tert-butyl-3,6-dihydroxy-1,4-benzoquinonate Bridging Ligand. *JACS* **2009**, *131*, 6229–6236.

(21) Tao, J.; Maruyama, H.; Sato, O. Valence Tautomeric Transitions with Thermal Hysteresis around Room Temperature and Photoinduced Effects Observed in a Cobalt-Tetraoxolene Complex. *JACS* **2006**, *128*, 1790–1791.

(22) Abrahams, B. F.; Lu, K. D.; Moubaraki, B.; Murray, K. S.; Robson, R. X-Ray Diffraction and Magnetic Studies on a Series of Isostructural Divalent Metal Chloranilates with Zigzag Polymeric Chain Structures and on a Dinuclear Iron(III) Chloranilate. *J. Chem. Soc., Dalton Trans.* **2000**, 1793–1797.

(23) Clutterbuck, K. M.; Abrahams, B. F.; Hudson, T. A.; van Koeverden, M. P. "Mixed Valency in a Neutral 1D Fe-Chloranilate Coordination Polymer". *Dalton Trans.* **2022**, *51*, 9199–9205.

(24) Jeon, I.-R.; Negru, B.; Van Duyne, R. P.; Harris, T. D. A 2D Semiquinone Radical-Containing Microporous Magnet with Solvent-Induced Switching from Tc = 26 to 80 K. *JACS* **2015**, *137*, 15699–15702.

(25) Wang, Y.; Ziebel, M. E.; Sun, L.; Gish, J. T.; Pearson, T. J.; Lu, X.-Z.; Thorarinsdottir, A. E.; Hersam, M. C.; Long, J. R.; Freedman, D. E.; Rondinelli, J. M.; Puggioni, D.; Harris, T. D. Strong Magnetocrystalline Anisotropy Arising from Metal–Ligand Covalency in a Metal–Organic Candidate for 2D Magnetic Order. *Chemistry of Materials* **2021**, *33*, 8712–8721.

(26) van Koeverden, M. P.; Abrahams, B. F.; D'Alessandro, D. M.; Doheny, P. W.; Hua, C.; Hudson, T. A.; Jameson, G. N. L.; Murray, K. S.; Phonsri, W.; Robson, R.; Sutton, A. L. Tuning Charge-State Localization in a Semiconductive Iron(III)–Chloranilate Framework Magnet Using a Redox-Active Cation. *Chemistry of Materials* **2020**, *32*, 7551–7563.

(27) Darago, L. E.; Aubrey, M. L.; Yu, C. J.; Gonzalez, M. I.; Long, J. R. Electronic Conductivity, Ferrimagnetic Ordering, and Reductive Insertion Mediated by Organic Mixed-Valence in a Ferric Semiquinoid Metal–Organic Framework. *JACS* **2015**, *137*, 15703–15711.

(28) Kitagawa, S.; Kawata, S. Coordination Compounds of 1,4-dihydroxybenzoquinone and its Homologues. Structures and Properties. *Coord. Chem. Rev.* **2002**, *224*, 11–34.

(29) Demir, S.; Jeon, I.-R.; Long, J. R.; Harris, T. D. Radical Ligand-Containing Single-Molecule Magnets. *Coord. Chem. Rev.* **2015**, *289-290*, 149–176, Prog. Magnetochem.

(30) Train, C.; Gruselle, M.; Verdaguer, M. The Fruitful Introduction of Chirality and Control of Absolute Configurations in Molecular Magnets. *Chem. Soc. Rev.* **2011**, *40*, 3297–3312.

(31) Brandt, J. R.; Salerno, F.; Fuchter, M. J. The Added Value of Small-Molecule Chirality in Technological Applications. *Nature Reviews Chemistry* **2017**, *1*, 0045.

(32) Baker, M. L.; Guidi, T.; Carretta, S.; Ollivier, J.; Mutka, H.; Güdel, H. U.; Timco, G. A.; McInnes, E. J. L.; Amoretti, G.; Winpenny, R. E. P.; Santini, P. Spin

dynamics of molecular nanomagnets unravelled at atomic scale by four-dimensional inelastic neutron scattering. *Nat. Phys.* **2012**, *8*, 906–911.

(33) Mirebeau, I.; Hennion, M.; Casalta, H.; Andres, H.; Güdel, H. U.; Irodova, A. V.; Caneschi, A. Low-Energy Magnetic Excitations of the Mn_{12}-Acetate Spin Cluster Observed by Neutron Scattering. *Phys. Rev. Lett.* **1999**, *83*, 628–631.

(34) Magee, S. A.; Sproules, S.; Barra, A.-L.; Timco, G. A.; Chilton, N. F.; Collison, D.; Winpenny, R. E. P.; McInnes, E. J. L. Large Zero-Field Splittings of the Ground Spin State Arising from Antisymmetric Exchange Effects in Heterometallic Triangles. *Angewandte Chemie International Edition* **2014**, *53*, 5310–5313.

(35) Kragskow, J. G. C.; Marbey, J.; Buch, C. D.; Nehrkorn, J.; Ozerov, M.; Piligkos, S.; Hill, S.; Chilton, N. F. Analysis of vibronic coupling in a 4f molecular magnet with FIRMS. *Nat. Commun.* **2022**, *13*, 825.

(36) Tait, A. M.; Busch, D. H.; Curtis, N. F. *Inorganic Syntheses*; John Wiley & Sons, Ltd, 1978; pp 10–17.

(37) Sheldrick, G. M. Crystal structure refinement with *SHELXL*. *Acta Crystallogr. Sec. C* **2015**, *71*, 3–8.

(38) Sheldrick, G. M. *SHELXT* – Integrated space-group and crystal-structure determination. *Acta Crystallogr. Sec. A* **2015**, *71*, 3–8.

(39) Dolomanov, O. V.; Bourhis, L. J.; Gildea, R. J.; Howard, J. A. K.; Puschmann, H. *OLEX2*: A complete structure solution, refinement and analysis program. *J. Appl. Crystallogr.* **2009**, *42*, 339–341.

(40) Bain, G. A.; Berry, J. F. Diamagnetic Corrections and Pascal's Constants. *J. Chem. Educ.* **2008**, *85*, 532.

(41) Ollivier, J.; Mutka, H. IN5 Cold Neutron Time-of-Flight Spectrometer, Prepared to Tackle Single Crystal Spectroscopy. *JPSJ* **2011**, *80*, SB003.

(42) Appel, M.; Frick, B.; Magerl, A. A Flexible High Speed Pulse Chopper System for an Inverted Neutron Time-of-Flight Option on Backscattering Spectrometers. *Scientific Reports* **2018**, *8*, 13580.

(43) Appel, M.; Frick, B.; Magerl, A. First results with the neutron backscattering and TOF spectrometer option BATS on IN16B. *Phys. B: Condens.* **2019**, *562*, 6–8.

(44) Granroth, G. E.; Kolesnikov, A. I.; Sherline, T. E.; Clancy, J. P.; Ross, K. A.; Ruff, J. P. C.; Gaulin, B. D.; Nagler, S. E. SEQUOIA: A Newly Operating Chopper Spectrometer at the SNS. *J. Phys. Conf. Ser.* **2010**, *251*, 012058.

(45) Arnold, O. et al. Mantid—Data analysis and visualization package for neutron scattering and μSR experiments. *Nucl. Instrum. Methods Phys. Res. A: Accel. Spectrom. Detect. Assoc. Equip.* **2014**, *764*, 156 – 166.

(46) Mantid: Manipulation and Analysis Toolkit for Instrument Data.; Mantid Project. 2013; http://dx.doi.org/10.5286/SOFTWARE/MANTID6.4.

(47) Le Mardelé, F. FieldOptic. 2024; https://github.com/LeMardele/FieldOptic.

(48) Echeverría, J.; Alvarez, S. Application of Symmetry Operation Measures in Structural Inorganic Chemistry. *Inorg. Chem.* **2008**, *47*, 10965–10970.

(49) Baker, M. L. *mint*: Simulation of Inelastic Neutron Scattering Induced Magnetic Excitations for Single-Ions & Finite Exchange Coupled Spin-systems. 2022; https://mlbakerlab.co.uk/mint.

(50) Bauer, E.; Rotter, M. *Properties and Applications of Complex Intermetallics*; pp 183–248.

(51) Stoll, S.; Schweiger, A. EasySpin, a comprehensive software package for spectral simulation and analysis in EPR. *J. Magn. Reson.* **2006**, *178*, 42–55.

(52) Baker, M. L.; Blundell, S. J.; Domingo, N.; Hill, S. In *Molecular Nanomagnets and Related Phenomena*; Gao, S., Ed.; Springer Berlin Heidelberg: Berlin, Heidelberg, 2015; pp 231–291.

(53) Squires, G. L. *Introduction to the Theory of Thermal Neutron Scattering*; Cambridge University Press, 1978.

(54) Rauch, H.; Waschkowski, W. In *Neutron Data Booklet*; Dianoux, A.-J., Lander, G., Eds.; OCP Science, 2003; pp 1.1–1,1.1–17.

(55) Wan, W. Spectroscopy Study of Low-dimensional Quantum Magnets. Ph.D. thesis, 2021.

(56) Weihe, H.; Güdel, H. U. Angular and Distance Dependence of the Magnetic Properties of Oxo-Bridged Iron(III) Dimers. *JACS* **1997**, *119*, 6539–6543.

(57) Wrobleski, J. T.; Brown, D. B. Synthesis, Magnetic Susceptibility, and Moessbauer Spectra of Iron(III) Dimers and Iron(II) Polymers containing 2,5-dihydroxy-1,4-benzoquinones. *Inorg. Chem.* **1979**, *18*, 498–504.

(58) Lloret, F.; Julve, M.; Faus, J.; Solans, X.; Journaux, Y.; Morgenstern-Badarau, I. Synthesis and Magnetic Properties of Binuclear Iron(III) Complexes with Oxalate, 2,5-dihydroxy-1,4-benzoquinone Dianion, and Squarate as Bridging Ligands. Crystal Structure of (μ-1,3-squarato)bis[(N,N'-ethylenebis(salicylideneaminato))(methanol)iron(III)]. *Inorg. Chem.* **1990**, *29*, 2232–2237.

(59) Thorarinsdottir, A. E.; Bjornsson, R.; Harris, T. D. Insensitivity of Magnetic Coupling

to Ligand Substitution in a Series of Tetraoxolene Radical-Bridged Fe_2 Complexes. *Inorganic Chemistry* **2020**, *59*, 4634–4649.

TOC Graphic

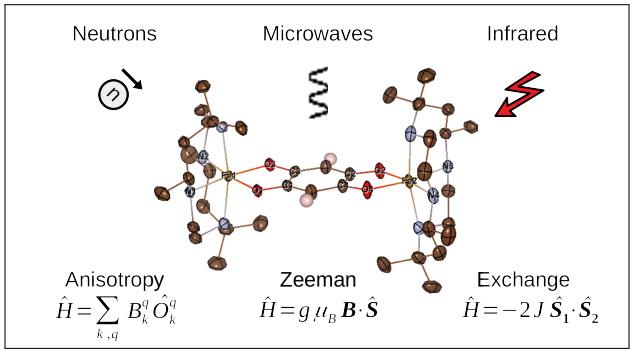
Neutrons
Microwaves
Infrared
Anisotropy
$\hat{H} = \sum_{k,q} B_k^q \hat{O}_k^q$
Zeeman
$\hat{H} = g \mu_B \boldsymbol{B} \cdot \hat{\boldsymbol{S}}$
Exchange
$\hat{H} = -2J \hat{\boldsymbol{S}}_1 \cdot \hat{\boldsymbol{S}}_2$

Chapter 4

Manuscript 2: Double Exchange Spin Dynamics within a Valence Delocalised Molecule

4.1 Prelude to Chapter

The research presented in this chapter sought to quantify valence delocalised spin dynamics within a molecule using INS for the first time. We chose to study a well-known molecule from the literature, $2\,Fe^{3+}Fe^{2+}O[O_2CC(CD_3)_3]_6(C_5D_5N)_3$ (**Fe_3-Piv**) [29]. Among other things, the crystallographic details about this molecule are well known, which allowed us to focus on the particular details about its spin dynamics rather than a more general description. The existence of analogous localised, delocalised, and mixed-metal molecules furthermore allowed us to do a comparative study [87]–[92]. Lastly, the facile synthesis of **Fe_3-Piv** and the availability of deuterated precursors meant that we had access to high-quality deuterated powder samples on the gramme scale.

Using the cold neutron time-of-flight spectrometer LET at ISIS Neutron and Muon Source, we were able to obtain rich INS data of high-quality. To interpret the observed spin dynamics, we developed a spin Hamiltonian modelling tool capable of simulating the INS spectra of models including Heisenberg exchange, double exchange and single-ion anisotropies. Our best fit provided an excellent description of most of the observed magnetic excitations and established **Fe_3-Piv** as a class II valence delocalised molecule with a mobile electron being shared at a 88/12 % distribution between two centres within the ground state. We also showcased the capability of our new modelling tool to calculate the 3D momentum tranfer dependencies of double exchange excitations. Simulations of our best model predicts that INS is sensitive to partial localisation within molecules, which future single-crystal INS experiments on deuterated single crystals could unravel.

Dr C. Balz carried out the INS experiment with online participation from R. T. Christiansen. Complete information about individual contributions can be found in the ”Author Contributions” section within the draft, which we intend to submit to a chemistry journal.

Double Exchange Spin Dynamics within a Valence Delocalised Molecule

R. T. Christiansen,[†,‡,¶] G. A. Timco,[‡] R. E. P. Winpenny,[‡] C. Balz,[§] F. Le Mardelé,[‖] M. Orlita,[‖,⊥] R. Clérac,[#,@] J. Ollivier,[†] and M. L. Baker[*,‡,¶]

†*Spectroscopy Group, Institut Laue-Langevin, 38042 Grenoble Cedex 9, France*

‡*Department of Chemistry, the University of Manchester, Manchester M13 9PL, UK*

¶*The University of Manchester at Harwell, Diamond Light Source, Didcot OX11 0DE, UK*

§*ISIS Facility, STFC Rutherford-Appleton Laboratory, Didcot OX11 0QX, UK*

‖*LNCMI-EMFL, CNRS UPR3228, Université Grenoble Alpes, Université Toulouse, Université Toulouse 3, INSA-T, 38042 Grenoble and Toulouse Cedex 9, France*

⊥*Faculty of Mathematics and Physics, Charles University, 121 16 Prague, Czech Republic*

#*CNRS, UMR 5031, Centre de Recherche Paul Pascal, 33600 Pessac, France*

@*Université de Bordeaux, UMR 5031, 33600 Pessac, France*

E-mail: michael.baker@manchester.ac.uk

Abstract

Delocalisation of the extra electron(s) within mixed-valence molecules can contribute to intramolecular magnetic exchange alongside conventional mechanisms. This interaction, typically named double exchange, can lead to exotic magnetic phenomena like intermediate spin ground states and molecular multiferroicity. However, quantitative assessment of valence delocalised spin dynamics have remained elusive despite significant fundamental interest and the promising utility of mixed-valence molecules. We show that combining inelastic neutron scattering (INS) with our newly developed

modelling tool can fully characterise the spin dynamics of valence delocalised molecules, exemplified by our study of a pair-delocalised $Fe^{2.5+}$-$Fe^{2.5+}$-Fe^{3+} trimer. We find that double exchange is responsible for the emergence of novel low-energy spin excitations absent in analogous localised trimers. Our simulations predict that certain double exchange excitations have unique the momentum transfer (**Q**) dependencies and that the **Q**-dependencies of all probed excitations are highly sensitive to preferential occupation of the delocalised electron(s). This shows that single-crystal INS experiments, which directly probe the **Q**-dependencies of molecular spin excitations, could provide quantitative measurements of the distribution of delocalised valence electron(s) within mixed-valence molecules.

Introduction

Magnetic molecules have been the subject of intense studies since the discovery of magnetic bistability in Mn_{12}-acetate in the early 90's.[1] They have provided unique model systems for investigating fundamental quantum phenomena like tunnelling of the magnetisation and of the Néel vector and quantum coherence.[2–5] Molecule-based magnetic materials are also on the forefront of technological development with promising utility as e.g. next-generation permanent magnets,[6,7] as qubits,[8–10] and as molecular-sized switches for magnetic memory and spintronic applications.[11–13] Motivated by this wide array of potential applications scientists continue to search for breakthroughs that would elevate molecular materials to the next level of applicability. A particularly desirable quantity would be easy and efficient control of molecular spin states via external stimuli, for example applied electric fields.[14,15]

In theory, magnetic molecules that contain metal centres in formally different oxidation states, mixed-valence (MV) molecules, are excellent candidates for realising this goal. Within these clusters, the "extra" valence electron(s) can become delocalised when the available orbitals are (near-)degenerate. As a consequence, an additional intramolecular magnetic interaction, known as double exchange, emerges.[16–18] Double exchange scales linearly with S, the

total spin quantum number, and usually promotes a parallel alignment of neighbouring spins due to spin polarisation of the delocalised electron. In contrast, conventional Heisenberg exchange scales as $S(S+1)$ and tends to promote anti-parallel alignment. Evidently, situations where these two mechanisms compete can occur, which can give rise to unique intermediate-spin ground states.[19] Supposedly, this competition can be controlled by applying an electric field, which perturbs the delocalisation potential and causes the spin ground state to change for sufficiently strong fields.[20,21] In biology, many enzymes contain MV molecules at their active sites, and electron transfer plays a critical role for their reactivity.[22]

Unfortunately, the magneto-structural correlations that govern double exchange within molecules remain poorly understood due to a lack of quantitative experimental evidence, largely because the typical methods for probing the magnetism of MV molecules, such as magnetometry and visible light spectroscopy, only provide indirect information about the spin dynamics. Furthermore, the lack of powerful modelling tools has often lead to overparameterisation and has hindered the simultaneous elucidation of important mechanisms like exchange couplings and single-ion anisotropies.

We propose to use INS to tackle this problem. To make this feasible, we have developed a spin Hamiltonian modelling tool capable of incorporating double exchange, conventional exchange interactions and single-ion anisotropies, including higher-order Steven's operators, into the same model. The tool utilises the analytical solution to the isotropic Heisenberg-double exchange problem from Ref. 23, which we have implemented into a formalism compatible with Easyspin and *mint*.[24,25] This compatibility makes it possible to, for the first time, calculate the magnetic properties of arbitrary spin Hamiltonian models with both double exchange and other traditional magnetic interactions included. Furthermore, the tool can simulate inelastic neutron scattering (INS) spectra of both powders and single crystals, which has the potential to provide unprecedented information about valence delocalised spin dynamics. Lastly, the tool also quantifies the distribution of the delocalised electron(s) for each eigenstate.

We exemplify the capabilities of our approach through the first direct investigation of the electronic structure of $2\,Fe^{3+}Fe^{2+}O[O_2CC(CD_3)_3]_6(C_5D_5N)_3$, a proposed class II valence delocalised molecule in which an electron undergoes thermally activated electrons transfer between two of the three iron sites.[26,27] Powder INS experiments provide the empirical basis for constraining a double exchange model that accurately describes the spin dynamics of **Fe_3-Piv**, which a localised model fails to do. Furthermore, simulations of single-crystal INS experiments show that particular double exchange excitations have unique signatures in their momentum transfer ($\mathbf{Q}$) dependencies and that single-crystal INS has the potential to quantify the distribution of delocalised valence electrons within molecules based on experimental data.

Results and Discussion

Fe_3-Piv, the Valence Delocalised Molecule

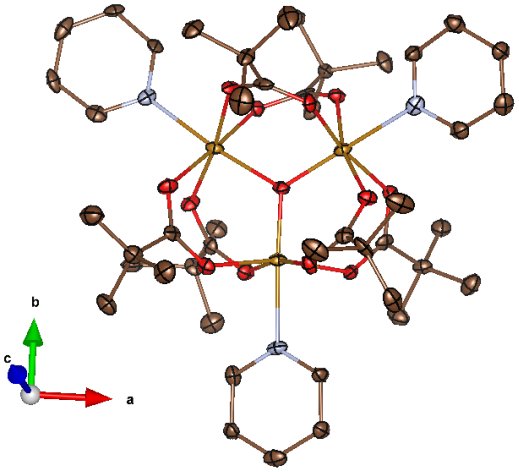

Fig. 1: Structure of $2\,Fe^{3+}Fe^{2+}O[O_2CC(CD_3)_3]_6(C_5D_5N)_3$ (**Fe_3-Piv**) with 50 % probability ellipsoids, obtained from single-crystal X-ray diffraction data and plotted using VESTA.[26,28] Brown: C, blue: N, red: O, gold: Fe. Hydrogens/deuteriums are omitted for clarity.

Fig. 1 shows the structure of **Fe_3-Piv**, the molecule we chose to study to exemplify the capabilities of our newly developed approach.[26,29–31] It is an extraordinarily well charac-

terised member of the general carboxylate trimer family, $[M_3O(O_2CR)_6L_3](S)$, which notably also encompasses its oxidised (R = $C(CH_3)_3$, L = MeOH, S = Cl) and mixed-metal (M^{2+} = Mn^{2+}/Ni^{2+}) analogues (**Fe_2Ni-Piv** and **Fe_2Mn-Piv**), which all only contain localised electrons. The mixed-valence acetate analogue (R = CH_3, S = C_5H_5N, **Fe_3-OAc**), has also been investigated.[32–37]

Fe_3-Piv contains a near-isosceles triangular core of iron ions with a combined valence of +8 connected by a central μ_3-O within the Fe plane. Two pivalate groups bridge the irons along each edge of the triangle, and terminal pyridines complete the pseudo-octahedral iron coordination. The Fe-Fe distance along the unique edge is 3.2424(17) Å, while the separations along the near-equal edges are 3.359(2) Å and 3.3144(19) Å, respectively. The molecule is neutral overall and crystallises without solvent in the $P2_1$ space group with only one molecule in the asymmetric unit. These two features simply data analysis, and together with the possibility for comparing our results to several analogues, they make **Fe_3-Piv** an excellent model system.

Formally, the core of **Fe_3-Piv** contains three high-spin iron ions, two Fe^{3+} ($s = 5/2$) and one Fe^{2+} ($s = 2$). However, thermally activated electron transfer occurs between the two sites on the unique edge of the isosceles triangle, while the last site remains Fe^{3+} at all times. Consequently, it is proposed that **Fe_3-Piv** belongs class II in the typical Robin and Day classification scheme for valence delocalised molecules.[27,38–42] While the physical origin of the lowering from C_{3v} point symmetry has not been experimentally verified, it likely comes from the combined effects of double exchange and vibronic coupling. It is well established that coupling of magnetic degrees of freedom to the in-plane asymmetric stretch of the Fe_3O core can cause this kind of symmetry breaking, which suggests that double exchange is indeed important for the spin dynamics of this molecule.[43,44]

Magnetic measurements (see Fig. S1) show that **Fe_3-Piv** has an $S = 2$ magnetic ground state with a substantial easy-axis anisotropy. The magnetic susceptibility plateaus at $\chi T = 3$ cm^3 K/mol around $T = 40$ K, the exact value expected for an isolated $S = 2$ ground state.

Field-dependent magnetisation curves measured at $T = 2$ and 5 K do not reach saturation at $B = 7$ T, which suggest that the zero-field splitting (ZFS) between the $m_S = \pm 2$ and $m_S = \pm 1$ doublets within the ground manifold is $\Delta \approx 1.2\,\text{meV} \approx 10\ \text{cm}^{-1}$. The orbital degeneracy of the Fe^{2+} site presumably causes this anisotropy.

This is in stark contrast to **Fe_3-OAc**, which has an $S = 1$ ground state.[33] One would expect the magnetic interactions in this class of compounds to predominantly be mediated by the central μ_3-O, and, as a consequence, that substitutions on the carboxylate bridge would only have minor effects on the magnetic properties. However, the change in spin ground state between **Fe_3-Piv** and **Fe_3-OAc** show that this is not the case. Once again, this can be understood in the light of vibronic coupling. IR vibrational spectroscopy studies of isotope-enriched **Fe_3-Piv** samples showed that the in-plane asymmetric stretching mode ν_{Fe_3O} couples to the carboxylate deformation mode.[45] This explains how substitution on the carboxylate bridges, far away from the magnetic core, can affect vibronic coupling and thereby influence the magnetic properties.

Our magnetic measurements also contains preliminary information about the intramolecular magnetic interactions. The susceptibility-temperature product increases with increasing temperature, which tells that significant antiferromagnetic interactions are at play like in the localised mixed-metal analogues **Fe_2Ni-Piv** and **Fe_2Mn-Piv**.[37] However, the χT-curve does not contain sufficient information for constraining the spin dynamics of **Fe_3-Piv**.

Inelastic Neutron Scattering

INS is a unique spectroscopic probe capable of directly measuring the energy gaps between the magnetic states of a molecule thanks to the magnetic moment of the neutron. Two sets of strong selection rules, $\Delta S = \pm 1, 0$ and $\Delta m_S = \pm 1, 0$, give experimental access to molecular spin excitations and ZFSs, respecively. Fig. 2 shows INS spectra measured on a deuterated powder sample; three high-resolution spectra measured at $T = 1.6$, 5, and 25 K using neutrons with incident energy $E_i = 3$ meV and one broad-band spectrum measured at

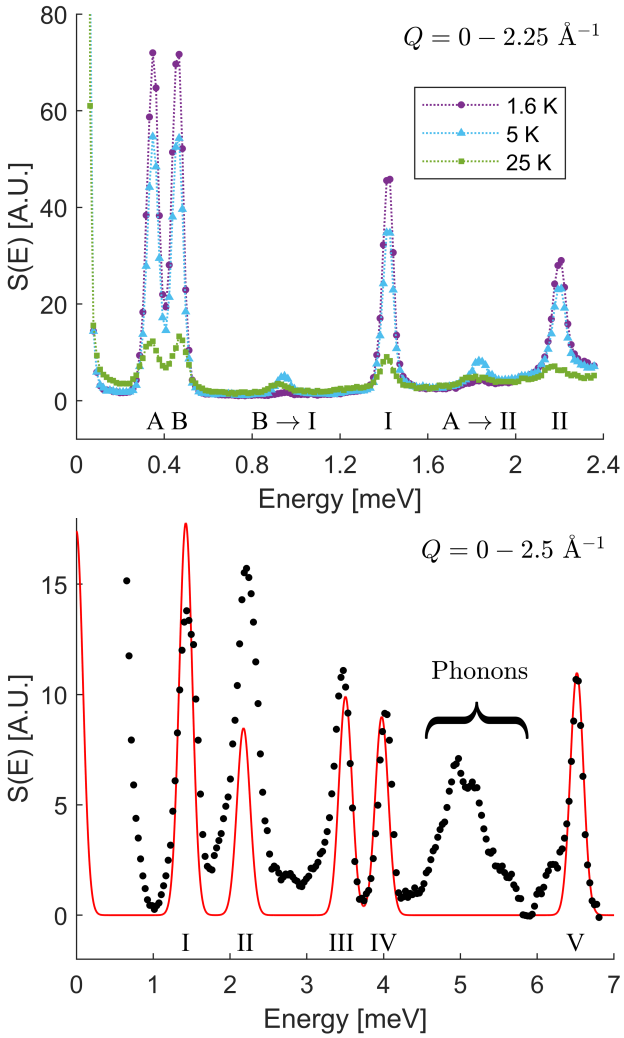

Fig. 2: Powder INS spectra of **Fe_3-Piv**. **Top:** $S(E)$ measured using $E_i = 3$ meV at $T = 1.6$ K (purple circles), 5 K (blue triangles) and 25 K (green squares). The dotted line is a guide to the eye. **Bottom**: $S(E)$ measured using $E_i = 10$ meV at $T = 1.6$ K (black circles) overplotted with a simulation (red line) based on the best fit of the scalene triangle model (Fig. 3) to the positions and relative intensities of the INS transitions. The cluster of peaks centred at 5 meV are all incoherent phonons. Letters and roman numerals numerate the observed transitions in both plots. Errorbars are smaller than the markers in both plots.

$T = 1.6$ K using $E_i = 10$ meV.

The $E_i = 3$ meV spectra contain 4 magnetic excitations from the ground state (cold transitions), labelled A, B, I and II. For $T \geq 5$ K, they also contain two excitations between excited states (hot transitions), B→I and A→II. All four features can be assigned as magnetic due their decrease in intensity with increasing $Q = |\mathbf{Q}|$ (see Fig. S2). The broad-band spectrum also contains I and II alongside three additional cold magnetic excitations, labelled III-V. The features centered at $E \approx 5$ meV are incoherent phonons recognised by their characteristic Q-dependence ($S(Q) \propto Q^2$). Fitting of appropriate line shapes (Lorentzian for II, Gaussin for the others) revealed that the seven magnetic transitions are located at $\hbar\omega = 0.3634(4)$, $0.4747(7)$, $1.4336(4)$, $2.2101(6)$, $3.4452(6)$, $4.0098(6)$, and $6.5052(5)$ meV. The integrated intensities of I-V at $T = 1.6$ K are $0.0436(3)$, $0.0925(7)$, $0.0313(3)$, $0.0209(2)$, and $0.0248(3)$, respectively.

Excitation I resembles the transition from the ground $m_S = \pm 2$ doublet to the excited $m_S = \pm 1$ doublet within the ground $S = 2$ manifold based on its quick decay with increasing Q (see Fig. 5). The excitation energy, $\hbar\omega = 1.4336(4)$ meV, agrees excellently with the estimate of $\Delta \approx 1.2$ meV from field-dependent magnetisation data.

We assign excitations II-V as transitions to excited spin manifolds based on the modulation of their intensities as a function of Q (see Figs. S2 and 5). These modulations are governed by the relative positions of the magnetic ions and the composition of the wave functions of the involved states. Therefore, they can be used to differentiate between different types of excitations.[46,47] Unfortunately, our data contains significant phonon contributions at $Q > 2$ Å^{-1} despite our use of deuterated samples from which phonon scattering is weaker due to the small incoherent neutron cross section of deuterium.[48] Therefore, the Q-dependencies could only be extracted after significant background corrections that introduce significant uncertainties at $Q > 2$ Å^{-1}. Consequently, the intensity modulations of all excitations are difficult to distinguish, except for excitation II, which shows less pronounced oscillations (see Fig. S2). However, II also has the largest phonon background, which complicates the back-

ground subtraction and presumably hides the oscillations. Excitation II does however stand out when it comes to its INS line shape, it is Lorentizian instead of Gaussian. Furthermore, its full width at half maximum (FWHM) shows a pronounced temperature dependence; it is approximately twice as large at $T = 25$ K compared to $T = 1.6$ K. This suggests that a phonon-assisted process could be related to the relaxation from II, however measurements at more temperatures are necessary to quantify this further.[49,50]

The presence of one ZFS excitation and four spin excitations below $\hbar\omega = 7$ meV in **Fe_3-Piv** is in stark contrast to the energy levels reported for its oxidised and mixed-metal analogues. Those clusters, which only contain localised electrons, all have one low-lying spin excitation around $\hbar\omega = 2.3$ meV, while the remaining spin excitations lie above $\hbar\omega = 9$ meV.[35,37] This shows that the magnetic interactions that govern the spin dynamics of **Fe_3-Piv** are fundamentally different from its localised counterparts.

Even **Fe_3-OAc**, in which the extra electron undergoes thermally activated transfer between 112 K and 191 K, has a magnetic spectrum that closely resembles those of the localised clusters, the reason being that electron transfer likely does not occur at the temperature of the reported INS measurements ($T = 5$ K).[33,51,52] The onset of electron transfer in **Fe_3-OAc** is related to one of its four structural phase transitions. It is likely that the structural changes affect the energies of the accessible orbitals such that delocalisation suddenly becomes possible at $T > 112$ K.[52] This explains why the magnetic spectrum collected at $T = 5$ K resembles those of the localised analogues. No structural phase transitions appear in **Fe_3-Piv**. Instead, its crystal structure shows that electron transfer remains T-dependent down to 10 K. At that point, there is not enough thermal energy to overcome the transfer barrier. The electron occupation asymmetry suggests that there is a gap between the minima of the potential energy surface that correspond to electron localisation on either site within the delocalised pair. Wilson et al estimate that this gap is less than 12.4 meV.[26]

With the nature of transitions I-V accounted for we shift our focus to excitations A and B. The quick decays of their intensities with increasing Q alongside the existence of hot bands

B→I and A→II provide unambiguous evidence for their magnetic origin, yet their exact natures remain unclear. Their intensities decrease faster with increasing Q than expected for a ZFS excitation (see Fig. S2). Our modelling furthermore showed that including them in a description of the ZFS alongside excitation I is incompatible with the observed field-dependent magnetisation, the equal INS intensities of A/B and the temperature dependence of the INS spectra. Thus, single-ion anisotropies, which are typically the origin of low-lying magnetic excitations in transition metal compounds, cannot be the origin of A and B.

Without further context, one could assign A and B as coming from intermolecular interactions. In **Fe_3-OAc**, intermolecular interactions mediated by π-π stacking of the pyridine ligands in neighbouring molecules have been proposed as the origin of a forest of magnetic excitations found between 0.24 meV and 2.2 meV. At 200 K, the iron sites in **Fe_3-OAc** are indistinguishable due to dynamic rotational disorder caused by intramolecular electron transfer. As the temperature decreases and the electrons become localised, these intermolecular interactions supposedly cause domian formation with local ordering of the now localised electron, which creates local field anisotropies that split the ground state of molecules in slightly different local environments. However, such a mechanism is not possible in **Fe_3-Piv**. Only one molecule exists in the asymmetric unit, and the three iron sites are crystallographically distinguishable at all temperatures, which means that such local field anisotropies cannot emerge. Also, the pyridine ligands of neighbouring **Fe_3-Piv** molecules are at angle to one-another ($\approx 30°$) in contrast to in **Fe_3-OAc**, where they are co-planar. Thus, intermolecular interactions in **Fe_3-Piv** would be mediated via long H···H bonds ($\sim$ 3 Å) instead of π-π stacking, which would make them significantly weaker than in **Fe_3-OAc**.[26] Consequently, the natures of A and B remain unknown despite their unambiguous magnetic origin, which prevents them from being incorporated into our model going forward.

The Double Exchange Model

Our analysis of the powder INS spectra in Fig. 2 showed that the spin dynamics of **Fe$_3$-Piv** are rich and fundamentally different from its localised analogues, which necessitates the inclusion of double exchange when modelling its properties. In a general case, this inclusion necessitates accurate tracking of all possible distributions D_i of the mobile electron(s).[23] For **Fe$_3$-Piv** there are effectively only two such distributions, the extra electron residing on either site within the delocalised pair, since the combination of double exchange and vibronic coupling prevents delocalisation onto the third site. Including the third distribution without explicitly accounting for vibronic coupling will lead to models that represent undesirable physical situations such as delocalised electron density on the third site.

The effect of double exchange is to mix all the localised systems that are defined by the electron distributions D_i. For **Fe$_3$-Piv** the double exchange Hamiltonian is given by[53]

$$\mathcal{H}_{\mathbf{Fe_3\text{-}Piv}} = \begin{bmatrix} \mathcal{H}_{\text{local}}(D_1) + U(D_1) & \mathcal{T} \\ \mathcal{T} & \mathcal{H}_{\text{local}}(D_2) + U(D_2) \end{bmatrix} \tag{1}$$

where $\mathcal{H}_{\text{local}}(D_i)$ is the Hamiltonian describing the localised system i with distribution D_i of the extra electron. $U(D_i)$ defines a possible intrinsic energy cost associated with a particular electron distribution, e.g. inequality of certain magnetic centres. For **Fe$_3$-Piv** we assume that $U = 0$ and let the differences between $\mathcal{H}_{\text{local}}(D_1)$ and $\mathcal{H}_{\text{local}}(D_2)$ govern the inequality of the two sites within the delocalised pair.

The local Hamiltonians contain the Heisenberg exchange interactions between each site as well as the their axial single-ion anisotropies:

$$\mathcal{H}_{\text{local}} = -\sum_{i,j,i\neq j} J_{ij}(\mathbf{s}_i \cdot \mathbf{s}_j) + \sum_i d_i \hat{s}_{z,i}^2 \tag{2}$$

where $\mathbf{S}_i$ is the spin operator for site i, J_{ij} is the Heisenberg exchange constant between sites i and j, $\hat{s}_{z,i}$ is the spin projection operator along z for site i and d_i is the anisotropy

parameter for the same site. We assume that the local anisotropy axes are perpendicular to the Fe_3O plane. Note that J_{ij} for a particular pair may vary drastically for different D's. For carboxylate trimers, M^{2+}-Fe^{3+} exchange constants typically lie around $J^{d^n-d^{n+1}}$=-2.5 meV, while $J^{d^n-d^n}$'s are three to four times larger.[33,35]

$\mathcal{T}$ governs the mixing of the localised systems and is given by[23]

$$\mathcal{T} = t \sum_{\sigma} c^{\dagger}_{2\phi\sigma} c_{1\phi\sigma} \tag{3}$$

where t parameterises the strength of double exchange within the delocalised pair and the operators $c^{\dagger}_{i\phi\sigma}/c_{i\phi\sigma}$ are the second quantisation operators that create and annihilate an electron with spin σ in orbital ϕ on site i, respectively.

Evidently, the dimension of $\mathcal{H}_{\mathbf{Fe_3\text{-}Piv}}$ is twice that of the local Hamiltonians, who are usually expressed in the product state basis $|m_{s,1}\rangle\,|m_{s,2}\rangle \cdots |m_{s,N}\rangle$ for a system with N magnetic centres. When including double exchange, one constructs the basis vectors by combining the product state vectors for each $\mathcal{H}_{\text{local}}$. For $\mathcal{H}_{\mathbf{Fe_3\text{-}Piv}}$, the basis vectors become $|D, m_{s,1}, m_{s,2}, m_{s,3}\rangle$, where $D = 1, 2$ denotes the electron distribution and $m_{s,i}$ is the projection of the spin of site i. There are always two $s = 5/2$ sites and one $s = 2$ site; D determines which site has $s = 2$. In this basis, the contribution of a distribution D' to the overall distribution of the extra electron(s) is given by the trace over the subspace defined by D' of the outer product of an eigenstate with itself. For example, for an arbitrary eigenstate $|\psi\rangle$, $\mathrm{Tr}_{D1}(|\psi\rangle\langle\psi|)$ yields a number between 0 and 1 that represents the contribution of D_1 to the overall distribution of the delocalised electron within $|\psi\rangle$. $\mathrm{Tr}_{D1}(|\psi\rangle\langle\psi|) = 0.91$ would, for example, mean that 91 % of the delocalised electron density is located on site 1 for an **Fe_3-Piv** molecule in state $|\psi\rangle$.

Fig. 3 (LHS) shows a schematic of the model we employed to fit the INS data. It contains six parameters in total: t, which parameterises double exchange within the delocalised pair, J, which parameterises both $J^{d^n-d^n}$ and $J^{d^n-d^{n+1}}$ for each bond, δ_1/δ_2, which parameterise

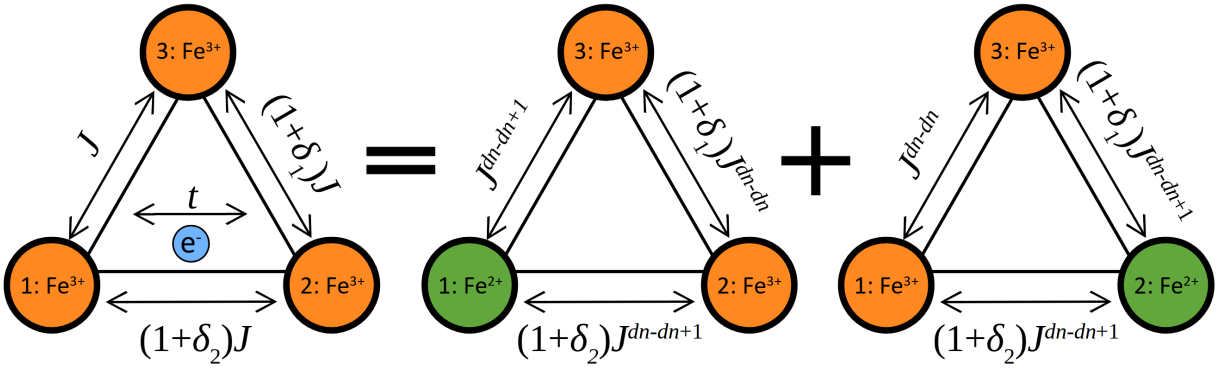

Fig. 3: Schematic of the scalene triangle double exchange model for **Fe_3-Piv** (LHS). Double exchange, parameterised by t, mixes the localised systems on the RHS. In the double exchange model, J contains two contributions, $J^{d^n-d^n}$ and $J^{d^n-d^{n+1}}$, which correspond to Fe^{3+}-Fe^{3+} and Fe^{3+}-Fe^{2+} Heisenberg interactions, respectively. δ_1 and δ_2 quantify the deviation from equilateral symmetry. Within each localised system, we assume that only the Fe^{2+} site is anisotropic, an axial anisotropy governed by d.

the departure from equilateral symmetry, and d, which parameterises the axial anisotropy of the Fe^{2+} site. The Fe^{3+} site may also have minor anisotropy, however, for simplicity, we assume that it is vanishing in comparison to the Fe^{2+} anisotropy. The RHS of Fig. 3 shows the two localised systems that get mixed by double exchange.

To limit the number of free parameters, we chose to describe the Heisenberg exchange part of the model with two exchange couplings, $J^{d^n-d^n}$ and $J^{d^n-d^{n+1}}$, alongside the two distortion parameters δ_1/δ_2 instead of five independent exchange constants. The bonding of each Fe site to the μ_3-O, which constitutes the main exchange pathway, are only slightly different, which justifies this approach. Equal treatment of similar bonds, which would limit the number of Heisenberg parameters to two, is however not possible. Any model with equal treatment of the two bonds involving the always-Fe^{3+} site leads to a 50/50 distribution of the extra electron within the delocalised pair, which contradicts the 10 K crystal structure. Preferential occupation only emerges when the isosceles symmetry of the triangle is broken. In fact, small differences (1-2 %) between the couplings along these bonds leads to significant asymmetry of the electron distribution.

It is necessary to also add δ_2 in order to replicate the relative intensities of the INS peaks.

Certain relative intensities remain effectively constant in an isosceles model, while symmetry lowering has a profound impact on the intensities of the INS transitions. Since the distance between the two Fe sites within the delocalised pair is ≈ 0.1 Å shorter than the other Fe-Fe distances, there is solid physical reasoning behind adding this parameter.

We use our newly developed modelling tool to simulate the properties of the model in Fig. 3. Exact diagonalisation of the Hamiltonian (eq. (1)) yields the eigenvectors and eigenvalues from which we simulate the powder-averaged INS spectrum using a modified version of *mint*.[25] Based on those simulations, we fit the model to the experimentally determined excitation energies and INS intensities by minimising the χ^2 (see Methods for in-depth explanation of the fitting procedure). The red line in Fig. 2 (bottom) shows the best fit, which yielded the parameters $J^{d^n-d^n} = -7.76(3)$ meV, $J^{d^n-d^{n+1}} = -1.92(2)$ meV, $\delta_1 = -0.0128(5)$, $\delta_2 = 0.107(11)$, $|t| = 5.48(11)$ meV and $d_{\mathrm{Fe}^{2+}} = -0.480(7)$ meV. Fig. 4 shows the resulting energy level scheme.

The model excellently reproduces the excitation energies of I-IV and the relative intensities of III-V. It slightly overestimates the intensity of I, the ZFS excitation, which could mean two things: 1) That including only the anisotropy of Fe^{2+} is an over-simplification or 2) that we did not accurately subtract the phonon background, which has a pronounced energy dependence around $\hbar\omega = 1.42$ meV. Neither case is detrimental for the quality for the fit. Because of the large phonon contribution the the intensity of II, the model cannot replicate the intensity of that peak as discussed in the Methods section.

The Heisenberg exchange parameters are very similar to those in other iron carboxylate trimers, which clearly tells that the emergence of the low-energy spin excitations in **Fe_3-Piv** is a consequence of double exchange.[33,35] The parameters also align closely with what one would anticipate based on the crystal structure. δ_1, which governs the inequality of magnetic couplings along the two bonds with near-equal Fe-Fe distances, is less than 1.5 %, while the coupling along the unique bond is ≈11 % larger. Given the low value of δ_1, this parameter may seem redundant. However, the asymmetry it imposes is the lone origin of the electron

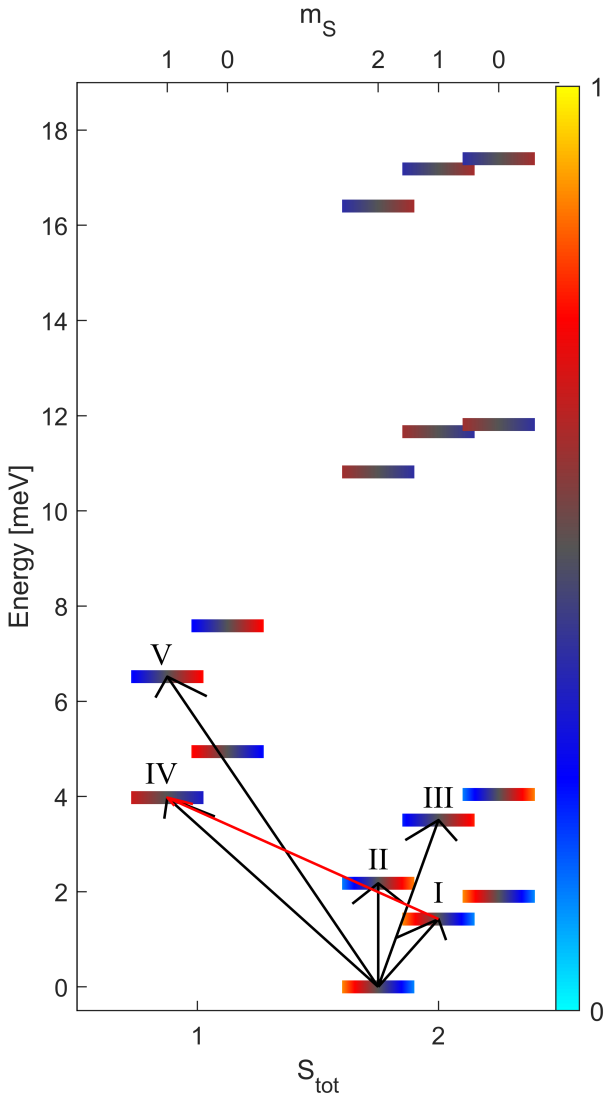

Fig. 4: Energy level scheme for **Fe_3-Piv** based on the best fit of the scalene triangle model (Fig. 3) to powder INS data. Black arrows mark the observed INS transitions from the ground state, and the red arrow marks the hot transition observed at $T = 25$ K using $E_i = 10$ meV. The colours mark the distribution of the extra electron within the delocalised pair for each state; left corresponds to site 1 and right to site 2. The ground state has preferential occupation of the site 1 with a ratio of 88 %/12 %.

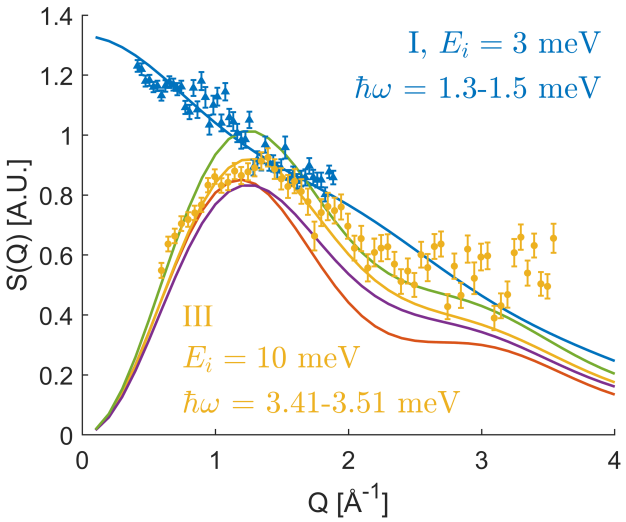

Fig. 5: Simulations of S(Q) for each INS transition (coloured lines) based on the best fit of the scalene model (Fig. 3) to powder INS data overlayed with the experimental Q-dependence of I (blue triangles) and III (yellow circles). The data is scaled to match the arbitraty intensity scale of the simulation.

distribution asymmetry that the 10 K crystal structure tells is necessary. The ground state electron distribution is asymmetric with 88 % occupation of the site 1, which agrees well with the $T = 10$ K crystal structure. In contrast, the mobile electron is predominantly located on site 2 in the first excited state ($E = 2.18$ meV), thus this excitation has a pronounced charge transfer nature. This agrees well with the predictions from Ref. 26, which gave an upper limit of 12.4 meV for the gap between these two minima of the potential energy surface.

Our modified version of *mint* can also simulate the intensity modulation of INS excitations as a function of Q; Fig. 5 shows the simulated Q-dependencies alongside the experimentally determined intensity modulations of I and III. These two are clearly different as expected for intra- and inter-multiplet transitions. The model excellently reproduces the Q-dependence of I and correctly determines the maximum at $Q \approx 1.25$ Å^{-1} for III, which confirms that the natures of the wave functions produced by the model are correct. At $Q > 2$ Å^{-1}, the agreement between simulation and data is worse due to incomplete subtraction of the phonon background in this region. The Q-dependencies of the remaining excitations can be found in the supporting information (Fig. S2).

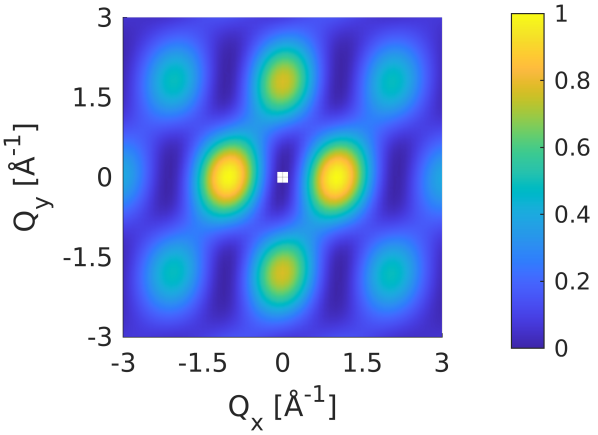

Fig. 6: Normalised $S(Q_x, Q_y)$ for the transition at 6.52 meV (excitation V) simulated based on the best fit of the scalene triangle model (Fig. 3) to powder INS data. The Fe-Fe bond within the delocalised pair lies along x.

In addition to the observables discussed so far, our model predicts the existence of additional excited $S = 2$ states around 12 and 17 meV; an energy region we were not able to probe with INS. The energies of the predicted states agree reasonably well with strong features at 12.0(2) and 16.2(2) meV in far infrared magneto-spectroscopy (FIRMS) measurement on **Fe$_3$-Piv** (Fig. S3). This gives us more confidence in our model and suggests that FIRMS can indeed provide information about molecular spin excitations as previously found for radical-bridged iron dimers.[54] However, further development of FIRMS simulations based on spin Hamiltonian models including vibronic coupling and intramolecular exchange is necessary to extract reliable quantitative information about the spin dynamics.

Simulations of Single-Crystal INS

While the intensity modulations along Q for the low-lying excited spin states are difficult to distinguish (see Fig. 4), the situation is entirely different for their 3D **Q**-dependencies. Our modified version of *mint* can also simulate these observables, which can be determined from INS experiments performed on large, oriented single crystals ($m \gtrsim 200$ mg). If the difficulties with acquiring crystals of this size can be overcome, such experiments have provided important information about magnetic molecules.[3,55,56]

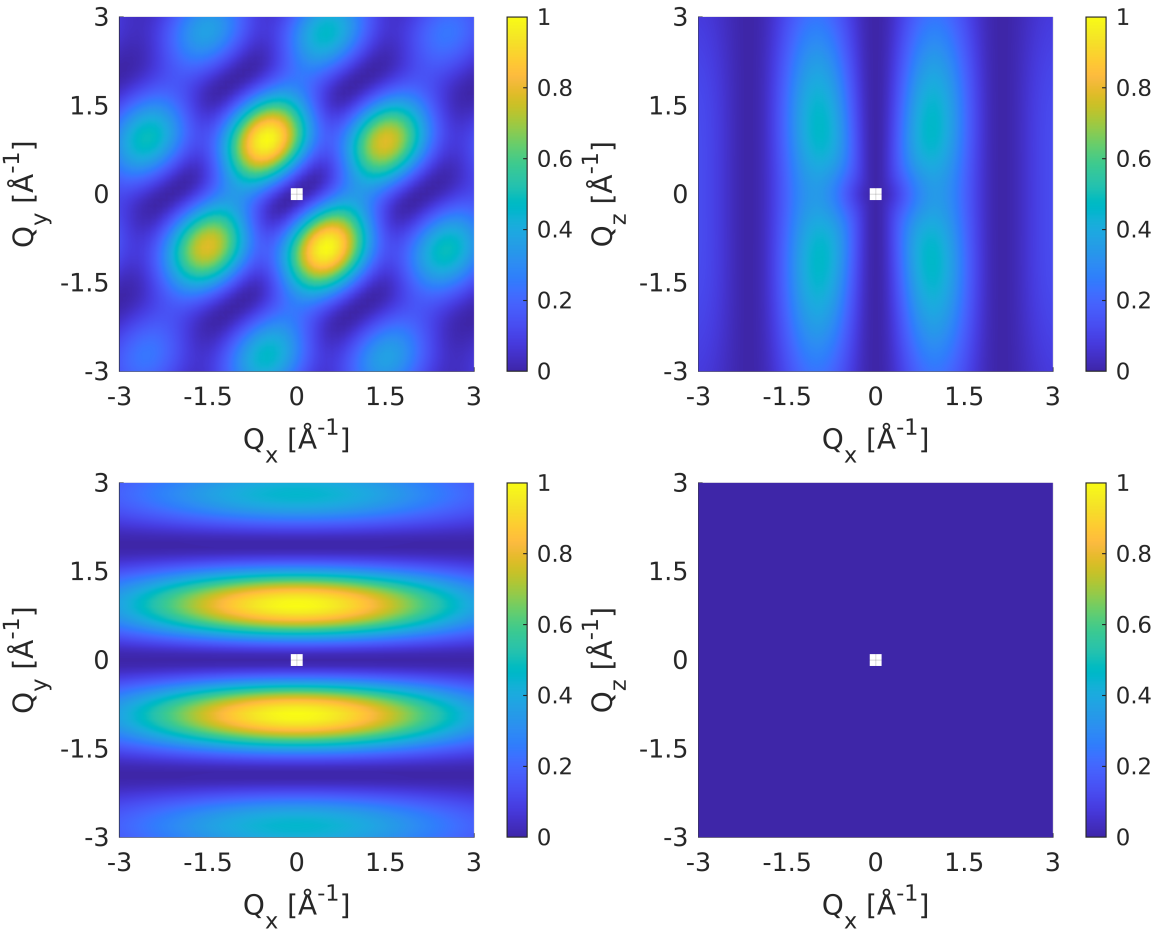

Fig. 7: Normalised **Q**-dependencies of excitation III simulated based on the best fit of the scalene (top row, see Fig. 3) and equilateral (bottom row) models to powder INS data. The Fe-Fe bond within the delocalised pair lies along x.

Our simulations show that this could also the case for **Fe_3-Piv** and systems governed by double exchange in general. Fig. 6 shows a simulation of the the intensity distribution of excitation V as function of Q_x and Q_y, the plane in which the Fe_3 triangle lies. Similar patterns did not emerge from simulations of trimer models without double exchange, which shows that this is a unique double exchange feature. Thus, experimental observation of a pattern similar to that in Fig. 6 would provide indisputable evidence for the presence of double exchange in a system. Similar patterns also emerge in equilateral double exchange models without preferential occupation.

Single-crystal INS would also be highly sensitive to preferential occupation of the delocalised electron according to our simulations. Fig. 7 shows a comparison between the simulated **Q**-dependencies of excitation III in the scalene model and a similar equilateral model with 50/50 electron distribution within the delocalised pair. Clearly, the preferential occupation in the scalene model has a profound impact on the **Q**-dependence. This shows that single-crystal INS has the possibility to quantify preferential occupation of delocalised electrons within mixed-valence molecules based on experimental evidence.

Conclusion and Outlook

This work showcases how INS can be used for investigating valence delocalised spin dynamics within magnetic molecules thanks to our newly developed modelling tool. We applied our approach to a proposed partially delocalised class II iron carboxylate trimer, **Fe_3-Piv**. Powder INS experiments showed that **Fe_3-Piv** has several low-lying excited spin states which can only be explained by including double exchange in a spin Hamiltonian model. From the relative intensities of the INS peaks, we were able to quantify the deviations from an equilateral model. This symmetry breaking causes significant preferential occupation of the delocalised electron within the ground state in agreement with crystallographic data. Our model furthermore shows that **Fe_3-Piv** has low-lying excited states with electron distribu-

tions opposite to that of the ground state, which gives rise to thermally activated electron transfer. Thereby, we firmly establish **Fe_3-Piv** as a Class II valence delocalised molecule.

The charge-transfer nature of the excitation to the first excited spin state (II, $\hbar\omega$=2.2101(6) meV) agrees well with the predictions from Ref. 26, where an upper limit of $\hbar\omega \leq 12.4$ meV is given for this excitation. The Lorentzian line shape of II and the pronounced temperature dependence of its FWHM suggest that a phonon-assisted process is responsible for the relaxation from this state exactly as expected for electron hopping in a class II valence delocalised molecule. On this basis, we propose that a full mapping of the T-dependence of this excitation's FWHM could shed light on the electron transfer process between the involved states.

Based on the obtained delocalised model for **Fe_3-Piv**, our simulations predict that certain double exchange excitations have unique **Q**-dependencies. Our model furthermore predicts that transitions involving states with preferential occupation have very distinct signatures in their **Q**-dependencies in comparison with completely delocalised models. This shows that single-crystal INS experiments, which directly measure the **Q**-dependencies of molecular spin excitations, could provide unambiguous evidence for molecular double exchange excitations and a method for quantifying the distribution of delocalised electrons within molecules. Such studies of **Fe_3-Piv** are currently on the way.

Finally, the differences between the magnetic properties of **Fe_3-Piv** and **Fe_3-OAc** highlights the potential for tuning the magnetic properties of larger valence delocalised molecules. A promising strategy could be to tailor vibronic coupling by carboxylate functionalisation analogously to how bridge substitution in dichalcogenide iron complexes controls the total spin of the ground state.[19] This shows that carboxylate trimers could be a good framework for realising molecular nanomagnets with useful properties and highlights the importance of our ongoing work of establishing a solid methodology for probing spin dynamics within valence delocalised molecules.

Acknowledgement

The authors thank Dr. Sarah Youngs, Operations Manager at the Deuteration Facility Laboratory at ISIS, for the synthesis of deuterated pivalic acid-D_9, Dr. Iñigo J. Vitórica-Yrezábal from the University of Manchester for solving the crystal structure of our sample of $Fe_3O(O_2CC(CD_3)_3)_6(C_5D_5N)_3$ from single-crystal X-ray diffraction data and Mr. Adam Brookfield for carrying out the bulk magnetometry measurements. We also thank ISIS for neutron beam time. RTC thanks the Institut Laue-Langevin for a PhD fellowship.

Author Contributions

RTC implemeted the double exchange model into code. CB performed the powder INS experiments with virtual participation of RTC, and RTC analysed the data supervised by JO. RTC simulated the INS experiments. GAT synthesised the **Fe_3-Piv** samples with support from REPW. RTC analysed the bulk magnetometry data with supervision from RC. FLM and RTC performed the FIRMS experiment supervised by MO and RTC analysed the data. RTC wrote the manuscript with input from MLB and JO. MLB supervised the project.

Methods

Sample

We synthesised $Fe_3O(O_2C(CH_3)_3)_6(C_5H_5N)_3$ (**Fe_3-Piv**) and its deuterated analogue in two steps. First, we made the (deuterated) pivalic acid adduct $Fe_3O(O_2C(CD_3)_3)_6(HO_2CC(CD_3)_3)_3$ (**A**), which we then recrystallised from (deuterated) pyridine (C_5H_5N) under a nitrogen atmosphere to give **Fe_3-Piv**. All reagents and solvents were from commercial sources and used without further purification except for deuterated pivalic acid-D_9 ($(CD_3)_3CCO_2H$), which was made at the ISIS Deuteration Facility. Other syntheses of **A** and **Fe_3-Piv** were previously reported.[26,40,57,58]

$\mathbf{Fe_3O(O_2C(CD_3)_3)_6(HO_2CC(CD_3)_3)_3}$ (A)

First, we mixed pivalic acid $(CD_3)_3CCO_2H$ (16.5 g, 148.4 mmol) and potassium hydroxide KOH (4.5 g, 80.2 mmol) in 50 ml deionised water in a nitrogen atmosphere and stirred it at $T = 30$ °C for ~ 30 min. Thereafter, we added iron(II) sulfate heptahydrate $FeSO_4 \cdot 7\,H_2O$ (10.0 g, 35.97 mmol) to the mixture and stirred for another 30 minutes. Afterwards and still in a nitrogen atmosphere, we added 50 ml of diethyl ether and stirred the mixture vigorously for another ~ 30 minutes. We then extracted the product on air by first separating the water from the dark brown diethyl ether layer using a funnel-separator and subsequently quickly filtrating the dark brown liquid using a filter paper. We then diluted the dark filtrate with 10 ml of deoxygenated acetonitrile and removed the diethyl ether under reduced pressure. We filtered the obtained product (black-brown crystals) once more, washed it with deoxygenated acetonitrile (3x 10 ml) and dried it in a stream of nitrogen. Yield: 3.85 g. Anal. Calc. for $C_{45}H_3D_{81}O_{19}Fe_3$: C, 45.87; Fe, 14.22. Found: C, 46.54; Fe, 14.43.

$\mathbf{Fe_3O(O_2C(CH_3)_3)_6(C_5H_5N)_3}$ ($\mathbf{Fe_3}$-Piv)

In a nitrogen atmosphere, we stirred compound **A** into a mixture of 10 ml diethyl ether and 6 ml (74.88 mmol) (deuterated) pyridine (C_5H_5N) for ~ 15 min at room temperature. Then, we removed the diethyl ether by distillation in a stream of nitrogen. We kept the obtained pyridine solution at $T = 100$ °C for another ~ 15 min and then left it to cool slowly to room temperature. The next day, we collected the precipitated crystals (including ones suitable for single-crystal X-ray diffraction) by filtration, washed them with a small quantity of cooled deoxygenated acetonitrile (~ 20 ml), and dried them at room temperature in a stream of nitrogen. Yield: 3.03 g (90 %). Anal. Calc. for $C_{45}D_{69}N_3O_{19}Fe_3$: C, 49.27; N, 3.83; Fe, 15.27. Found: C, 49.71; N, 3.99; Fe, 15.57.

The synthesis utilises that the oxidising process of iron(II) carboxylates to fully oxidised iron(III) carboxylates proceeds in steps. In each step, the ratio of Fe^{2+} to Fe^{3+} differs, and so does their solubility compared to that of the initial iron(II) and iron(III) analogues. This

methodology was the first, largely used by Gerbeleu et al., for synthesising complexes with a $2\,Fe_2^{3+}Fe^{2+}O$ core with other aliphatic carboxylic acids besides the acetate anion.[59]

Single crystal X-ray diffraction was used to determine the crystal structure of the obtained sample of **Fe_3-Piv**, which was found to be isostructural to the crystals reported in Ref. 26. Diffraction data were collected on a Rikagu XtaLAB AFC11 (RINC): quarter-chi single diffractometer at $T = 100$ K using Cu Kα radiation with $\lambda = 1.552$ Å doing ω scans. The structure was solved with SHELXT[60] and refined with SHELXL[61] both within OLEX2.[62] An absorption correction was performed with CrysAlisPro,[63] and the structure was checked with CheckCIF (https://checkcif.iucr.org).

Magnetometry

Variable-field (VF) and variable-temperature (VT) direct current magnetisation were measured using a Quantum Design MPMS®3 SQUID magnetometer. Ca. 10 mg of **Fe_3-Piv** (powder form) was mixed with eicosane and mounted in a gelatin capsule. VT measurements were performed from $T = 2$-300 K in $B = 500$ Oe applied field, and VF measurements were performed from $B = 0$-7 T at $T = 2$ K and 5 K. The temperature dependence of the magnetic susceptibility, $\chi(T)$, was obtained from VT data using the linear medium approximation $\chi(T) = M(T)/B$, where $M(T)$ is the temperature-dependent magnetisation. The diamagnetism of the eicosane was subsequently subtracted, and the diamagnetism of the constituents of **Fe_3-Piv** was corrected for using Pascal's constants.[64]

Inelastic Neutron Scattering

The powder INS experiment was performed with the time-of-flight spectrometer LET at the ISIS Pulsed Neutron and Muon Source at the STFC Rutherford Appleton Laboratory, UK.[65] We used approximately one gram of polycrystalline **Fe_3-Piv** packed in a hollow cylinder geometry in an aluminium sample holder to prevent multiple scattering. LET was run in replication rate multiplication (RRM) mode with the RRM chopper spinning at 140 Hz

leading to simultaneous measurements with $E_i = 2.95$ meV, 4.96 meV, 10.01 meV and 29.81 meV. Data was collected at $T = 1.55$ K for 5 hours, 5 K for 5 hours and at 25 K for 2 hours. We used MANTID to reduce and analyse the data.[66,67]

For $E_i = 3$ meV, the background contribution is negligible and we do not correct for it. For $S(E)$ measured with $E_i = 10$ meV, we account for the phonon background contribution by fitting a cubic spline alongside the Gaussian and Lorentzian peak shapes. In Fig. 2, this background contribution has been subtracted. For $S(Q)$ data measured with $E_i \geq 5$ meV, we estimate the phonon contribution to a particular peak by integrating over a narrow energy transfer region in the vicinity of the magnetic excitation.

When fitting the scalene triangle model (Fig. 3) we determine the level of agreement between the experimental and simulated peak positions and intensities with a χ^2 method, and fit the model to data by minimising the χ^2. We exclude the intensity of excitation II from the evaluation of the χ^2 since a phonon background contributes significantly to its integrated intensity, a feature our modelling tool cannot capture. To force our algorithm to fit the relative intensities more accurately, we introduced a weighting of the different contributions to the χ^2 as $\chi^2_{\text{tot}} = p\chi^2_{\hbar\omega} + (1-p)\chi^2_{\text{ints}}$; $p = 0.1$ provided a good trade-off between accurately reproducing both peak positions and intensities.

We estimate the parameter errors based on the parameter variations that induce unambiguously worse visual agreement between the simulation and the powder INS data. Due to large systematic errors, such as phonon contributions to the relative intensities of magnetic peaks, statistical error estimation overestimates the precision of the parameter estimates from the fitted model by two orders of magnitude.

Supporting Information Available

CIF files will be shared upon request via email to the corresponding author.

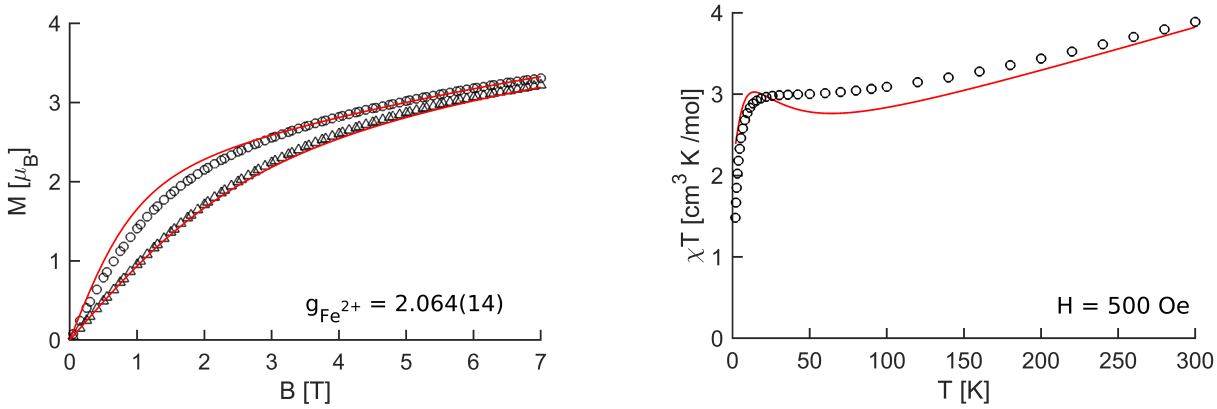

Fig. S1: **Left**: Iso-thermal field-dependent magnetisation of **Fe_3-Piv** at $T = 2$ K (black circles) and 5 K (black triangles). The red lines are fits of the scalene triangle model from the main text with $g_{Fe^{2+}}$ as the only free parameter and a fixed $g_{Fe^{3+}} = 2$. **Right**: Temperature-dependence of the magnetic susceptibility of **Fe_3-Piv** (black circles) overplotted with a simulation (red line) of the scalene model from the main text with the g-values from the fit of $M(H)$.

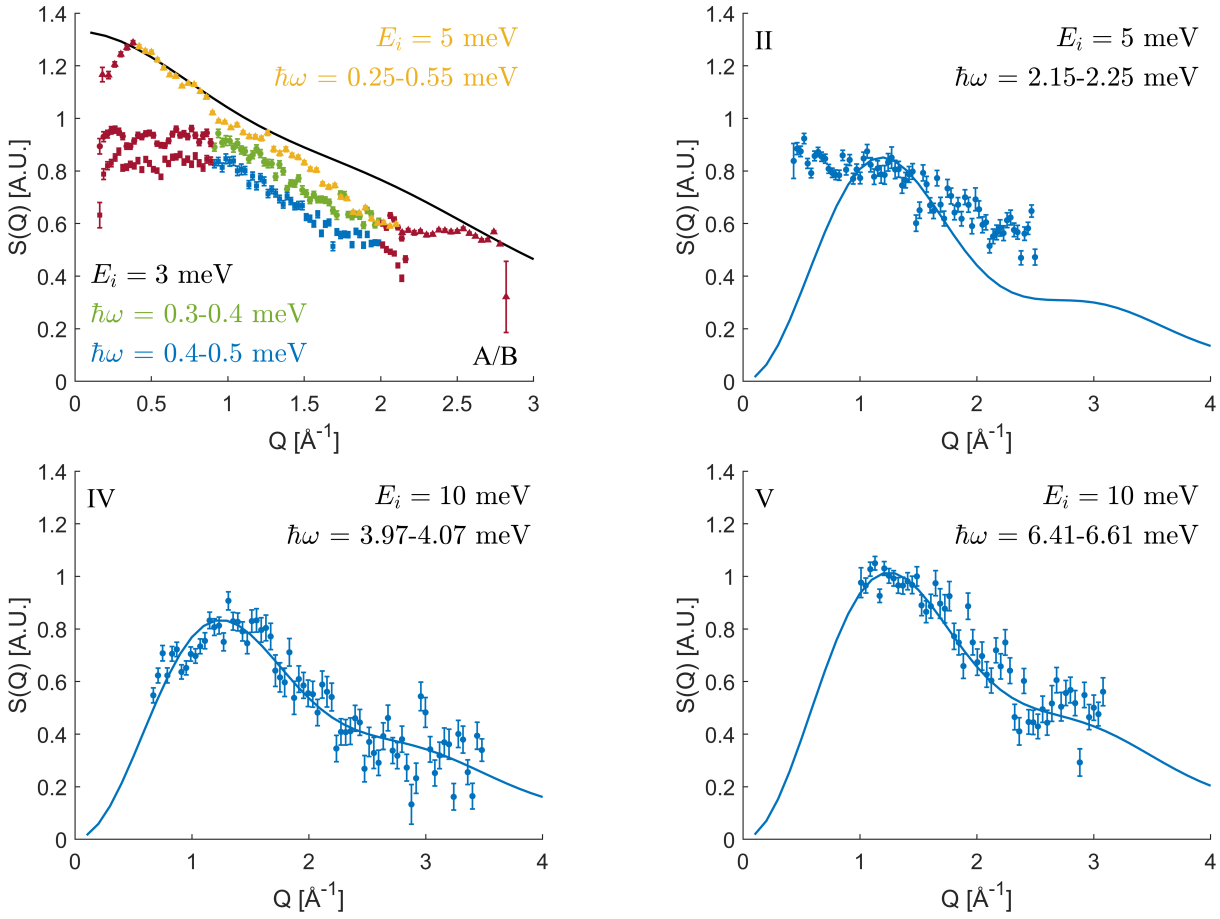

Fig. S2: S(Q) for INS excitations A/B, II, IV, and V with E_i's and exact integration ranges are written on the plots. For II, IV, and V, the lines depict simulations of their Q-dependencies based on the best fit of scalene triangle model (Fig. 3) to INS peak position and intensities. For A/B, the line depicts the Q-dependence of I, the ZFS excitation, and the red data points mark regions with significant experimental artefacts. The data is scaled to match the intensity scale of the simulations.

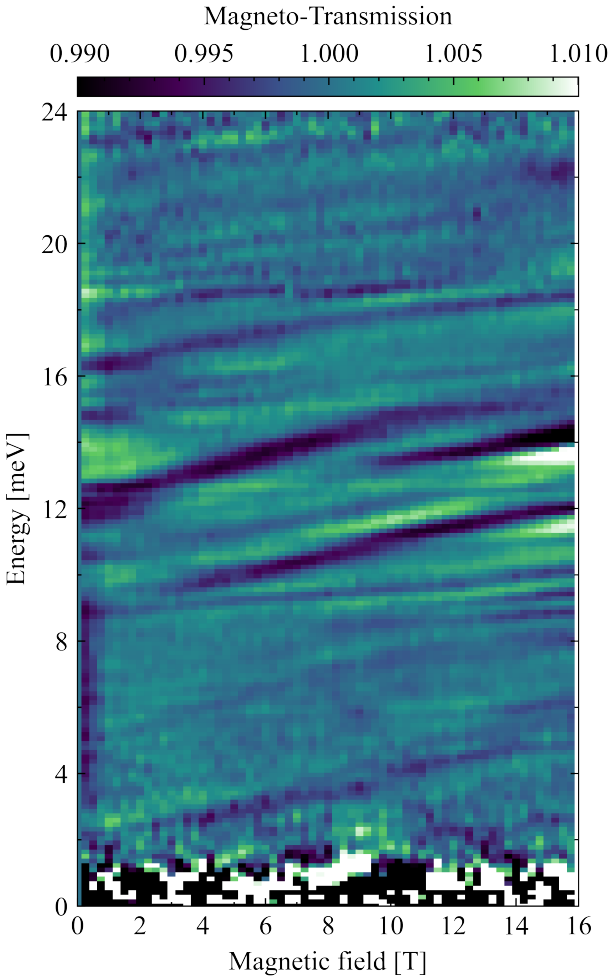

Fig. S3: Derivative of IR magneto-transmission through polycrystalline **Fe_3-Piv** suspended in eicosane as a function of applied magnetic field. Fourier transform IR spectra are measured at $T = 4.2K$ between 0 and 16 T in steps of 0.25 T. The derivative of a spectrum measured at $B = B'$ is normalised to average of derivatives of spectra measured at $B' \pm 3.75$ T.

References

(1) Sessoli, R.; Gatteschi, D.; Caneschi, A.; Novak, M. Magnetic bistability in a metal-ion cluster. *Nature* **1993**, *365*, 141–143.

(2) Thomas, L.; Lionti, F.; Ballou, R.; Gatteschi, D.; Sessoli, R.; Barbara, B. Macroscopic quantum tunnelling of magnetization in a single crystal of nanomagnets. *Nature* **1996**, *383*, 145–147.

(3) Baker, M. L.; Guidi, T.; Carretta, S.; Ollivier, J.; Mutka, H.; Güdel, H. U.; Timco, G. A.; McInnes, E. J. L.; Amoretti, G.; Winpenny, R. E. P.; Santini, P. Spin dynamics of molecular nanomagnets unravelled at atomic scale by four-dimensional inelastic neutron scattering. *Nat. Phys.* **2012**, *8*, 906–911.

(4) Hill, S.; Edwards, R. S.; Aliaga-Alcalde, N.; Christou, G. Quantum Coherence in an Exchange-Coupled Dimer of Single-Molecule Magnets. *Science* **2003**, *302*, 1015–1018.

(5) Ardavan, A.; Rival, O.; Morton, J. J. L.; Blundell, S. J.; Tyryshkin, A. M.; Timco, G. A.; Winpenny, R. E. P. Will Spin-Relaxation Times in Molecular Magnets Permit Quantum Information Processing? *Phys. Rev. Lett.* **2007**, *98*, 057201.

(6) Perlepe, P. et al. Metal-Organic Magnets with Large Coercivity and Ordering Temperatures up to 242 °C. *Science* **2020**, *370*, 587–592.

(7) Gould, C. A.; McClain, K. R.; Reta, D.; Kragskow, J. G. C.; Marchiori, D. A.; Lachman, E.; Choi, E.-S.; Analytis, J. G.; Britt, R. D.; Chilton, N. F.; Harvey, B. G.; Long, J. R. Ultrahard Magnetism from Mixed-Valence Dilanthanide Complexes with Metal-Metal Bonding. *Science* **2022**, *375*, 198–202.

(8) Wedge, C. J.; Timco, G. A.; Spielberg, E. T.; George, R. E.; Tuna, F.; Rigby, S.; McInnes, E. J. L.; Winpenny, R. E. P.; Blundell, S. J.; Ardavan, A. Chemical Engineering of Molecular Qubits. *Phys. Rev. Lett.* **2012**, *108*, 107204.

(9) Shiddiq, M.; Komijani, D.; Duan, Y.; Gaita-Arino, A.; Coronado, E.; Hill, S. Enhancing coherence in molecular spin qubits via atomic clock transitions. *Nature* **2016**, *531*, 348–351.

(10) Chicco, S.; Allodi, G.; Chiesa, A.; Garlatti, E.; Buch, C. D.; Santini, P.; De Renzi, R.; Piligkos, S.; Carretta, S. Proof-of-Concept Quantum Simulator Based on Molecular Spin Qudits. *JACS* **2024**, *146*, 1053–1061.

(11) Miyamachi, T.; Gruber, M.; Davesne, V.; Bowen, M.; Boukari, S.; Joly, L.; Scheurer, F.; Rogez, G.; Yamada, T. K.; Ohresser, P.; Beaurepaire, E.; Wulfhekel, W. Robust spin crossover and memristance across a single molecule. *Nat. Commun.* **2012**, *3*, 938.

(12) Guo, F.-S.; Day, B. M.; Chen, Y.-C.; Tong, M.-L.; Mansikkamäki, A.; Layfield, R. A. Magnetic Hysteresis up to 80 Kelvin in a Dysprosium Metallocene Single-Molecule Magnet. *Science* **2018**, *362*, 1400–1403.

(13) Sanvito, S. Molecular Spintronics. *Chem. Soc. Rev.* **2011**, *40*, 3336–3355.

(14) Baumann, S.; Paul, W.; Choi, T.; Lutz, C. P.; Ardavan, A.; Heinrich, A. J. Electron paramagnetic resonance of individual atoms on a surface. *Science* **2015**, *350*, 417–420.

(15) Robert, J.; Parizel, N.; Turek, P.; Boudalis, A. K. Polyanisotropic Magnetoelectric Coupling in an Electrically Controlled Molecular Spin Qubit. *JACS* **2019**, *141*, 19765–19775.

(16) Zener, C. Interaction between the *d*-Shells in the Transition Metals. II. Ferromagnetic Compounds of Manganese with Perovskite Structure. *Phys. Rev.* **1951**, *82*, 403–405.

(17) Anderson, P. W.; Hasegawa, H. Considerations on Double Exchange. *Phys. Rev.* **1955**, *100*, 675–681.

(18) Blondin, G.; Girerd, J. J. Interplay of electron exchange and electron transfer in metal polynuclear complexes in proteins or chemical models. *Chem. Rev.* **1990**, *90*, 1359–1376.

(19) Henthorn, J.; Cutsail, G.; Weyhermüller, T.; DeBeer, S. Stabilization of intermediate spin states in mixed-valent diiron dichalcogenide complexes. *Nat. Chem.* **2022**, *14*, 328–333.

(20) Palii, A.; Aldoshin, S.; Tsukerblat, B. Mixed-valence clusters: Prospects for single-molecule magnetoelectrics. *Coord. Chem. Rev.* **2021**, *426*, 213555.

(21) Bosch-Serrano, C.; Clemente-Juan, J. M.; Coronado, E.; Gaita-Ariño, A.; Palii, A.; Tsukerblat, B. Electric Field Control of the Spin State in Mixed-Valence Magnetic Molecules. *ChemPhysChem* **2012**, *13*, 2662–2665.

(22) Solomon, E. I.; Xie, X.; Dey, A. Mixed valent sites in biological electron transfer. *Chem. Soc. Rev.* **2008**, *37*, 623–638.

(23) Borrás-Almenar, J. J.; Clemente, J. M.; Coronado, E.; Palii, A. V.; Tsukerblat, B. S.; Georges, R. High-nuclearity mixed-valence magnetic clusters: A general solution of the double exchange problem. *J. Chem. Phys.* **1996**, *105*, 6892–6909.

(24) Stoll, S.; Schweiger, A. EasySpin, a comprehensive software package for spectral simulation and analysis in EPR. *J. Magn. Reson.* **2006**, *178*, 42–55.

(25) Baker, M. L. *mint*: Simulation of Inelastic Neutron Scattering Induced Magnetic Excitations for Single-Ions & Finite Exchange Coupled Spin-systems. 2022; https://mlbakerlab.co.uk/mint.

(26) Wilson, C.; Iversen, B. B.; Overgaard, J.; Larsen, F. K.; Wu, G.; Palii, S. P.; Timco, G. A.; Gerbeleu, N. V. Multi-Temperature Crystallographic Studies of Mixed-Valence Polynuclear Complexes; Valence Trapping Process in the Trinuclear Oxo-Bridged Iron Compound, $[Fe_3O(O_2CC(CH_3)_3)_6(C_5H_5N)_3]$. *JACS* **2000**, *122*, 11370–11379.

(27) Overgaard, J.; Larsen, F. K.; Schiøtt, B.; Iversen, B. B. Electron Density Distributions of Redox Active Mixed Valence Carboxylate Bridged Trinuclear Iron Complexes. *JACS* **2003**, *125*, 11088–11099.

(28) Momma, K.; Izumi, F. *VESTA3* for three-dimensional visualization of crystal, volumetric and morphology data. *J. Appl. Crystallogr.* **2011**, *44*, 1272–1276.

(29) Wu, G.; Zhang, Y.; Ribaud, L.; Coppens, P.; Wilson, C.; Iversen, B. B.; Larsen, F. K. Multitemperature Resonance-Diffraction and Structural Study of the Mixed-Valence Complex $[Fe_3O(OOCC(CH_3)_3)_6(C_5H_5N)_3]$. *Inorg. Chem.* **1998**, *37*, 6078–6083.

(30) Sowrey, F. E.; MacDonald, C. J.; Cannon, R. D. NMR study of electron transfer between paramagnetic complexes Kinetics of the self-exchange reaction $[Fe_3O(O_2CCMe_3)_6(py)_3]^{+/0}$ (py = pyridine). *J. Chem. Soc., Faraday Trans.* **1998**, *94*, 1571–1574.

(31) Scheins, S.; Overgaard, J.; Timco, G. A.; Stash, A.; Chen, Y.-S.; Larsen, F. K.; Christensen, M.; Jørgensen, M. R. V.; Madsen, S. R.; Schmøkel, M. S.; Iversen, B. B. Pressure versus Temperature Effects on Intramolecular Electron Transfer in Mixed-Valence Complexes. *Chem. - Eur. J.* **2013**, *19*, 195–205.

(32) Cannon, R. D.; White, R. P. Chemical and Physical Properties of Triangular Bridged Metal Complexes. *Prog. Inorg. Chem.* **1988**, *36*, 195–298.

(33) White, R.; Al-Basseet, J.; Cannon, R.; Kearley, G.; Jayasooriya, U. Temperature dependent magnetic exchange interactions in a mixed-valence complex: A neutron scattering study. *Phys. B: Condens.* **1989**, *156-157*, 367–369.

(34) Jayasooriya, U. A.; Cannon, R. D.; Anson, C. E.; arapKoske, S. K.; White, R. P.; Kearley, G. J. Intermolecular magnetic interactions in a mixed-valence compound: inelastic neutron scattering spectrum of $[Fe_2FeO(O_2CCD_3)_6(C_5D_5N)_3](C_5D_5N)$. *J. Chem. Soc., Chem. Commun.* **1992**, 379–381.

(35) White, R. P.; Stride, J. A.; Bollen, S. K.; Sa-Ard, N. C.; Kearley, G. J.; Jayasooriya, U. A.; Cannon, R. D. Electronic interactions in mixed-valence and mixed-metal ion clusters: inelastic neutron scattering spectra of the complexes $[Fe_2^{III}M^{II}O(OOCMe)_6(py)_3](py)$, where M = manganese, nickel. *JACS* **1993**, *115*, 7778–7782.

(36) Cannon, R. D.; Jayasooriya, U. A.; White, R. P.; ArapKoske, S. K. New electronic transitions observed in the trinuclear iron (III,III,II) cluster, by inelastic neutron scattering. *Spectrochim. Acta - A: Mol. Biomol.* **1993**, *49*, 1787–1791.

(37) Cannon, R. D.; Jayasooriya, U. A.; Wu, R.; arapKoske, S. K.; Stride, J. A.; Nielsen, O. F.; White, R. P.; Kearley, G. J.; Summerfield, D. Spin Frustration in High-Spin Triiron(III) Complexes: An Inelastic Neutron Scattering Study. *JACS* **1994**, *116*, 11869–11874.

(38) White, R.; Wilson, L.; Williamson, D.; Moore, G.; Jayasooriya, U.; Cannon, R. Electron transfer in a triangular $Fe_2^{III}Fe^{II}$ cluster: Evidence of valence localization in solution. *Spectrochim. Acta - A: Mol. Biomol.* **1990**, *46*, 917–920.

(39) Wu, R.; Koske, S. K. A.; White, R. P.; Anson, C. E.; Jayasooriya, U. A.; Cannon, R. D. Electron transfer rates in a trinuclear mixed-valence iron(III, III, II) molecule: A variable-temperature infrared spectroscopic study. *J. Chem. Soc., Chem. Commun.* **1994**, 1657–1658.

(40) Wu, R.; Poyraz, M.; Sowrey, F. E.; Anson, C. E.; Wocadlo, S.; Powell, A. K.; Jayasooriya, U. A.; Cannon, R. D.; Nakamoto, T.; Katada, M.; Sano, H. Electron Localization and Delocalization in Mixed-Valence Transition Metal Clusters: Structural and Spectroscopic Studies of Oxo-Centered Trinuclear Complexes $[Fe_3O(OOCCMe_3)_6(py)_3]^{+/0}$ and $[Mn_3O(OOCCMe_3)_6(py)_3]^{+/0}$. *Inorg. Chem.* **1998**, *37*, 1913–1921.

(41) Robin, M. B.; Day, P. Mixed Valence Chemistry - A Survey and Classification. *Adv. Inorg. Chem. Radiochem.* **1968**, *10*, 247–422.

(42) Demadis, K. D.; Hartshorn, C. M.; Meyer, T. J. The Localized-to-Delocalized Transition in Mixed-Valence Chemistry. *Chem. Rev.* **2001**, *101*, 2655–2686.

(43) Borshch, S. A.; Bominaar, E. L.; Blondin, G.; Girerd, J. J. Double exchange and vibronic coupling in mixed valence systems. Origin of the broken-symmetry ground state of $[Fe_3S_4]^0$ cores in proteins and models. *JACS* **1993**, *115*, 5155–5168.

(44) Palii, A.; Tsukerblat, B. Pair-delocalization in trigonal mixed-valence clusters: New insight into the vibronic origin of broken-symmetry ground states. *Phys. Chem. Chem. Phys.* **2019**, *21*, 11122–11131.

(45) Wu, R.; Jayasooriya, U. A.; Cannon, R. D. Vibrational coupling in oxo-centred trinuclear clusters: Oxygen-16/18 isotopic substitution studies of $[Fe_3^{III}O(O_2CC(CH_3)_3)_6(py)_3][FeCl_4]$ and $[Fe_2^{III}Fe^{II}O(O_2CC(CH_3)_3)_6(py)_3]$. *Spectrochim. Acta - A: Mol. Biomol.* **2000**, *56*, 575–579.

(46) Baker, M. L.; Blundell, S. J.; Domingo, N.; Hill, S. In *Molecular Nanomagnets and Related Phenomena*; Gao, S., Ed.; Springer Berlin Heidelberg: Berlin, Heidelberg, 2015; pp 231–291.

(47) Kofu, M.; Yamamuro, O.; Kajiwara, T.; Yoshimura, Y.; Nakano, M.; Nakajima, K.; Ohira-Kawamura, S.; Kikuchi, T.; Inamura, Y. Hyperfine structure of magnetic excitations in a Tb-based single-molecule magnet studied by high-resolution neutron spectroscopy. *Phys. Rev. B* **2013**, *88*, 064405.

(48) Rauch, H.; Waschkowski, W. In *Neutron Data Booklet*; Dianoux, A.-J., Lander, G., Eds.; OCP Science, 2003; pp 1.1–1,1.1–17.

(49) Lovesey, S. W.; Staub, U. Magnetoelastic model for the relaxation of lanthanide ions in $YBa_2Cu_3O_{7-\delta}$ observed by neutron scattering. *Phys. Rev. B* **2000**, *61*, 9130–9139.

(50) Dunstan, M. A.; Giansiracusa, M. J.; Vonci, M.; Calvello, S.; Yu, D.; Soncini, A.; Boskovic, C.; Mole, R. A. Direct observation of magnetoelastic coupling in a molecular spin qubit: New insights from crystal field neutron scattering data. *Chem. Sci.* **2023**, *14*, 3990–4001.

(51) Cannon, R. D.; Montri, L.; Brown, D. B.; Marshall, K. M.; Elliott, C. M. Partial electron delocalization in a mixed-valence trinuclear iron(III)-iron(II) complex. *JACS* **1984**, *106*, 2591–2594.

(52) Woehler, S. E.; Wittebort, R. J.; Oh, S. M.; Kambara, T.; Hendrickson, D. N.; Inniss, D.; Strouse, C. E. Deuteron NMR study of lattice dynamics affecting the rate of intramolecular electron transfer in the iron acetato oxo pyridine mixed-valence complex $[Fe_3O(O_2CCH_3)_6(py)_3](py)$. *JACS* **1987**, *109*, 1063–1072.

(53) Borrás-Almenar, J. J.; Cardona-Serra, S.; Clemente-Juan, J. M.; Coronado, E.; Palii, A. V.; Tsukerblat, B. MVPACK: A package to calculate energy levels and magnetic properties of high nuclearity mixed valence clusters. *J. Comput. Chem.* **2010**, *31*, 1321–1332.

(54) Christiansen, R. T. *Double Exchange Spin Dynamics within Valence Delocalised Molecular Magnets*; University of Manchester, 2024; Chapter 3.

(55) Carretta, S.; Santini, P.; Amoretti, G.; Guidi, T.; Copley, J. R. D.; Qiu, Y.; Caciuffo, R.; Timco, G.; Winpenny, R. E. P. Quantum Oscillations of the Total Spin in a Heterometallic Antiferromagnetic Ring: Evidence from Neutron Spectroscopy. *Phys. Rev. Lett.* **2007**, *98*, 167401.

(56) Garlatti, E.; Guidi, T.; Ansbro, S.; Santini, P.; Amoretti, G.; Ollivier, J.; Mutka, H.; Timco, G.; Vitorica-Yrezabal, I. J.; Whitehead, G. F. S.; Winpenny, R. E. P.; Car-

retta, S. Portraying entanglement between molecular qubits with four-dimensional inelastic neutron scattering. *Nat. Commun.* **2017**, *8*, 14543.

(57) Gerbeleu, N.; Timko, G.; Turte, K.; Popovich, G.; Bobkova, S.; Indrichan, K. Synthesis and investigation of mixed valence (II,III,III) iron μ-3-oxocarboxylates. *Zh. Neorg. Khim.* **1986**, *31*, 684–690.

(58) Asamaki, K.; Nakamoto, T.; Kawata, S.; Sano, H.; Katada, M.; Endo, K. Structure and mixed-valence states of the trinuclear iron(II,III,III) pivalate complex-pivalic acid adduct, $[Fe_3O(O_2CCMe_3)_6(Me_3CCO_2H)_3]$ ($Me = -CH_3$). *Inorganica Chim. Acta* **1995**, *236*, 155–161.

(59) Overgaard, J.; Rentschler, E.; Timco, G. A.; Gerbeleu, N. V.; Arion, V.; Bousseksou, A.; Tuchagues, J. P.; Larsen, F. K. Multi-temperature X-ray diffraction, Mössbauer spectroscopy and magnetic susceptibility studies of a solvated mixed-valence trinuclear iron formate, $[Fe_3O(HCO_2)_6(NC_5H_4CH_3)_3] \cdot 1.3\,(NC_5H_4CH_3)$. *J. Chem. Soc., Dalton Trans.* **2002**, 2981–2986.

(60) Sheldrick, G. M. *SHELXT* – Integrated space-group and crystal-structure determination. *Acta Crystallogr. Sec. A* **2015**, *71*, 3–8.

(61) Sheldrick, G. M. Crystal structure refinement with *SHELXL*. *Acta Crystallogr. Sec. C* **2015**, *71*, 3–8.

(62) Dolomanov, O. V.; Bourhis, L. J.; Gildea, R. J.; Howard, J. A. K.; Puschmann, H. *OLEX2*: A complete structure solution, refinement and analysis program. *J. Appl. Crystallogr.* **2009**, *42*, 339–341.

(63) Rigaku Oxford Diffraction CrysAlisPro Software system, version 1.171.42.64a. 2022.

(64) Bain, G. A.; Berry, J. F. Diamagnetic Corrections and Pascal's Constants. *J. Chem. Educ.* **2008**, *85*, 532.

(65) Bewley, R.; Taylor, J.; Bennington., S. LET, a cold neutron multi-disk chopper spectrometer at ISIS. *Nucl. Instrum. Methods Phys. Res. A: Accel. Spectrom. Detect. Assoc. Equip.* **2011**, *637*, 128–134.

(66) Arnold, O. et al. Mantid—Data analysis and visualization package for neutron scattering and μSR experiments. *Nucl. Instrum. Methods Phys. Res. A: Accel. Spectrom. Detect. Assoc. Equip.* **2014**, *764*, 156 – 166.

(67) Mantid: Manipulation and Analysis Toolkit for Instrument Data.; Mantid Project. 2013; http://dx.doi.org/10.5286/SOFTWARE/MANTID6.4.

Chapter 5

Manuscript 3: Spin Dynamics of a Molecular Nanomagnet with two Valence Electrons Delocalised Across Six Sites

5.1 Prelude to Chapter

The research presented in this paper draft sought to investigate the elusive spin dynamics of the nanosized complex $[Fe(Tp)(CN)_3]_8[Fe(H_2O)(DMSO)]_6$ (Fe_{14}, Tp^-=hydrotris(pyrazolyl)borate; DMSO=dimethyl sulfoxide) [31]. Within this unique molecule, two electrons undergo thermally activated transfer between six formally high-spin Fe^{3+} sites. It provides a rare possibility for probing the effects of electron delocalisation across multiple sites, which is crucial for the fundamental understanding of valence delocalisation. It furthermore provides a platform for investigating the influence of Coulomb repulsion between two delocalised electrons, which had a larger influence on the spin dynamics than anticipated.

Experiments using IN5@ILL provided high-quality INS data that revealed several low-lying ($\hbar\omega < 1$ meV) spin excitations for which we could also probe the momentum transfers. Because of the increased intrinsic complexity of Fe_{14} compared to **Fe_3-Piv** from Chapter 4, the modelling had to be performed with MVPACK instead of the modelling tool developed during this thesis (see section 2.2). Therefore, we could not simulate the INS spectra of the employed model. Instead, we had to rely on comparison of experimentally observed excitation energies with Hamiltonian eigenvalues, as well as qualitative arguments, to assess the agreement between model and data. In the future, we would like to expand our analysis to also include INS simulations. We are currently in contact with the developers of MVPACK discussing a possible collaboration.

We intend to submit this draft to a physics journal. Contribtuions: R. T. Christiansen treated the raw INS data, analysed it, performed the modelling and wrote the manuscript. Dr M. S. Huzan, Dr M. L. Baker, and Dr J. Ollivier performed the INS measurements with preliminary measurements by Dr T. Guidi. Dr S.-Q. Wu and Prof. O. Sato provided the samples. Dr J. Ollivier and Dr M. L. Baker supervised the project.

Spin Dynamics of a Molecular Nanomagnet with two Valence Electrons Delocalised Across Six Sites

R. T. Christiansen,[1,2,3] M. S. Huzan,[2,3] S.-Q. Wu,[4] O. Sato,[4] T. Guidi,[5] J. Ollivier,[1] and M. L. Baker[2,3,*]

[1] *Spectroscopy Group, Institut Laue-Langevin, 38042 Grenoble Cedex 9, France*
[2] *Department of Chemistry, the University of Manchester, Manchester M13 9PL, UK*
[3] *The University of Manchester at Harwell, Diamond Light Source, Didcot OX11 0DE, UK*
[4] *Institute for Materials Chemistry and Engineering, Department of Fundamental Organic Chemistry, Kyushu University, Fukuoka 819-0395, Japan*
[5] *ISIS Facility, STFC Rutherford-Appleton Laboratory, Didcot OX11 0QX, UK*

(Dated: April 17, 2024)

Quantitative information about valence delocalised electrons within molecules remains elusive despite the ubiquity of the mechanism in biological systems and the promising utility of valence delocalised molecules in quantum materials. The problem is especially challenging when more than one electron becomes delocalised. We present inelastic neutron scattering (INS) studies of Fe_{14}, a proposed partially delocalised molecule in which two electrons undergo thermally activated electron transfer between six high-spin Fe^{3+} ions. We identify four low-lying magnetic levels which can be reproduced by a spin Hamiltonian model incorporating double exchange, Heisenberg exchange, and Coulomb repulsion. Our best fit shows that ferromagnetic Heisenberg exchange overcomes antiferromagnetic double exchange to arrive at the $S = 14$ ground state. We also extract the distribution of the delocalised electrons for each eigenstate based on the spin Hamiltonian model, which confirms the partially delocalised nature of Fe_{14}. Also, the electron distributions can be correlated to the momentum transfer dependencies of the excitations probed by INS.

I. INTRODUCTION

Magnetic molecules can host various fundamental quantum phenomena such as magnetic bistability, quantum tunnelling and coherence of quantum superpositions [1–5]. Today, significant effort is being put into engineering molecule-based materials that harness these phenomena for various applications, for example high-density information storage, spintronics, quantum information processing and quantum sensing [6–14]. Therefore, it is crucially important to improve fundamental understanding of molecular spin dynamics.

A particularly desirable property for molecular material building blocks is addressability by external stimuli, for example light or electromagnetic fields. Electric fields are particularly promising since they are easy and quick to manipulate, unlike e.g. magnetic fields, and it is possible to address individual molecules on a surface using an STM tip [15, 16]. Yet, efficient magneto-electrical coupling within molecules remains elusive despite recent developments [17–20].

Valence delocalised molecules could provide a promising platform for realising magneto-electric coupling on a molecular scale. In these molecules, double exchange can contribute to intramolecular magnetic interactions alongside Heisenberg superexchange mechanisms, which, for example, can lead to novel intermediate-spin ground states [21–23]. Since double exchange relies on the dynamical delocalisation of spin-polarised valence electrons, electric fields could bias the potential energy of the delocalisation and thereby modify the character of the ground state wave function. Ultimately, this could lead to spin state switching when superexchange and double exchange compete [24, 25].

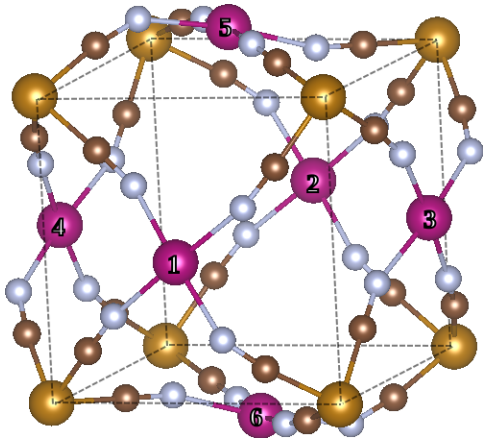

FIG. 1. Structure of the core of Fe_{14} with non-magnetic iron (A-sites) in gold and magnetic iron (B-sites) in purple. Brown and blue, respectively, depict the carbon and nitrogen atoms of the cyanide bridges. The dashed lines outline the cube-like structure. Capping ligands are omitted for clarity.

We present inelastic neutron scattering (INS) studies of Fe_{14}, a magnetic molecule with a diameter slightly larger than C_{60} (see Fig. 1) [26, 27]. Eight non-magnetic Fe^{2+} ions (the A-sites, low-spin $3d^6$) define the corners of the cube-like structure, and the magnetic ions are located at the cube faces (the B-sites). All iron ions are connected by cyanide bridges similar to Prussian Blue analogues [28]. At room temperature, the magnetic ions have an average valence of $+2\frac{2}{3}$ due to two electrons hopping

* michael.baker@manchester.ac.uk

between the six Fe^{3+} sites (high-spin $3d^5$). Mössbauer spectroscopy studies showed that electron hopping occurs on the nanosecond timescale at room temperature and that only the B-sites can accommodate the mobile electrons [26]. The molecule has an $S = 14$ ground state due to weak ferromagnetic coupling between neighbouring magnetic centres.

Based on those findings, it is believed that Fe_{14} exhibits partial valence delocalisation (Robin and Day class II), and consequently, that double exchange contributes to the magnetic interactions within Fe_{14} [21, 29, 30]. However, due to its intrinsic complexity, the details regarding the electronic structure of this unique molecule remain unknown despite the large variety of previously employed experimental methods [26]. With INS, we directly probe the energies and momentum transfer (Q) dependencies of the low-lying spin excited states thanks to the strong selection rules $\Delta S = \Delta m_S = \pm 1, 0$. This provides the first spectroscopic information about the intricacies of the spin dynamics of Fe_{14}. Furthermore, we show that the Q-dependencies and delocalised electron distributions for particular states are correlated and thereby establish INS as a unique tool for investigating valence delocalisation within molecules.

II. INELASTIC NEUTRON SCATTERING

A. Experimental Details

Our INS experiments were carried out with the direct-geometry time-of-flight disk chopper (dg-TOF-dc) spectrometer IN5 at the Institut Laue-Langevin in Grenoble, France. Experiments with neutron wavelength $\lambda = 5$ and 6.5 Å were performed with a small protonated polycrystalline sample ($m \approx 500$ mg), while later high-resolution experiments ($\lambda = 10$ Å) were carried out with a larger ^{11}B-enriched sample to minimise neutron absorption effects ($m = 1.57$ g). For all measurements, our polycrystalline Fe_{14} sample was sealed in an aluminium cylinder (annular geometry) to avoid multiple scattering, and we used Mantid for all INS data treatment [31, 32].

The chopper settings yielded quasi-Gaussian resolutions with full-width-at-half-maximums (FWHMs) of 82, 40, and 12 μeV at $\hbar\omega = 0$ for $\lambda = 5$, 6.5, and 10 Å respectively. For dg-TOF-dc spectrometers, the energy resolution is generally dependent on $\hbar\omega$. For this reason, we used an analytical expression to calculate the FWHM of the resolution for $\hbar\omega \neq 0$ [33].

B. INS Data Analysis

Fig. 2 shows the low-temperature ($T = 1.6$ K) INS spectrum of Fe_{14} measured using neutrons with $\lambda = 6.5$ Å. The spectrum has three distinct local maxima on the Stokes side ($\hbar\omega > 0$); they are located at approximately $\hbar\omega \approx 0.4$, 0.6, and 0.9 meV and appear to have

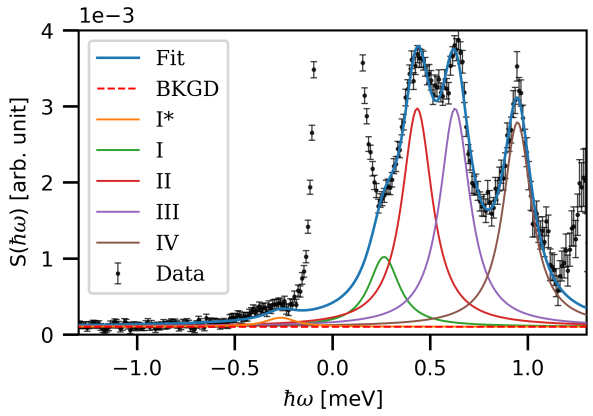

FIG. 2. INS intensity vs. $\hbar\omega$ for Fe_{14} measured with $\lambda = 6.5$ Å at $T = 1.6$ K integrated over $Q = 0.8 - 1.7$ Å^{-1} (black markers). The full lines mark the five resolution-convoluted Lorentzians used to model data (see legend and Tab. I), and the red dashed line mark the flat background.

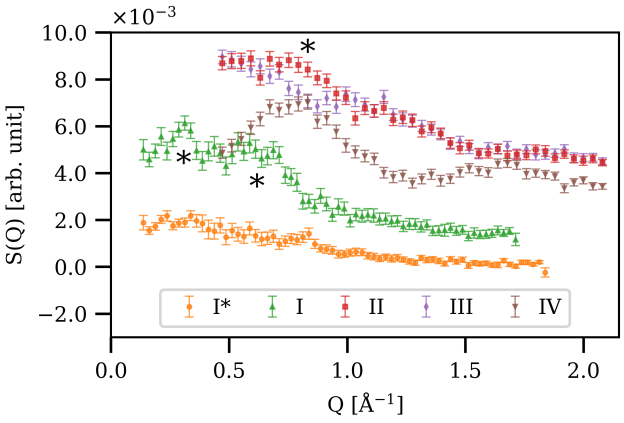

FIG. 3. INS intensity vs. Q for excitations I*-IV (see legend) measured at $T = 1.6$ K with $\lambda = 6.5$ Å (I*, I) or $\lambda = 5$ Å (II, III, IV). Data is integrated over intervals of $\hbar\omega = \pm 0.03$ (I) or $\hbar\omega = \pm 0.05$ meV (others) centred at $\hbar\omega_{0,j}$ (see Tab. I). The asterisks mark local maxima caused by spurious scattering.

Lorentzian line shapes. The features are significantly broader than the FWHM of the resolution (~ 40 μeV). The anti-Stokes side of the spectrum ($\hbar\omega < 0$) contains a single low-intensity excitation at $\hbar\omega \approx -0.3$ meV, i.e. smaller $|\hbar\omega|$ than any of the local maxima on the Stokes side. In the light of energy conservation, this implies that there is an unresolved fourth peak on the Stokes side.

All peaks in the INS spectrum in Fig. 2 can be assigned as magnetic excitations from the ground $S = 14$ manifold (cold bands) based on their Q-dependencies (see Fig. 3) and their behaviour as T increases (See Appendix B). The intensities decay with increasing Q as a consequence of the magnetic form factor, and all distinct features on the Stokes side become less intense as T increases due to

thermal depopulation of the ground state [34]. It is plausible that population of excited spin states makes transitions to previously inaccessible spin manifolds ($S \leq 12$) possible at $T > 1.6$ K. However, the proximity and intrinsic broadening of the excitations prevents obtaining any quantitative information about the existence of such states from the spectra measured at elevated temperatures ($T \geq 3$ K).

To quantify the intensities, energies, and intrinsic line broadenings of the observed cold bands, we model the spectrum in Fig. 2 with a combination of a constant background and five resolution-convoluted Lorentzian functions as elaborated in Appendix A [35]. The lines in Fig. 2 show the resulting best model as well as the individual Lorentzians, and Tab. I summarises the parameters.

The FWHM of all excitations are equal within the errorbars, which indicates that the broadenings indeed have the same origin for all states as assumed when constraining the FWHMs of I*-III to be equal. Notewothily, the FWHMs are also equal to the width of the quasi-elastic broadening of the elastic line as described in Appendix C, which suggests that it and the broadenings of I*-IV have a common origin. Such quasi-elastic broadening can be caused by vibronic coupling of low-lying magnetic states to states in a region with substantial phonon partial density-of-states [36–38]. Another possibility is that short-range correlations emerge due to the proximity to long-range magnetic order, which sets in at $T_c = 0.8$ K for Fe_{14}, i.e. less than 1 K colder than the temperature of our INS measurement [26]. However, our data does not allow us to distinguish between these two possible reasons for the broadness of our INS spectra.

The intensities of II-IV are all similar, while I is approximately three times less intense. This implies that the wave function of the first excited state has a different character relative to the excited states at higher energies. Q-dependencies can also help to differentiate between excitations to states who's wave functions have different characters. Fig. 3 shows the Q-dependencies of all excitations measured using neutrons with either $\lambda = 6.5$ Å (I* and I) or $\lambda = 5$ Å (II, III, and IV). Due to their proximity to the elastic line, the Q-dependencies of I and II contain artefacts, which are marked with asterisks on Fig. 3. IV has a distinct oscillatory Q-behaviour, as often found for molecular nanomagnets, with local maxima at $Q = 0.79$ and 1.68 Å^{-1} [34]. II and III have identical Q-dependencies, which underlines their similar nature. They show less pronounced oscillations, which clearly distinguishes them from IV. I is also clearly different from IV, however we cannot draw further conclusions from its Q-dependence due its low intensity and the prominence of artefacts in the data.

TABLE I. Best-fit values for the Lorentzian parameters describing the magnetic excitations in Fig. 2 (see eq. (A1)).

	$I_j/10^{-3}$ [arb. unit]	$\hbar\omega_{0,j}$ [meV]	γ_j [μeV]	R FWHM[a] [μeV]
I*	0.12(5)[b]	-0.264(8)[c]	181(8)[d]	40.0
I	0.94(4)[b]	0.264(8)[c]	181(8)[d]	32.5
II	2.93(8)	0.434(2)	181(8)[d]	30.7
III	2.92(5)	0.627(2)	181(8)[d]	28.5
IV	2.73(7)	0.947(2)	173(8)	25.4

[a] $=2\sqrt{2\ln 2}\sigma(\hbar\omega_{0,j})$, the expression for $\sigma(\hbar\omega_{0,j})$ is given in [33]
[b] Constrained to obey the principle of detailed balance
[c] Constrained to obey energy conservation
[d] Tied to the same value

III. SPIN HAMILTONIAN MODELLING

We use spin Hamiltonian modelling to interpret our INS results. Evaluation of an appropriately designed Hamiltonian yields spin state eigenvalues and -vectors which can be directly compared to INS observables [34]. To describe the spin dynamics of Fe_{14}, we employ the Hamiltonian

$$\mathcal{H} = \sum_{i,j\neq i} \mathcal{H}^{\mathrm{tr},1}_{i\to j} + \sum_{i,j,k,l} \mathcal{H}^{\mathrm{tr},2}_{i\to k,j\to l} + \sum_i \left(\mathcal{H}_H(D_i) + U_i\right) \tag{1}$$

which incoorporates both Heisenberg and double exchange. D_i, i = 1-15 define the possible distributions of the two delocalised electrons across the six B-sites and $\mathcal{H}_{\mathrm{H}}(D_i)$ are the Heisenberg Hamiltonians for a particular D_i. U_i parameterise the intrinsic energy differences between D_i's, for example the difference in Coulomb repulsion energy between D_i's with the extra electrons on neighbouring or opposite faces of the Fe_{14}-cube.

The Heisenberg Hamiltonians are given by [39]

$$\mathcal{H}_{\mathrm{H}}(D_i) = -\sum_{n,m\neq n} J_{n,m}(D_i)\,(\mathbf{s}_n \cdot \mathbf{s}_m) \tag{2}$$

where $\mathbf{s}_{n,m}$ are spins on neighbouring sites and $J_{n,m}$ is the associated exchange constant. The value of $J_{n,m}$ depends on D_i; $J_{n,m} = J_1$ if $s_n = s_m = 5/2$, $J_{n,m} = J_2$ if s_n or s_m are equal to 2, and $J_{n,m} = J_3$ if $s_n = s_m = 2$. We have previously shown that exchange constants in valence delocalised molecules depend on the valences of the involved sites, which justifies the atypical inclusion of oxidation state-dependent J's [40].

The first two terms in eq. (1) describe the double exchange contribution for one- and two-electron transfers, respectively. The first term mixes two D_i's which differ in the location of exactly one electron and is given by [22]

$$\mathcal{H}^{tr,1}_{i\to j} = t_{ij} \sum_\sigma c^\dagger_{j\phi\sigma} c_{n\phi\sigma} \tag{3}$$

where $c^\dagger_{k\phi\sigma}$ and $c_{k\phi\sigma}$, respectively, create and annihilate an electron with projection σ in orbital ϕ on site k. t_{ij} is the double exchange parameter which governs electron transfer. Since only neighbouring B-sites are connected by ligands we set $t_{ij} = t$ for nearest neighbours and $t_{ij} = 0$ otherwise. The two-electron contribution to

double exchange can be expressed as the product of two one-electron transfers [22].

$$\mathcal{H}^{\mathrm{tr},2}_{i\to k,j\to l} = \mathcal{H}^{tr,1}_{i\to k}\mathcal{H}^{tr,1}_{j\to l} \tag{4}$$

An important property of $\mathcal{H}$ is that the trace over a particular subspace, defined by D_i, of the outer product of an arbitrary eigenstate $|\psi\rangle$ with itself yields the contribution of D_i to the electron distribution for $|\psi\rangle$. Thus, it is possible to extract the distribution of the mobile electrons for individual eigenstates.

Iron ions on opposite faces of the Fe_{14} cube are $\Delta r = 2.54$ Å further apart than ions occupying neighbouring B-sites. In free space, this would stabilise D_i's with the two electrons on opposite faces by $E = e^2/(4\pi\epsilon_0\Delta r) \approx 650$ meV due to Coulomb repulsion. To limit the complexity of our model, we fix $U_i = 650$ meV for D_i's with electron occupation on neighbouring sites and $U_i = 0$ for the others. Since this choice makes it extremely unfavourable to have two $s = 2$ sites as nearest neighbours, J_3 has no influence on the low-lying energy levels, and we fix it to $J_3 = J_2$.

This leaves three free parameters in our model: J_1, which governs superexchange between $s = 5/2$ sites, J_2, which governs superexchange between mixed-valence sites, and t, which governs double exchange. We use MVPACK to set up and diagonalise $\mathcal{H}$ (see eq. (1)) [41]. This program takes full advantage of the irreducible tensor operator technique, whereby it deconstructs $\mathcal{H}$ into block-diagonal elements; for our model the maximal block dimension is 7050x7050. In the product state basis, $\mathcal{H}$ has dimension 468000x468000.

For $J_1 = J_2 = 0$, the model in eq. (1) has an $S = 0$ ground manifold for all $t < 0$, which is in stark contrast to the experimentally determined $S = 14$ ground manifold of Fe_{14}. This shows that double exchange can give rise to antiferromagnetic couplings within large molecules in contrast to in dimers, where double exchange always is ferromagnetic [21]. All $0 < t \lesssim U/2$ also give rise to an $S = 0$ ground manifold, while an $S = 14$ ground manifold emerges for $0 < U/2 < t$. This shows that Coulomb repulsion significantly suppresses the ferromagnetic interaction caused by $t > 0$. However, for $0 < U/2 < t$, the first excited $S = 13$ manifolds have energies $E_1 \approx 0.1t$ and $E_2 = 0.2t$, which for all possible t's are much larger than Fe_{14}'s dynamical range given $U = 650$ meV. Therefore, we conclude that double exchange alone cannot be the origin of ferromagnetic coupling within Fe_{14}.

When including weak Heisenberg exchange ($J_1 = J_2 \approx 10$ μeV), three degenerate $S = 14$ manifolds make up the ground level for moderate $t < 0$. The model furthermore has five low-lying INS-active levels, each composed of three degenerate $S = 13$ manifolds. Letting $J_1 \neq J_2$ while both are still positive perturbs the separation between the five $S = 13$ levels, but the overall behaviour of the model does not change. We label the ground level GS, the five $S = 13$ levels $\alpha - \epsilon$, and each of the 18 total manifolds a-r. This model predicts five INS excitations, one more than we observe. Yet, no other model is better suited to describe our INS data. Simpler models predict three or fewer low-lying INS transitions, and more complicated models do not overcome the obvious flaw of producing a fifth INS-active level.

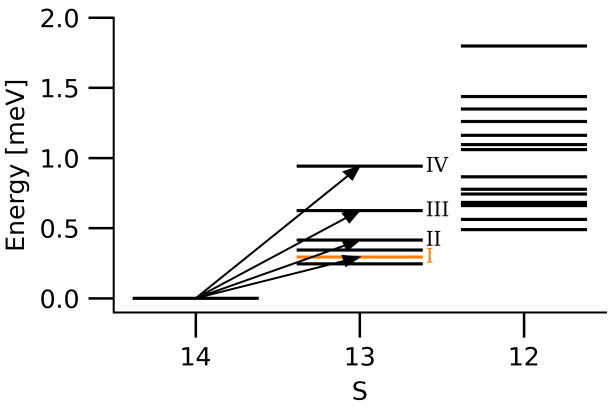

FIG. 4. Energy level scheme for Fe_{14} (black bars) calculated using eq. (1) with $J_1 = 41.8(2)$ μeV, $J_2 = 6.8(2)$ μeV and $t = -9.087(2)$ meV. The orange bar marks the average of the two lowest-lying $S = 13$ used to model I. The arrows mark the observed INS transitions.

In an attempt to fit the model by comparing the eigenvalues of $\mathcal{H}$ with the experimentally determined excitation energies, we decided to compare the energy of I ($\hbar\omega = 0.264(8)$ meV) to the average energy of levels α and β, the two lowest-lying $S = 13$ levels, while II-IV were compared to the three $S = 13$ levels with higher energy (γ, δ, and ϵ). The best fit yielded $J_1 = 41.8(2)$ μeV, $J_2 = 6.8(2)$ μeV and $t = -9.087(2)$ meV. Fig. 4 shows the resulting energy level scheme for $\hbar\omega \leq 2$ meV and $S \geq 12$, and Tab. II contains the exact excitation energies of levels α-ϵ. The presence of numerous $S = 12$ levels at $\hbar\omega < 2$ meV explains why the INS spectra measured at elevated T contain no distinct features: they likely contain too many overlapping excitations. The model contains no further $S = 13$ levels below 600 meV.

The obtained values of J are on average larger than $J_1 = J_2 = J_{\mathrm{mag}} = 7.6$ μeV, the value reported in Ref. 26 based on modelling of iso-thermal field-dependent magnetisation ($T = 2$ K) [42]. However, based on our INS data, $J_{\mathrm{mag}} = 7.6$ μeV is clearly an underestimation. For that value of J and $t = 0$, the highest-lying INS-active level lies at $\hbar\omega \approx 0.3$ meV, i.e. approximately three times less than the energy of IV. The proximity to long-range magnetic order, which can affect the field-dependence of magnetisation, may be the origin of this discrepancy.

The mobile electrons are distributed differently within the 18 manifolds (a-r) despite them being grouped into six degenerate trios that make up the GS and the five $S = 13$ levels (α-ϵ). Tab. III gives an overview of the average electron occupation for each manifold within the GS and Tab. II compares the occupations of each magnetic site for the 15 excited manifolds. Within the GS, manifold a

TABLE II. Distribution of the two mobile electrons across the magnetic sites for each manifold within the five low-lying $S = 13$ levels obtained from the best fit of the model in eq. (1) to INS data. The distributions are equal for each site pair on opposite faces of the Fe_{14} cube (see numbering in Fig. 1). $\hbar\omega$ refers to the energies yielded by the best fit of $\mathcal{H}$, and Exp. refers to the label of the corresponding experimentally determined excitation.

Level	α			β			γ			δ			ϵ		
$\hbar\omega$	0.245 meV			0.343 meV			0.414 meV			0.625 meV			0.941 meV		
Exp.	I						II			III			IV		
Manifold	d	e	f	g	h	i	j	k	l	m	n	o	p	q	r
Sites 1-2	0.167	0.500	0.333	0.001	0.482	0.518	0.493	0.412	0.095	0.498	0.043	0.459	0.484	0.001	0.515
Sites 3-4	0.167	0.500	0.333	0.001	0.518	0.482	0.446	0.148	0.406	0.500	0.459	0.042	0.515	0.002	0.483
Sites 5-6	0.666	0.001	0.333	0.999	0.001	0.001	0.061	0.440	0.499	0.002	0.499	0.500	0.001	0.997	0.003

TABLE III. Distribution of the two mobile electrons across the magnetic sites for each manifold within the ground level obtained from the best fit of the model in eq. (1) to INS data. The distributions are equal for each site pair on opposite faces of the Fe_{14} cube (see numbering in Fig. 1)

Level	GS		
Manifold	a	b	c
Sites 1-2	0.241	0.759	0.000
Sites 3-4	0.759	0.241	0.000
Sites 5-6	0.000	0.000	1.000

is localised with the electrons located on sites 5 and 6. In contrast, the electrons are delocalised across sites 1-4 for b and c, which make up the rest of the GS. Manifold b has slight preferential occupation of sites 1-2, while manifold c has a slight preference for sites 3-4.

The electron distributions within the six manifolds that make up levels γ and δ, which correspond to II and III, respectively, all follow the same trend: The two electrons are shared approximately equally between four sites, while one pair of sites have little-to-no electron occupation. Excitations II and III also had identical Q-dependencies, which suggests that there is a connection between the Q-dependence and the distribution of the mobile electrons within the corresponding level.

The compositions of levels β and ϵ, where the latter corresponds to IV, are different from the compositions of γ and δ. β and ϵ resemble the ground level by being composed of one localised manifold and two delocalised manifolds with almost equal electron occupation on sites 1-4. This supports the proposition that there is a link between the electron distributions and the Q-dependence since for IV, both its Q-dependence and electron distribution stand out compared to II and III.

Level α, which combines with level β to represent I, has an unique composition: one of its constituent manifolds has equal occupation of all six sites. Based on the two above paragraphs, we predict that this could give rise to a unique Q-dependence of level α and therefore excitation I. The fact that the experimentally determined intensity of I stands out compared to the others support this idea. However, due to the crude approximation of representing I as a combination of levels α and β, and the artefacts present in the experimentally determined Q-dependence of I, this cannot be quantitatively assessed.

IV. CONCLUSION

We have presented INS studies of the low-energy spin dynamics of Fe_{14} in which two mobile electrons undergo thermally activated transfer between six high-spin Fe^{3+} sites. We found four low-lying spin excited states with $S = 13$ at $\hbar\omega = 0.264(8)$, 0.434(2), 0.627(2), and 0.947(2) meV. They all have large intrinsic line broadenings equal in magnitude to the quasi-elastic broadening of the elastic line, which could emerge from magneto-vibronic coupling or the proximity of magnetic ordering.

A spin Hamiltonian model incorporating Heisenberg exchange, double exchange, and Coulomb repulsion provided an acceptable description of the determined excitation energies. The optimal parameters were $t = -9.087(2)$ meV, $J_1 = 41.8(2)$ μeV, and $J_2 = 6.8(2)$ μeV. t parameterises double exchange, while J_1/J_2 govern Heisenberg exchange between pairs of $s = 5/2$ sites or within mixed-valence pairs, respectively. The energies of the low-lying levels did not depend on the fixed Coulomb parameter $U = 650$ meV. Our modelling showed that the $S = 14$ ground level emerges due to ferromagnetic Heisenberg exchange overcoming antiferromagnetic double exchange ($t < 0$). Models with ferromagnetic double exchange ($t > 0$) could not give rise to an $S = 14$ ground level because the strong Coulomb repulsion heavily suppresses the ferromagnetic effect of $t > 0$.

Lastly, we were able to extract the distribution of the mobile electrons within the ground and low-lying excited levels from the Hamiltonian model. The ground level is composed of both localised and delocalised $S = 14$ manifolds, which confirms the predicted partially delocalised nature of Fe_{14}. In addition, excitations with different Q-dependencies seem to have different electron occupations. This suggests that INS can access unique information about the distribution of valence delocalised electrons within molecules and reinforces that INS remains a crucial tool for elevating the fundamental understanding of molecular spin dynamics.

ACKNOWLEDGMENTS

The authors thank Institute Laue-Langevin (ILL) for access to neutron beam time, and RTC thanks ILL for a PhD fellowship.

Appendix A: Fitting Procedure for INS Spectra

We use the following model to describe the INS spectrum in Fig. 2

$$S(\omega) = S_0 + \sum_{j=1}^{5} R(\omega_{0,j}) * L_j(\omega) \tag{A1a}$$

$$R(\omega_{0,j}) = \frac{1}{\sqrt{2\pi}\sigma(\omega_{0,j})} e^{-\frac{(\hbar\omega-\hbar\omega_{0,j})^2}{2\sigma(\omega_{0,j})}} \tag{A1b}$$

$$L_j(\omega) = \frac{I_j}{2\pi} \frac{\gamma_j}{(\hbar\omega-\hbar\omega_{0,j})^2 + (\gamma_j/2)^2} \tag{A1c}$$

where S_0 is a flat background, $R(\omega_{0,j})$ is the resolution function, and $*$ denotes convolution. L_1 through L_5 are Lorentzians that describe the observed INS transitions. The parameters I_j, $\omega_{0,j}$ and γ_j denote the intensities, positions and FWHMs of the Lorentzians, respectively.

Due to energy conservation it must be that $-\hbar\omega_{0,1} = \hbar\omega_{0,2}$, and L_1 and L_2 must furthermore obey the principle of detailed balance, $S(-\omega) = \exp\{-\hbar\omega/k_BT\}S(\omega)$ [35]. Thus, with the constraints imposed by physics, the model contains 14 free parameters: 13 Lorentzian parameters and the background S_0. However, it was not possible to obtain a stable fit of 14 parameters due to the large intrinsic line broadenings and close proximity of excitations I-III in the region $\hbar\omega = 0.2$-0.7 meV. Therefore, we impose the constraint that $\gamma_1 = \gamma_2 = \gamma_3 = \gamma_4$, which is justifiable since the same physical phenomenon most likely is responsible for the intrinsic broadening of I*-III. We optimised the model in eq. (A1) by minimising the χ^2 using the fitting tool within Mantid [31, 32].

Appendix B: INS Spectra at Elevated Temperatures

Fig. A1 (left) shows the temperature dependence of the INS spectrum of Fe_{14} measured with $\lambda = 6.5$ Å at $T = 1.6$ K (black), 3 K (dark purple), 6 K (purple) and 15 K (yellow). This clearly shows that the weak feature on the anti-Stokes side (I*) is magnetic since it increases in intensity with increasing T.

Appendix C: Quasi-Elastic Signal Reveals Intrinsic Line Broadening

High-resolution INS data measured using neutrons with $\lambda = 10$ Å revealed a substantial broadening of the elastic line at $T = 1.6$ K as Fig. A1 (right) shows. To quantify the intensity of the quasi-elastic signal and its FWHM we fit the following model to the data

$$S(\omega) = S_0(\omega) + R(\omega_0) * (\delta(\omega-\omega_0) + B(\omega)L(\omega)) \tag{C1a}$$

$$R(\omega_0) = \frac{1}{\sqrt{2\pi}\sigma(\omega_0)} e^{-\frac{(\hbar\omega-\hbar\omega_0)^2}{2\sigma(\omega_0)}} \tag{C1b}$$

$$L(\omega) = \frac{I}{2\pi} \frac{\gamma}{(\hbar\omega-\hbar\omega_0)^2 + (\gamma/2)^2} \tag{C1c}$$

$$B(\omega) = \frac{\hbar\omega-\hbar\omega_0}{1-e^{-\frac{\hbar omega-\hbar\omega_0}{k_BT}}} \tag{C1d}$$

where $B(\omega)$ is the Bose factor, which ensures that the quasi-elastic signal obeys the principle of detailed balance, δ is Dirac's delta-function and $S_0(\omega)$ is a fourth order polynomial accounting for the background. The rest of the symbols have the same meanings as in eq. (A1). We use a fourth-order polynomial for the background since a flat background in the time-of-flight domains scales as $(\hbar\omega)^4$ when converted. To make S_0 well-behaved when fitting we implement the constraint $\partial S_0/\partial\omega > 0$.

We fit the model to data my minimising the χ^2. The lines on Fig. A1 (right) show the resulting model, the background, and the Lorentzian describing the quasi-elastic signal, which has $\gamma = 170(50)$ μeV and $I = 5.4(9) \cdot 10^{-5}$.

[1] R. Sessoli, D. Gatteschi, A. Caneschi, and M. Novak, Magnetic bistability in a metal-ion cluster, Nature **365**, 141 (1993).

[2] L. Thomas, F. Lionti, R. Ballou, D. Gatteschi, R. Sessoli, and B. Barbara, Macroscopic quantum tunnelling of magnetization in a single crystal of nanomagnets, Nature **383**, 145 (1996).

[3] M. L. Baker, T. Guidi, S. Carretta, J. Ollivier, H. Mutka, H. U. Güdel, G. A. Timco, E. J. L. McInnes, G. Amoretti, R. E. P. Winpenny, and P. Santini, Spin dynamics of molecular nanomagnets unravelled at atomic scale by four-dimensional inelastic neutron scattering, Nat. Phys. **8**, 906 (2012).

[4] M. Leuenberger and D. Loss, Quantum computing in molecular magnets, Nature **410**, 789–793 (2001).

[5] C. Schlegel, J. van Slageren, M. Manoli, E. K. Brechin, and M. Dressel, Direct observation of quantum coherence in single-molecule magnets, Phys. Rev. Lett. **101**, 147203 (2008).

[6] C. A. P. Goodwin, F. Ortu, D. Reta, N. F. Chilton, and D. P. Mills, Molecular magnetic hysteresis at 60 kelvin in dysprosocenium, Nature **548**, 439 (2017).

[7] F.-S. Guo, B. M. Day, Y.-C. Chen, M.-L. Tong, A. Mansikkamäki, and R. A. Layfield, Magnetic hysteresis up to

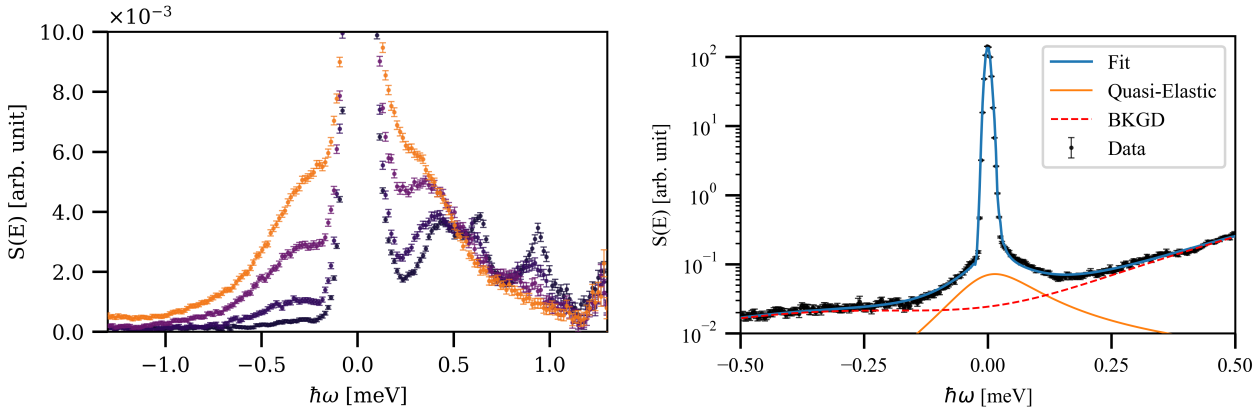

FIG. A1. **Left**: INS intensity vs. $\hbar\omega$ for Fe_{14} measured with $\lambda = 6.5$ Å at $T = 1.6$ K (black), 3 K (dark purple), 6 K (purple), and 15 K (yellow) integrated over the momentum transfer range $Q = 0.8 - 1.7$ Å^{-1}. Due to the plethora of overlapping peaks and their intrinsic broadness it is not possible to extract quantitative information from spectra measured at $T \geq 3$ K. **Right**: Logarithm of the INS intensity vs. $\hbar\omega$ for Fe_{14} measured with $\lambda = 10$ Å integrated over the momentum transfer range $Q = 0.1 - 0.75$ Å (black markers). The full lines mark the total fit (blue), the quasi-elastic signal (orange) and the background (red dashed).

80 Kelvin in a dysprosium metallocene single-molecule magnet, Science **362**, 1400 (2018).

[8] C. A. Gould, K. R. McClain, D. Reta, J. G. C. Kragskow, D. A. Marchiori, E. Lachman, E.-S. Choi, J. G. Analytis, R. D. Britt, N. F. Chilton, B. G. Harvey, and J. R. Long, Ultrahard magnetism from mixed-valence dilanthanide complexes with metal-metal bonding, Science **375**, 198 (2022).

[9] S. Sanvito, Molecular spintronics, Chem. Soc. Rev. **40**, 3336 (2011).

[10] A. Ardavan, O. Rival, J. J. L. Morton, S. J. Blundell, A. M. Tyryshkin, G. A. Timco, and R. E. P. Winpenny, Will spin-relaxation times in molecular magnets permit quantum information processing?, Phys. Rev. Lett. **98**, 057201 (2007).

[11] C. J. Wedge, G. A. Timco, E. T. Spielberg, R. E. George, F. Tuna, S. Rigby, E. J. L. McInnes, R. E. P. Winpenny, S. J. Blundell, and A. Ardavan, Chemical engineering of molecular qubits, Phys. Rev. Lett. **108**, 107204 (2012).

[12] S. Chicco, G. Allodi, A. Chiesa, E. Garlatti, C. D. Buch, P. Santini, R. De Renzi, S. Piligkos, and S. Carretta, Proof-of-concept quantum simulator based on molecular spin qudits, JACS **146**, 1053 (2024).

[13] C.-J. Yu, S. von Kugelgen, D. W. Laorenza, and D. E. Freedman, A molecular approach to quantum sensing, ACS Central Science **7**, 712 (2021).

[14] K. R. Mullin, D. W. Laorenza, D. E. Freedman, and J. M. Rondinelli, Quantum sensing of magnetic fields with molecular color centers, Phys. Rev. Res. **5**, L042023 (2023).

[15] A. Zhao, Q. Li, L. Chen, H. Xiang, W. Wang, S. Pan, B. Wang, X. Xiao, J. Yang, J. G. Hou, and Q. Zhu, Controlling the kondo effect of an adsorbed magnetic ion through its chemical bonding, Science **309**, 1542 (2005).

[16] S. Baumann, W. Paul, T. Choi, C. P. Lutz, A. Ardavan, and A. J. Heinrich, Electron paramagnetic resonance of individual atoms on a surface, Science **350**, 417 (2015).

[17] A. K. Boudalis, J. Robert, and P. Turek, First demonstration of magnetoelectric coupling in a polynuclear molecular nanomagnet: Single-crystal epr studies of $[Fe_3O(O_2CPh)_6(py)_3]ClO_4$·py under static electric fields, Chem. - Eur. J. **24**, 14896 (2018).

[18] J. Robert, N. Parizel, P. Turek, and A. K. Boudalis, Polyanisotropic magnetoelectric coupling in an electrically controlled molecular spin qubit, JACS **141**, 19765 (2019).

[19] X. Liu, Q. Liu, H. Zhao, G. Zhuang, Y. Ren, T. Liu, L. Long, and L. Zheng, Magnetoelectric Effect Generated Through Electron Transfer from Organic Radical to Metal Ion, National Science Review **10**, nwad059 (2023).

[20] M. Yazback, S. Liu, M. Shatruk, G. Christou, and H.-P. Cheng, Search for toroidal ground state and magnetoelectric effects in molecular spin triangles with antiferromagnetic exchange, The Journal of Physical Chemistry A **127**, 3814 (2023).

[21] G. Blondin and J. J. Girerd, Interplay of electron exchange and electron transfer in metal polynuclear complexes in proteins or chemical models, Chem. Rev. **90**, 1359 (1990).

[22] J. J. Borrás-Almenar, J. M. Clemente, E. Coronado, A. V. Palii, B. S. Tsukerblat, and R. Georges, High-nuclearity mixed-valence magnetic clusters: A general solution of the double exchange problem, J. Chem. Phys. **105**, 6892 (1996).

[23] J. Henthorn, G. Cutsail, T. Weyhermüller, and S. DeBeer, Stabilization of intermediate spin states in mixed-valent diiron dichalcogenide complexes, Nat. Chem. **14**, 328 (2022).

[24] C. Bosch-Serrano, J. M. Clemente-Juan, E. Coronado, A. Gaita-Ariño, A. Palii, and B. Tsukerblat, Electric field control of the spin state in mixed-valence magnetic molecules, ChemPhysChem **13**, 2662 (2012).

[25] A. Palii, S. Aldoshin, and B. Tsukerblat, Mixed-valence clusters: Prospects for single-molecule magnetoelectrics, Coord. Chem. Rev. **426**, 213555 (2021).

[26] W. Huang, S. Wu, X. Gu, Y. Li, A. Okazawa, N. Ko-

jima, S. Hayami, M. L. Baker, P. Bencok, M. Noguchi, Y. Miyazaki, M. Nakano, T. Nakanishi, S. Kanegawa, Y. Inagaki, T. Kawae, G.-L. Zhuang, Y. Shiota, K. Yoshizawa, D. Wu, and O. Sato, Temperature dependence of spherical electron transfer in a nanosized [Fe_{14}] complex, Nature Communications **10**, 5510 (2019).

[27] H. W. Kroto, J. R. Heath, S. C. O'Brien, R. F. Curl, and R. E. Smalley, C_{60}: Buckminsterfullerene, Nature **318**, 162 (1985).

[28] M. Verdaguer and G. S. Girolami, Magnetic prussian blue analogs, in *Magnetism: Molecules to Materials V* (John Wiley & Sons, Ltd, 2004) Chap. 9, pp. 283–346.

[29] M. B. Robin and P. Day, Mixed valence chemistry - A survey and classification, Adv. Inorg. Chem. Radiochem. **10**, 247 (1968).

[30] K. D. Demadis, C. M. Hartshorn, and T. J. Meyer, The localized-to-delocalized transition in mixed-valence chemistry, Chem. Rev. **101**, 2655 (2001).

[31] Mantid:, Manipulation and analysis toolkit for instrument data.; mantid project. (2013), http://dx.doi.org/10.5286/SOFTWARE/MANTID6.4.

[32] O. Arnold, J. Bilheux, J. Borreguero, A. Buts, S. Campbell, L. Chapon, M. Doucet, N. Draper, R. F. Leal, M. Gigg, V. Lynch, A. Markvardsen, D. Mikkelson, R. Mikkelson, R. Miller, K. Palmen, P. Parker, G. Passos, T. Perring, P. Peterson, S. Ren, M. Reuter, A. Savici, J. Taylor, R. Taylor, R. Tolchenov, W. Zhou, and J. Zikovsky, Mantid—data analysis and visualization package for neutron scattering and μsr experiments, Nucl. Instrum. Methods Phys. Res. A: Accel. Spectrom. Detect. Assoc. Equip. **764**, 156 (2014).

[33] R. E. Lechner, Optimization of a multi-disk chopper spectrometer for cold neutron scattering experiments, in *Proceedings of the 11th Meeting of the International Collaboration on Advanced Neutron Sources (ICANS-XI)*, Vol. 2 (1991) pp. 717–732.

[34] M. L. Baker, S. J. Blundell, N. Domingo, and S. Hill, Spectroscopy methods for molecular nanomagnets, in *Molecular Nanomagnets and Related Phenomena*, edited by S. Gao (Springer Berlin Heidelberg, Berlin, Heidelberg, 2015) pp. 231–291.

[35] H. Schober, An introduction to the theory of nuclear neutron scattering in condensed matter, J. Neutron Res. **17**, 109 (2014).

[36] S. W. Lovesey and U. Staub, Magnetoelastic model for the relaxation of lanthanide ions in $YBa_2Cu_3O_{7-\delta}$ observed by neutron scattering, Phys. Rev. B **61**, 9130 (2000).

[37] M. Kofu, T. Kajiwara, J. S. Gardner, G. G. Simeoni, M. Tyagi, A. Faraone, K. Nakajima, S. Ohira-Kawamura, M. Nakano, and O. Yamamuro, Magnetic relaxations in a tb-based single molecule magnet studied by quasielastic neutron scattering, Chemical Physics **427**, 147 (2013).

[38] M. A. Dunstan, M. J. Giansiracusa, M. Vonci, S. Calvello, D. Yu, A. Soncini, C. Boskovic, and R. A. Mole, Direct observation of magnetoelastic coupling in a molecular spin qubit: New insights from crystal field neutron scattering data, Chem. Sci. **14**, 3990 (2023).

[39] D. Gatteschi, R. Sessoli, and J. Villain, *Molecular Nanomagnets* (Oxford University Press, 2006).

[40] R. T. Christiansen, Double exchange spin dynamics within a valence delocalised molecule, in *Double Exchange Spin Dynamics within Valence Delocalised Molecular Magnets* (University of Manchester, 2024) Phd thesis 4, Chapter 4.

[41] J. J. Borrás-Almenar, S. Cardona-Serra, J. M. Clemente-Juan, E. Coronado, A. V. Palii, and B. Tsukerblat, MVPACK: A package to calculate energy levels and magnetic properties of high nuclearity mixed valence clusters, J. Comput. Chem. **31**, 1321 (2010).

[42] Note that there is a typo in Ref. 26. It is written that $J = 76$ μeV, which is off by a an order of magnitude. Reproducing their figures requires $J = 7.6$ μeV.

Chapter 6

Conclusions and Outlook

Since the resurgence of molecular magnetism in the 1990's, significant progress has been made towards understanding the fundamental quantum properties of molecules and exploiting them for technological applications. Molecules have the potential to be a key ingredient for the second quantum revolution, provided that we have solid knowledge about the quantum mechanics at play within [93], [94]. Therefore, it is imperative that we pursue investigations of the fundamental quantum mechanics that govern the properties of molecules to push the capabilities of molecule-based quantum technologies towards their full potential [95].

The work presented in this thesis set out to investigate a particular quantum mechanical phenomenon within molecules: valence delocalisation of electrons and the unique spin dynamics believed to emerge from the resulting double exchange. Previously, this phenomenon had mainly been studied within dimer molecules using indirect experimental methods and non-standardised analysis approaches. The main goal of our work was to establish INS as key method for investigating valence delocalisation. We chose INS because it addresses the main challenges faced by previous methods. We wanted expand the investigation of double exchange to molecules with more than two magnetic centres, and INS is an excellent tool for probing the spin dynamics of polynuclear molecules as previously shown for e.g. Mn_{12} or Cr_8 and derivatives [78]–[81]. Our hypothesis was furthermore that valence delocalisation could give rise to unique momentum transfer dependencies of the spin excitations when compared to dynamics of molecules governed only by Heisenberg exchange, and INS is currently the only method for probing momentum-resolved molecular spin dynamics.

Realising this goal required some method development. Spin Hamiltonian modelling is the typical method for interpreting INS data from molecules, and while modelling tools like *mint* and MAGPACK are well-developed none of the them facilitated INS calculations including double exchange. Therefore, we have implemented the general solution to the double exchange problem in *mint* [61]. The formalism is familiar to *mint* and Easyspin users, and the output of our code will soon be compatible with the rest of the functions of Easyspin.

In Chapters 3-5, we presented the main bodies of work undertaken during this thesis. In Chapter 3, we investigated how several spectroscopic techniques can combine to unravel the spin dynamics of strongly coupled systems when individual methods are insufficient. While this particular work does not involve valence delocalised molecules, its methodology is directly applicable to such systems. In Chapter 4 we investigated the spin dynamics

of $Fe_3O[O_2CC(CD_3)_3]_6(C_5D_5N)_3$ (**Fe_3-Piv**) using INS and used our new modelling tool for the interpretation. In Chapter 5, we investigated the effects of simultaneous delocalisation of multiple electrons across several magnetic centres. Specifically, we used INS to probe the spin dynamics of $[Fe(Tp)(CN)_3]_8[Fe(H_2O)(DMSO)]_6$ (Fe_{14}), a molecule in which two electrons become delocalised six multiple magnetic centres. Below, we present the conclusions from each Chapter one by one.

Manuscript 1

In this work, we showed how INS, HF EPR, FIRMS and magnetometry can combine to unravel spin dynamics of strongly coupled molecules inaccessible to a single technique. We exemplified our approach by studying structure-property relationships in a series of radical-bridged iron dimers based on $[[Fe(cth)]_2(dhbq)]^{3+}$ (cth = 5,5,7,12,12,14-hexamethyl-1,4,8,11-tetraaza-cyclotetradecane; H_2dhbq = 2,5-dihydroxy-1,4-benzoquinone). We found that functionalisation of the $dhbq^{3-}$ bridge can affect Fe-radical couplings in contrast to previous findings, and that centrosymmetry, controlled by the relative chirality of the cth ligands, imposes **g**-tensor isotropy [96].

The employed methodology is directly portable to other studies of magnetic molecules and is particularly useful for studying valence delocalised molecules since they are often strongly coupled. Our direct observation of an inter-multiplet transition with FIRMS is particularly promising for future investigations of polynuclear magnetic molecules.

Manuscript 2

In this work, our INS investigation of **Fe_3-Piv** provided the first direct spectroscopic evidence for double exchange spin dynamics within a valence delocalised molecule and firmly established that **Fe_3-Piv** belongs to Robin and Day class II. We showed that INS is sensitive to small deviations from equilateral symmetry in a triangular magnetic model, and that these deviations lead to low-lying magnetic states not present in localised analogues. Our modelling also showed that a static picture of the Heisenberg exchange parameters within a valence delocalised molecule is wrong - the Heisenberg coupling between two magnetic centres can vary by a factor of 4 if one of the interacting centres accommodates an extra electron. Lastly, we found that a magnetic excitation with prevalent charge transfer nature had an intrinsic INS line width which may be linked to the time scale of the electron transfer process.

Simulations of $S(\mathbf{Q}, \omega)$ based on the model extracted from powder INS data revealed that some double exchange excitations have unique momentum transfer features in agreement with our original hypothesis. This provides a strong motivation for pursuing INS experiments on deuterated single crystals in the future to obtain experimental evidence for these unique features. Our simulations furthermore showed that the **Q**-dependencies contain distinct features related to to the degree of electron localisation within the involved states, and consequently

that single-crystal INS could provide a direct handle on this elusive property.

From a broader perspective, the differences between **Fe_3-Piv** and its acetate and mixed-metal analogues shows that tailoring the properties of μ_3-oxo-centered carboxylates is possible, and thus that they could be a good framework for engineering new molecules for quantum applications. It has, for example, already been proposed to harness the magneto-electric coupling within a localised analogue, $[Fe_3O(O_2CPh)_6(py)_3]ClO_4 \cdot py$, to build a molecular exchange qubit. We expect that magneto-electrical coupling would be stronger within **Fe_3-Piv** thanks to valence delocalisation, which could lead to superior qubit properties.

Lastly, the rich magnetic behaviour of **Fe_3-Piv**'s far-infrared spectrum shows that FIRMS has has the potential to provide detailed information about the spin dynamics of valence delocalised molecules. In particular, the ability of infrared radiation to induce both magnetic and electric dipole transitions could allows us to probe potential magneto-electric coupling in **Fe_3-Piv**. INS experiments in applied electric fields could also provide unique insight into these properties.

Manuscript 3

In this work, we used INS to investigate the elusive spin dynamics of Fe_{14}. Like for **Fe_3-Piv**, we found that transitions between states with different electron distributions had intrinsic INS line widths, which strengthens our proposition that these line widths are correlated to the dynamics of electron transfer processes. The line widths in Fe_{14} are equal to the quasi-elastic broadening of its elastic line, which suggested that the two have a common origin.

Our modelling showed that the ferromagnetic $S = 14$ ground state of Fe_{14} emerges because ferromagnetic Heisenberg exchanges overcomes antiferromagnetic double exchange. Like for **Fe_3-Piv**, a static picture of the Heisenberg exchange couplings was insufficient, this time the coupling gets weakened by a factor of six when a pair accommodates an extra electron. We furthermore found that the effects of ferromagnetic double exchange become heavily suppressed when a model contains strong Coulomb repulsion, which emphasises the critical role Coulomb repulsion plays when more than one electron becomes delocalised. Lastly, we were able to correlate the Q-dependencies of the excitations with the calculated electron occupations, which constitutes a compelling argument for optimising our double exchange modelling tool such that INS observables can be calculated from our model of Fe_{14}.

Outlook

Based on the findings presented manuscripts 2 and 3, we have shown that INS is a powerful tool for elucidating valence delocalised spin dynamics within molecules in the low-energy regime ($\hbar\omega < 10$ meV), even in the rather complex case where several electrons become delocalised across multiple magnetic centres. INS can furthermore access momentum-resolved information, which simulations showed contain unique information about the distribution of

delocalised electrons. Our findings also suggest that INS line widths contain information about vibronic coupling and/or electrons transfer dynamics analogously to how they can encode information about magnetic relaxation dynamics [83], [84]. Therefore, INS has the potential to become a key technique for investigating valence delocalisation. In the future, further development of our modelling tool and experiments on single crystals should investigate this potential.

When the dynamic range extends above 10 meV, INS has intrinsic limitations related to instrumentation and its high sensitivity to hydrogen vibrational dynamics. In those cases, manuscripts 1 and 2 showed that FIRMS can access rich information information about molecular spin dynamics. In particular, we demonstrated for the first time that inter-multiplet transitions can have FIRMS intensity, presumably due to vibronic coupling. On this basis, we believe that the scientific community could benefit from adapting FIRMS for studying polynuclear complexes analogously to how it has been adapted for investigating mononuclear complexes in recent years.

References

[1] R. Sessoli, D. Gatteschi, A. Caneschi, and M. Novak, "Magnetic bistability in a metal-ion cluster," *Nature*, vol. 365, pp. 141–143, 1993. DOI: 10.1038/365141a0 (cited on p. 13).

[2] J. R. Friedman, M. P. Sarachik, J. Tejada, and R. Ziolo, "Macroscopic measurement of resonant magnetization tunneling in high-spin molecules," *Phys. Rev. Lett.*, vol. 76, pp. 3830–3833, 20 1996. DOI: 10.1103/PhysRevLett.76.3830 (cited on p. 13).

[3] P. Perlepe, I. Oyarzabal, A. Mailman, *et al.*, "Metal-organic magnets with large coercivity and ordering temperatures up to 242 °C," *Science*, vol. 370, no. 6516, pp. 587–592, 2020. DOI: 10.1126/science.abb3861 (cited on p. 13).

[4] C. A. Gould, K. R. McClain, D. Reta, *et al.*, "Ultrahard magnetism from mixed-valence dilanthanide complexes with metal-metal bonding," *Science*, vol. 375, no. 6577, pp. 198–202, 2022. DOI: 10.1126/science.abl5470 (cited on pp. 13, 14, 22).

[5] C. A. P. Goodwin, F. Ortu, D. Reta, N. F. Chilton, and D. P. Mills, "Molecular magnetic hysteresis at 60 Kelvin in dysprosocenium," *Nature*, vol. 548, pp. 439–442, 2017. DOI: https://doi.org/10.1038/nature23447 (cited on p. 13).

[6] F.-S. Guo, B. M. Day, Y.-C. Chen, M.-L. Tong, A. Mansikkamäki, and R. A. Layfield, "Magnetic hysteresis up to 80 Kelvin in a dysprosium metallocene single-molecule magnet," *Science*, vol. 362, no. 6421, pp. 1400–1403, 2018. DOI: 10.1126/science.aav0652 (cited on p. 13).

[7] M. Bernhardt, M. D. Korzyński, Z. J. Berkson, *et al.*, "Tailored Lewis acid sites for high-temperature supported single-molecule magnetism," *JACS*, vol. 145, no. 23, pp. 12 446–12 451, 2023. DOI: 10.1021/jacs.3c02730 (cited on p. 13).

[8] Z. Hu, Y. Wang, A. Ullah, *et al.*, "High-temperature magnetic blocking in a monometallic dysprosium azafullerene single-molecule magnet," *Chem*, vol. 9, no. 12, pp. 3613–3622, 2023. DOI: https://doi.org/10.1016/j.chempr.2023.08.007 (cited on p. 13).

[9] M. Shiddiq, D. Komijani, Y. Duan, A. Gaita-Arino, E. Coronado, and S. Hill, "Enhancing coherence in molecular spin qubits via atomic clock transitions," *Nature*, vol. 531, pp. 348–351, 2016. DOI: 10.1038/nature16984 (cited on p. 13).

[10] S. Chicco, G. Allodi, A. Chiesa, *et al.*, "Proof-of-concept quantum simulator based on molecular spin qudits," *JACS*, vol. 146, no. 1, pp. 1053–1061, 2024. DOI: 10.1021/jacs.3c12008 (cited on p. 13).

[11] S. Sanvito, "Molecular spintronics," *Chem. Soc. Rev.*, vol. 40, pp. 3336–3355, 6 2011. DOI: 10.1039/C1CS15047B (cited on p. 13).

[12] H. J. Eckvahl, N. A. Tcyrulnikov, A. Chiesa, *et al.*, "Direct observation of chirality-induced spin selectivity in electron donor–acceptor molecules," *Science*, vol. 382, no. 6667, pp. 197–201, 2023. DOI: 10.1126/science.adj5328 (cited on p. 13).

[13] O. Sato, "Optically switchable molecular solids: Photoinduced spin-crossover, photochromism, and photoinduced magnetization," *Acc. Chem. Res.*, vol. 36, no. 9, pp. 692–700, 2003. DOI: 10.1021/ar020242z (cited on p. 13).

[14] A. Palii, S. Aldoshin, and B. Tsukerblat, "Mixed-valence clusters: Prospects for single-molecule magnetoelectrics," *Coord. Chem. Revs.*, vol. 426, p. 213 555, 2021. DOI: https://doi.org/10.1016/j.ccr.2020.213555 (cited on pp. 14, 23).

[15] C. Bosch-Serrano, J. M. Clemente-Juan, E. Coronado, A. Gaita-Ariño, A. Palii, and B. Tsukerblat, "Electric field control of the spin state in mixed-valence magnetic molecules," *ChemPhysChem*, vol. 13, no. 11, pp. 2662–2665, 2012. DOI: https://doi.org/10.1002/cphc.201200383 (cited on p. 14).

[16] E. I. Solomon, X. Xie, and A. Dey, "Mixed valent sites in biological electron transfer," *Chem. Soc. Rev.*, vol. 37, pp. 623–638, 4 2008. DOI: 10.1039/B714577M (cited on p. 14).

[17] S. Sharma, K. Sivalingam, F. Neese, and G. K.-L. Chan, "Low-energy spectrum of iron–sulfur clusters directly from many-particle quantum mechanics," *Nat. Chem.*, vol. 6, pp. 927–933, 2014. DOI: 10.1038/nchem.2041 (cited on p. 14).

[18] K. M. Lancaster, M. Roemelt, P. Ettenhuber, *et al.*, "X-ray emission spectroscopy evidences a central carbon in the nitrogenase iron-molybdenum cofactor," *Science*, vol. 334, no. 6058, pp. 974–977, 2011. DOI: 10.1126/science.1206445 (cited on p. 14).

[19] N. Cherkasov, A. Ibhadon, and P. Fitzpatrick, "A review of the existing and alternative methods for greener nitrogen fixation," *Chem. Eng. Process.*, vol. 90, pp. 24–33, 2015. DOI: https://doi.org/10.1016/j.cep.2015.02.004 (cited on p. 14).

[20] K. D. Demadis, C. M. Hartshorn, and T. J. Meyer, "The localized-to-delocalized transition in mixed-valence chemistry," *Chem. Rev.*, vol. 101, no. 9, pp. 2655–2686, 2001. DOI: 10.1021/cr990413m (cited on pp. 14, 21, 22).

[21] B. Bechlars, D. M. D'Alessandro, D. M. Jenkins, *et al.*, "High-spin ground states via electron delocalization in mixed-valence imidazolate-bridged divanadium complexes," *Nat. Chem.*, vol. 2, pp. 362–368, 2010. DOI: 10.1038/nchem.585 (cited on pp. 14, 20, 33).

[22] R. Nabi, J. K. Staab, A. Mattioni, *et al.*, "Accurate and efficient spin–phonon coupling and spin dynamics calculations for molecular solids," *JACS*, vol. 145, no. 45, pp. 24 558–24 567, 2023. DOI: 10.1021/jacs.3c06015 (cited on p. 14).

[23] L. A. Mariano, S. Mondal, and A. Lunghi, "Spin-vibronic dynamics in open-shell systems beyond the spin Hamiltonian formalism," *J. Chem. Theory Comput.*, vol. 20, no. 1, pp. 323–332, 2024. DOI: 10.1021/acs.jctc.3c01130 (cited on p. 14).

[24] S. E. Houck and N. J. Mayhall, "A combined spin-flip and IP/EA approach for handling spin and spatial degeneracies: Application to double exchange systems," *J. Chem. Theory Comput.*, vol. 15, no. 4, pp. 2278–2290, 2019. DOI: 10.1021/acs.jctc.8b01268 (cited on p. 14).

[25] J. J. Borrás-Almenar, S. Cardona-Serra, J. M. Clemente-Juan, E. Coronado, A. V. Palii, and B. Tsukerblat, "MVPACK: A package to calculate energy levels and magnetic properties of high nuclearity mixed valence clusters," *J. Comput. Chem.*, vol. 31, no. 6, pp. 1321–1332, 2010. DOI: https://doi.org/10.1002/jcc.21400 (cited on pp. 14, 24, 32).

[26] J. M. Clemente-Juan, A. Palii, B. Tsukerblat, and E. Coronado, "VIBPACK: A package to treat multidimensional electron-vibrational molecular problems with application to magnetic and optical properties," *J. Comput. Chem.*, vol. 39, no. 22, pp. 1815–1827, 2018. DOI: https://doi.org/10.1002/jcc.25355 (cited on p. 14).

[27] S. Stoll and A. Schweiger, "Easyspin, a comprehensive software package for spectral simulation and analysis in epr," *J. Magn. Reson.*, vol. 178, no. 1, pp. 42–55, 2006. DOI: https://doi.org/10.1016/j.jmr.2005.08.013 (cited on pp. 15, 32).

[28] M. L. Baker, *mint: Simulation of inelastic neutron scattering induced magnetic excitations for single-ions & finite exchange coupled spin-systems*, https://mlbakerlab.co.uk/mint, 2022 (cited on pp. 15, 32).

[29] C. Wilson, B. B. Iversen, J. Overgaard, *et al.*, "Multi-temperature crystallographic studies of mixed-valence polynuclear complexes: Valence trapping process in the trinuclear oxo-bridged iron compound, [$Fe_3O(O_2CC(CH_3)_3)_6(C_5H_5N)_3$]," *JACS*, vol. 122, no. 46, pp. 11 370–11 379, 2000. DOI: 10.1021/ja994162a (cited on pp. 15, 79).

[30] S. Scheins, J. Overgaard, G. A. Timco, *et al.*, "Pressure versus temperature effects on intramolecular electron transfer in mixed-valence complexes," *Chem. Eur. J.*, vol. 19, no. 1, pp. 195–205, 2013. DOI: https://doi.org/10.1002/chem.201201669 (cited on p. 15).

[31] W. Huang, S. Wu, X. Gu, *et al.*, "Temperature dependence of spherical electron transfer in a nanosized [Fe14] complex," *Nat. Commun.*, vol. 10, p. 5510, 2019. DOI: 10.1038/s41467-019-13279-y (cited on pp. 15, 116).

[32] D. J. Griffith, *Introduction to Quantum Mechanics*, 2nd. Person Education, 2015 (cited on pp. 15, 17, 18).

[33] S. Blundell, *Magnetism in Condensed Matter*. Oxford University Press, 2001 (cited on pp. 15–18, 25).

[34] J.-P. Launay and M. Verdauger, *Electrons in Molecules*. Oxford University Press, 2014 (cited on pp. 16, 20–22).

[35] J. J. Sakurai and J. Napolitano, *Modern Quantum Mechanics*, 2nd. Cambridge University Press, 2017 (cited on pp. 17, 18, 26).

[36] R. Boča and R. Herchel, "Antisymmetric exchange in polynuclear metal complexes," *Coord. Chem. Revs.*, vol. 254, no. 23, pp. 2973–3025, 2010, ISSN: 0010-8545. DOI: https://doi.org/10.1016/j.ccr.2010.06.012 (cited on p. 17).

[37] H. Kramers, "General theory of paramagnetic rotation in crystals," in *Proc. Acad. Sci. Amsterdam*, vol. 33, 1930, p. 959 (cited on p. 17).

[38] D. Gatteschi, R. Sessoli, and J. Villain, *Molecular Nanomagnets*. Oxford University Press, 2006 (cited on pp. 17, 20).

[39] E. Bauer and M. Rotter, "Magnetism of complex metallic alloys: Crystalline electric field effects," in *Properties and Applications of Complex Intermetallics*, pp. 183–248. DOI: 10.1142/9789814261647_0005 (cited on p. 17).

[40] I. Mirebeau, M. Hennion, H. Casalta, *et al.*, "Low-energy magnetic excitations of the Mn_{12}-acetate spin cluster observed by neutron scattering," *Phys. Rev. Lett.*, vol. 83, pp. 628–631, 3 1999. DOI: 10.1103/PhysRevLett.83.628 (cited on pp. 20, 31).

[41] R. Bircher, G. Chaboussant, A. Sieber, H. U. Güdel, and H. Mutka, "Transverse magnetic anisotropy in Mn_{12} acetate: Direct determination by inelastic neutron scattering," *Phys. Rev. B*, vol. 70, p. 212 413, 21 2004. DOI: 10.1103/PhysRevB.70.212413 (cited on pp. 20, 31).

[42] C. Zener, "Interaction between the d-shells in the transition metals. II. ferromagnetic compounds of manganese with perovskite structure," *Phys. Rev.*, vol. 82, pp. 403–405, 3 1951. DOI: 10.1103/PhysRev.82.403 (cited on p. 20).

[43] P. W. Anderson and H. Hasegawa, "Considerations on double exchange," *Phys. Rev.*, vol. 100, pp. 675–681, 2 1955. DOI: 10.1103/PhysRev.100.675 (cited on p. 20).

[44] C. Creutz and H. Taube, "Direct approach to measuring the Franck-Condon barrier to electron transfer between metal ions," *JACS*, vol. 91, no. 14, pp. 3988–3989, 1969. DOI: 10.1021/ja01042a072 (cited on p. 20).

[45] C. Creutz and H. Taube, "Binuclear complexes of ruthenium ammines," *JACS*, vol. 95, no. 4, pp. 1086–1094, 1973. DOI: 10.1021/ja00785a016 (cited on p. 20).

[46] S. Drüeke, P. Chaudhuri, K. Pohl, *et al.*, "The novel mixed-valence, exchange-coupled, class III dimer $[L_2Fe_2(\mu\text{-}OH)_3]^{2+}$(L =N,N ,N -trimethyl-1,4,7-triazacyclononane)," *J. Chem. Soc., Chem. Commun.*, pp. 59–62, 1 1989. DOI: 10.1039/C39890000059 (cited on p. 20).

[47] S. K. Dutta, J. Ensling, R. Werner, *et al.*, "Valence-delocalized and valence-trapped FeIIFeIII complexes: Drastic influence of the ligands," *Angew. Chem., Int. Ed. Engl.*, vol. 36, no. 1-2, pp. 152–155, DOI: https://doi.org/10.1002/anie.199701521 (cited on p. 20).

[48] J. R. Hagadorn, L. Que, W. B. Tolman, I. Prisecaru, and E. Münck, "Conformational tuning of valence delocalization in carboxylate-rich diiron complexes," *JACS*, vol. 121, no. 41, pp. 9760–9761, 1999. DOI: 10.1021/ja9920381 (cited on p. 20).

[49] Y. Dong, H. Fujii, M. P. Hendrich, *et al.*, "A high-valent nonheme iron intermediate. Structure and properties of $[Fe_2(\mu\text{-}O)_2(5\text{-Me-TPA})_2](ClO_4)_3$," *JACS*, vol. 117, no. 10, pp. 2778–2792, 1995. DOI: 10.1021/ja00115a013 (cited on p. 20).

[50] A. I. Gaudette, I.-R. Jeon, J. S. Anderson, F. Grandjean, G. J. Long, and T. D. Harris, "Electron hopping through double-exchange coupling in a mixed-valence diiminobenzoquinone-bridged Fe_2 complex," *JACS*, vol. 137, no. 39, pp. 12 617–12 626, 2015. DOI: 10.1021/jacs.5b07251 (cited on pp. 20, 33).

[51] D. Lee, C. Krebs, B. H. Huynh, M. P. Hendrich, and S. J. Lippard, "Valence-delocalized diiron(II,III) cores supported by carboxylate-only bridging ligands," *JACS*, vol. 122, no. 20, pp. 5000–5001, 2000. DOI: 10.1021/ja994448f (cited on p. 20).

[52] X.-Q. Ding, E. Bill, A. X. Trautwein, *et al.*, "Exchange interactions, charge delocalization, and spin relaxation in a mixed-valence di-iron complex studied by Mössbauer spectroscopy," *J. Chem. Phys.*, vol. 99, no. 9, pp. 6421–6428, 1993. DOI: 10.1063/1.465881 (cited on p. 20).

[53] K. K. Surerus, E. Munck, B. S. Snyder, and R. H. Holm, "A binuclear mixed-valence ferromagnetic iron system with an s = 9/2 ground state and valence trapped and detrapped states," *JACS*, vol. 111, no. 14, pp. 5501–5502, 1989. DOI: 10.1021/ja00196a086 (cited on p. 20).

[54] S. Dammers, T. P. Zimmermann, S. Walleck, *et al.*, "A mixed-valence fluorido-bridged FeIIFeIII complex," *Inorg. Chem.*, vol. 56, no. 4, pp. 1779–1782, 2017. DOI: 10.1021/acs.inorgchem.6b03093 (cited on p. 20).

[55] A. Stubna, D.-H. Jo, M. Costas, *et al.*, "A structural and mössbauer study of complexes with $Fe_2(\mu\text{-}OH)_2$ cores: Stepwise oxidation from FeII(μ-OH)$_2$FeII through FeII(μ-OH)$_2$FeIII to FeIII(μ-O)(μ-OH)FeIII," *Inorg. Chem.*, vol. 43, no. 10, pp. 3067–3079, 2004. DOI: 10.1021/ic030296k (cited on p. 20).

[56] J. Henthorn, G. Cutsail, T. Weyhermüller, and S. DeBeer, "Stabilization of intermediate spin states in mixed-valent diiron dichalcogenide complexes," *Nat. Chem.*, vol. 14, pp. 328–333, 2022. DOI: 0.1038/s41557-021-00853-5 (cited on pp. 20, 23, 33).

[57] A. Bencini, E. Berti, A. Caneschi, D. Gatteschi, E. Giannasi, and I. Invernizzi, "Electronic structure and nature of the ground state of the mixed-valence binuclear tetra(μ-1,8-naphthyridine-n,n)-bis(halogenonickel) tetraphenylborate complexes: Experimental and DFT characterization," *Chem. Eur. J.*, vol. 8, no. 16, pp. 3660–3670, 2002. DOI: https://doi.org/10.1002/1521-3765(20020816)8:16<3660::AID-CHEM3660>3.0.CO;2-H (cited on p. 20).

[58] M. B. Robin and P. Day, "Mixed valence chemistry - A survey and classification," *Adv. Inorg. Chem. Radiochem.*, vol. 10, pp. 247–422, 1968. DOI: https://doi.org/10.1016/S0065-2792(08)60179-X (cited on pp. 21, 22).

[59] J.-J. Girerd, V. Papaefthymiou, K. K. Surerus, and E. Munck, *Pure Appl. Chem.*, vol. 61, no. 5, pp. 805–816, 1989. DOI: doi:10.1351/pac198961050805 (cited on p. 22).

[60] G. Blondin, S. Borshch, and J.-J. Girerd, "When must double exchange be used?" *Comments on Inorg. Chem.*, vol. 12, no. 6, pp. 315–340, 1992. DOI: 10.1080/02603599208055168 (cited on p. 23).

[61] J. J. Borrás-Almenar, J. M. Clemente, E. Coronado, A. V. Palii, B. S. Tsukerblat, and R. Georges, "High-nuclearity mixed-valence magnetic clusters: A general solution of the double exchange problem," *J. Chem. Phys.*, vol. 105, no. 16, pp. 6892–6909, 1996. DOI: 10.1063/1.471983 (cited on pp. 24, 32, 125).

[62] S. A. Borshch, E. L. Bominaar, G. Blondin, and J. J. Girerd, "Double exchange and vibronic coupling in mixed valence systems. origin of the broken-symmetry ground state of $[Fe_3S_4]^0$ cores in proteins and models," *JACS*, vol. 115, no. 12, pp. 5155–5168, 1993. DOI: 10.1021/ja00065a030 (cited on p. 24).

[63] J. M. Clemente-Juan, J. J. Borrás-Almenar, E. Coronado, A. V. Palii, and B. S. Tsukerblat, "High-nuclearity mixed-valence clusters and mixed-valence chains: General approach to the calculation of the energy levels and bulk magnetic properties," *Inorg. Chem.*, vol. 48, no. 10, pp. 4557–4568, 2009. DOI: 10.1021/ic802201h (cited on p. 24).

[64] H. Schober, "An introduction to the theory of nuclear neutron scattering in condensed matter," *J. Neutron Res.*, vol. 17, pp. 109–357, 2014 (cited on pp. 25–27).

[65] M. L. Baker, S. J. Blundell, N. Domingo, and S. Hill, "Spectroscopy methods for molecular nanomagnets," in *Molecular Nanomagnets and Related Phenomena*, S. Gao, Ed. Springer Berlin Heidelberg, 2015, pp. 231–291 (cited on pp. 25–28).

[66] K. Lefmann, *Neutron Scattering: Theory, Instrumentation and Simulation*. Lecture Notes, University of Copenhagen, 2019 (cited on p. 26).

[67] G. L. Squires, *Introduction to the Theory of Thermal Neutron Scattering*. Cambridge University Press, 1978 (cited on p. 26).

[68] H. Rauch and W. Waschkowski, "Neutron scattering lengths," in *Neutron Data Booklet*, A.-J. Dianoux and G. Lander, Eds., OCP Science, 2003, pp. 1.1–1, 1.1–17 (cited on p. 27).

[69] R. Nathans and A. Paoletti, "Magnetic form factor of cobalt," *Phys. Rev. Lett.*, vol. 2, pp. 254–256, 1959 (cited on p. 28).

[70] M. Blume, "Orbital contribution to the magnetic form factor of Ni^{++}," *Phys. Rev.*, vol. 124, pp. 96–103, 1961 (cited on p. 28).

[71] M. Blume, A. J. Freeman, and R. E. Watson, "Neutron Magnetic Form Factors and X-Ray Atomic Scattering Factors for Rare-Earth Ions," *J. Chem. Phys.*, vol. 37, pp. 1245–1253, 1962 (cited on p. 28).

[72] P. J. Brown, "Magnetic form factors," in *Neutron Data Booklet*, A.-J. Dianoux and G. Lander, Eds., OCP Science, 2003, pp. 2.5–1, 2.5–12 (cited on p. 28).

[73] R. Caciuffo, T. Guidi, G. Amoretti, *et al.*, "Spin dynamics of heterometallic Cr_7M wheels (M = Mn, Zn, Ni) probed by inelastic neutron scattering," *Phys. Rev. B*, vol. 71, p. 174 407, 2005 (cited on p. 29).

[74] *IN5 Schematic*, `https://www.ill.eu/users/instruments/instruments-list/in5/description/instrument-layout`, Accessed Dec. 28th, 2023 (cited on p. 30).

[75] J. Ollivier and H. Mutka, "IN5 cold neutron time-of-flight spectrometer, prepared to tackle single crystal spectroscopy," *J. Phys. Soc. Jpn.*, vol. 80, no. Suppl.B, SB003, 2011. DOI: 10.1143/JPSJS.80SB.SB003 (cited on p. 30).

[76] R. Eccleston, "Time-of-flight inelastic scattering," in *Neutron and X-Ray Spectroscopy*, F. Hippert, E. Geissler, J. L. Hodeau, E. Lelièvre-Berna, and J.-R. Regnard, Eds. Springer, 2006, pp. 457–482 (cited on p. 30).

[77] O. Waldmann, G. Carver, C. Dobe, *et al.*, "Magnetic relaxation studies on a single-molecule magnet by time-resolved inelastic neutron scattering," *Appl. Phys. Lett.*, vol. 88, no. 4, p. 042 507, 2006. DOI: 10.1063/1.2164409 (cited on p. 31).

[78] A. Chiesa, T. Guidi, S. Carretta, *et al.*, "Magnetic exchange interactions in the molecular nanomagnet Mn_{12}," *Phys. Rev. Lett.*, vol. 119, p. 217 202, 21 2017. DOI: 10.1103/PhysRevLett.119.217202 (cited on pp. 31, 125).

[79] M. L. Baker, T. Guidi, S. Carretta, *et al.*, "Spin dynamics of molecular nanomagnets unravelled at atomic scale by four-dimensional inelastic neutron scattering," *Nat. Phys.*, vol. 8, pp. 906–911, 2012. DOI: 10.1038/nphys2431 (cited on pp. 31, 125).

[80] E. Garlatti, T. Guidi, S. Ansbro, *et al.*, "Portraying entanglement between molecular qubits with four-dimensional inelastic neutron scattering," *Nat. Commun.*, vol. 8, p. 14 543, 2017. DOI: 10.1038/ncomms14543 (cited on pp. 31, 125).

[81] S. Carretta, P. Santini, G. Amoretti, *et al.*, "Quantum oscillations of the total spin in a heterometallic antiferromagnetic ring: Evidence from neutron spectroscopy," *Phys. Rev. Lett.*, vol. 98, p. 167 401, 16 2007. DOI: 10.1103/PhysRevLett.98.167401 (cited on pp. 31, 125).

[82] M. Kofu, O. Yamamuro, T. Kajiwara, *et al.*, "Hyperfine structure of magnetic excitations in a Tb-based single-molecule magnet studied by high-resolution neutron spectroscopy," *Phys. Rev. B*, vol. 88, p. 064 405, 2013 (cited on p. 31).

[83] M. Kofu, T. Kajiwara, J. S. Gardner, *et al.*, "Magnetic relaxations in a Tb-based single molecule magnet studied by quasielastic neutron scattering," *Chem. Phys.*, vol. 427, pp. 147–152, 2013. DOI: https://doi.org/10.1016/j.chemphys.2013.10.004 (cited on pp. 31, 128).

[84] M. A. Dunstan, M. J. Giansiracusa, M. Vonci, *et al.*, "Direct observation of magnetoelastic coupling in a molecular spin qubit: New insights from crystal field neutron scattering data," *Chem. Sci.*, vol. 14, pp. 3990–4001, 15 2023. DOI: 10.1039/D2SC05797B (cited on pp. 31, 128).

[85] J. J. Borrás-Almenar, J. M. Clemente-Juan, E. Coronado, and B. S. Tsukerblat, "MAGPACK: A package to calculate the energy levels, bulk magnetic properties, and inelastic neutron scattering spectra of high nuclearity spin clusters," *J. Comput. Chem.*, vol. 22, no. 9, pp. 985–991, 2001. DOI: https://doi.org/10.1002/jcc.1059 (cited on p. 32).

[86] N. F. Chilton, R. P. Anderson, L. D. Turner, A. Soncini, and K. S. Murray, "PHI: A powerful new program for the analysis of anisotropic monomeric and exchange-coupled polynuclear d- and f-block complexes," *J. Comput. Chem.*, vol. 34, no. 13, pp. 1164–1175, 2013. DOI: https://doi.org/10.1002/jcc.23234 (cited on p. 32).

[87] R. D. Cannon and R. P. White, "Chemical and physical properties of triangular bridged metal complexes," *Prog. Inorg. Chem.*, vol. 36, no. 12, pp. 195–298, 1988 (cited on p. 79).

[88] R. White, J. Al-Basseet, R. Cannon, G. Kearley, and U. Jayasooriya, "Temperature dependent magnetic exchange interactions in a mixed-valence complex: A neutron scattering study," *Physica B: Condens. Matter*, vol. 156-157, pp. 367–369, 1989. DOI: https://doi.org/10.1016/0921-4526(89)90680-7 (cited on p. 79).

[89] U. A. Jayasooriya, R. D. Cannon, C. E. Anson, S. K. arapKoske, R. P. White, and G. J. Kearley, "Intermolecular magnetic interactions in a mixed-valence compound: Inelastic neutron scattering spectrum of $[Fe_2FeO(O_2CCD_3)_6(C_5D_5N)_3](C_5D_5N)$," *J. Chem. Soc., Chem. Commun.*, pp. 379–381, 4 1992. DOI: 10.1039/C39920000379 (cited on p. 79).

[90] R. P. White, J. A. Stride, S. K. Bollen, *et al.*, "Electronic interactions in mixed-valence and mixed-metal ion clusters: Inelastic neutron scattering spectra of the complexes $[Fe_2^{3+}M^{2+}O(OOCMe)6(py)3](py)$, where m = manganese, nickel," *JACS*, vol. 115, no. 17, pp. 7778–7782, 1993. DOI: 10.1021/ja00070a025 (cited on p. 79).

[91] R. D. Cannon, U. A. Jayasooriya, R. P. White, and S. K. ArapKoske, "New electronic transitions observed in the trinuclear iron(III,III,II) cluster, by inelastic neutron scattering," *Spectrochim Acta A Mol Spectrosc.*, vol. 49, no. 12, pp. 1787–1791, 1993. DOI: https://doi.org/10.1016/0584-8539(93)80247-8 (cited on p. 79).

[92] R. D. Cannon, U. A. Jayasooriya, R. Wu, *et al.*, "Spin frustration in high-spin triiron(III) complexes: An inelastic neutron scattering study," *JACS*, vol. 116, no. 26, pp. 11 869–11 874, 1994. DOI: 10.1021/ja00105a029 (cited on p. 79).

[93] M. Atzori and R. Sessoli, "The second quantum revolution: Role and challenges of molecular chemistry," *JACS*, vol. 141, no. 29, pp. 11 339–11 352, 2019. DOI: 10.1021/jacs.9b00984 (cited on p. 125).

[94] S. Carretta, D. Zueco, A. Chiesa, Á. Gómez-León, and F. Luis, "A perspective on scaling up quantum computation with molecular spins," *Appl. Phys. Lett.*, vol. 118, no. 24, p. 240 501, 2021. DOI: 10.1063/5.0053378 (cited on p. 125).

[95] I. H. Deutsch, "Harnessing the power of the second quantum revolution," *PRX Quantum*, vol. 1, p. 020 101, 2 2020. DOI: 10.1103/PRXQuantum.1.020101 (cited on p. 125).

[96] A. E. Thorarinsdottir, R. Bjornsson, and T. D. Harris, "Insensitivity of magnetic coupling to ligand substitution in a series of tetraoxolene radical-bridged Fe_2 complexes," *Inorg. Chem.*, vol. 59, no. 7, pp. 4634–4649, 2020. DOI: 10.1021/acs.inorgchem.9b03736 (cited on p. 126).